COO-3072-19

Princeton University
Elementary Particles Laboratory
Department of Physics

A MEASUREMENT OF THE ANGULAR DISTRIBUTION OF

$n + p \rightarrow d + \gamma$

AS A TEST OF TIME-REVERSAL INVARIANCE

PAUL EUGENE GOLDHAGEN

TECHNICAL REPORT NO. 6

February 1973

Contract AT(11-1)-3072

A MEASUREMENT OF THE ANGULAR DISTRIBUTION OF

$n + p \rightarrow d + \gamma$

AS A TEST OF TIME-REVERSAL INVARIANCE

Paul Eugene Goldhagen

A DISSERTATION

PRESENTED TO THE

FACULTY OF PRINCETON UNIVERSITY

IN CANDIDACY FOR THE DEGREE

OF DOCTOR OF PHILOSOPHY

RECOMMENDED FOR ACCEPTANCE BY THE

DEPARTMENT OF

PHYSICS

February, 1973

ACKNOWLEDGEMENTS

A modern experiment in high energy physics, even a fairly modest one, requires dozens of man-years of labor. I would here like to express my appreciation to the people who helped make possible the experiment described in this work.

My colleagues Dr. David Bartlett, Dr. Konstantin Goulianos, and Dr. Carl Friedberg had to work very hard to enable our relatively small research group to complete the experiment. David acted as my academic advisor until his move to the University of Colorado, whereupon Dino took over that task, including the supervision of this thesis. Throughout the experiment David's reasoned approach and Dino's energy and inventiveness produced effective experimental physics. Carl almost single-handedly created the data-reduction computer programs and organized the slow electronic logic. From design through publication they all remained sympathetic to my needs and each other's. It was truly a pleasure to work with them.

Dr. David Hutchinson provided helpful advice on small Čerenkov counters. Four graduate students, Jacob Bekenstein, James Fines, Sidney Nagel, and Bennie Ward, helped at various times during setup and running.

I would like to thank the entire PPA staff under the guidance of Professor M. White for supporting every aspect of this experiment, even though they faced the imminent closing of the PPA. The perseverance of Halsey Allen, Marius Isala, and the rest of the synchrotron crew during the initial acceleration of the special deuteron beam we required deserves particular mention. Direct help during construction and emergencies was given by F. Homan's target group, R. Jankowicz's liquid

hydrogen target group, the floor crew, the watch crew, the electronics shop, and the health physics group.

Howard Edwards and his staff helped design the spark chambers and most of the mechanical supports of the apparatus. Fred Schwartz and his staff built the counters and helped us with all mechanical problems. Ed Card built most of our home-designed electronic circuits. John Gomany and his drafting shop staff transformed my sketches into drawings, which Bob Mathews and J. S. Lechner photographed to produce the figures of this work.

"They also serve who only stand and wait," so thanks go to the other experimenters on the PPA floor who waited for six weeks while we used the PPA exclusively.

This thesis was typed by Pearl Goldhagen, my mother, whose experience in preparing manuscripts, cooperativeness, patience, and free services are greatly appreciated.

Finally, I would like to thank the Atomic Energy Commission and the taxpayers of the United States for the funds (AEC contract AT(11-1)-3072, formerly AT(30-1)-4159) which made this experiment possible.

TABLE OF CONTENTS

LIST OF TABLES

LIST OF FIGURES

ABSTRACT

The angular distribution of $n + p \rightarrow d + \gamma$ has been measured at neutron kinetic energies of 475, 560, 625, and 750 MeV. An intense neutron beam was prepared by allowing deuterons accelerated in the Princeton-Pennsylvania Accelerator to strip in an internal Beryllium target. Velocities and angles of the particles were determined using accurate time-of-flight techniques and magnetostrictive read-out wire spark chambers. Results based on 31000 events at nine scattering angles are reported and compared with existing data for the inverse reaction $\gamma + d \rightarrow n + p$. The angular distributions are found to agree, as predicted by time-reversal invariance.

CHAPTER I

HISTORICAL AND THEORETICAL BACKGROUND

SECTION A INTRODUCTION

This work describes a measurement of the angular distribution (arbitrarily normalized differential cross section) of the reaction

$$n + p \rightarrow d + \gamma \quad , \tag{1.1}$$

performed as a test of time-reversal invariance (TRI). The test consists of comparison of the angular distribution of reaction (1.1) in the center-of-mass reference frame with the c.m. angular distribution of the reaction

$$\gamma + d \rightarrow n + p \quad . \tag{1.2}$$

One of the consequences of TRI is that these two distributions should be the same at the same c.m. energy, or, to the approximation that $m_p = m_n = \frac{1}{2}m_d$, when

$$T_n \cong 2\ E_\gamma \quad , \tag{1.3}$$

where T_n is the laboratory kinetic energy of the incident neutron in (1.1) and E_γ is the laboratory energy of the incident gamma ray in (1.2). This experiment was performed at the Princeton-Pennsylvania Accelerator (PPA) in 1970 with David F. Bartlett, Carl Friedberg, and Konstantin Goulianos. A short report of it has appeared in Physical Review Letters.[1]

The interactions of elementary particles were originally presumed to be symmetric under each of the discrete transformations of parity (P), charge conjugation (C), and time reversal (T). These symmetries first came under close scrutiny in 1956 when the weak interactions were discovered to violate invariance under P and under C.[2-4] The current interest in tests of TRI was stimulated by the discovery in 1964 of the decay $K_L^\circ \rightarrow \pi^+ + \pi^-$,[5] the existence of which violates invariance under the combined transformation CP. According to the CPT theorem, which

states that any "reasonable" quantum field theory is invariant under the combined transformation CPT,[6] the existence of this decay also violates TRI. Further results on the neutral kaon system indicate that TRI is violated there regardless of the validity of CPT invariance.[7] Although CP and T noninvariance are extremely well established in the neutral kaon system, no experiment has yet conclusively demonstrated the existence of either elsewhere.

Reaction (1.2), photodisintegration of the deuteron, has been of continuing interest since the early 1950's. Its angular distribution and total cross section at high energies have been measured many times.[8-25]

The experiment described in this work is the third measurement of the angular distribution of $n + p \rightarrow d + \gamma$ at laboratory neutron kinetic energies in the vicinity of $T_n = 600$ MeV where production of the $\Delta(1236)$ might allow a violation of TRI to be seen (see section I.D). The two earlier measurements were begun in 1966 by a Princeton group: D. Bartlett, C. Friedberg, K. Goulianos, I. Hammerman, and D. Hutchinson and by a UCLA-Michigan-LRL collaboration: B. Schrock, J. Detoeuf, R. Haddock, J. Helland, M. Longo, K. Young, S. Wilson, D. Cheng, J. Sperinde, and V. Perez-Mendez. The angular distribution of $n + p \rightarrow d + \gamma$ at $T_n \cong 580$ MeV reported by Bartlett *et al.* in 1969[26,27] had only about a 12% chance of agreeing with well established data[10,12,18,21] for $\gamma + d \rightarrow n + p$. A similar inconclusive disagreement was reported by Schrock *et al.* in 1970[28] based on 15% of their data. Upon completion of the analysis of all their data, they reported in 1971 good agreement with the inverse reaction.[29]

The present experiment differs from the first two in a number of important ways. Data was taken at $T_n \cong 475$, 560, 625, and 750 MeV, for the first time reaching energies well above that of the $\Delta(1236)$

resonance peak. This was made possible by the first use in a high energy experiment of a neutron beam produced by stripping accelerated deuterons. For each energy, data was taken over a wider angular range than in the earlier experiments, in nine bins instead of seven or five. The momenta of the neutron and deuteron, used to separate reaction (1.1) from background, were measured to an accuracy of about ± 1% using only the time of flight of the particles; there were no analyzing magnets in the experiment. The positions of electron showers near the conversion points of the gamma rays were measured using magnetostrictive read-out wire spark chambers. Apparatus inefficiencies were measured, and errors in these measurements were included in the errors in the angular distribution. The separation of $n + p \rightarrow d + \gamma$ events from background was performed in two independent ways, neither of which relied on Monte Carlo programs. About 31000 events from $n + p \rightarrow d + \gamma$ were collected, roughly the same number collected by Schrock *et al.* and about 10 times the number collected during the first experiment by Bartlett *et al.*

The remainder of this chapter is devoted to discussions of time reversal in general, TRI in the electromagnetic interactions of strongly interacting particles (hadrons), and theoretical aspects of time-reversal noninvariance in $n + p \rightleftarrows d + \gamma$.

SECTION B TIME REVERSAL

The time-reversal transformation of a physical system, like the parity transformation, is an improper Lorentz transformation. It is the inversion (reflection) of the time coordinate:

$$t' = T(t) = -t \quad .$$

The physical laws governing a system are said to be time-reversal invariant if they do not change form under T. An equivalent definition is that a system obeys TRI if it can develop backward in time in the same way that it normally does forward in time.

The laws of classical mechanics and electromagnetism are time--reversal invariant, as illustrated by the following example. Consider the motion of a particle of mass m in a conservative force field $\vec{F}(\vec{x})$ as described by Newton's second law:

$$\frac{d\vec{p}}{dt} = \vec{F}(\vec{x}) \quad , \quad \vec{p} = m\frac{d\vec{x}}{dt} \quad ,$$

and let $\vec{x}(t)$ be a solution. Applying T, the time-reversed system is described by

$$\frac{d\vec{p}'}{dt'} = \vec{F}(\vec{x}) \quad , \quad \vec{p}' = m\frac{d\vec{x}}{dt'}$$

with $\vec{x}(t') = \vec{x}(-t)$ as a solution. The equations describing this system are thus time-reversal invariant. Suppose the initial conditions were such that the system evolved forward from a state $\vec{x}_i$, $\vec{p}_i$ at $t = t_i < 0$ along the trajectory $\vec{x}(t)$ to a state $\vec{x}_f$, $\vec{p}_f$ at $t = 0$. The time--reversed system would then evolve backward along the same trajectory from its initial state $\vec{x}_i' = \vec{x}_f$, $\vec{p}_i' = -\vec{p}_f$ at $t' = t = 0$ to its final state $\vec{x}_f' = \vec{x}_i$, $\vec{p}_f' = -\vec{p}_i$ at $t' = -t_i$. This example illustrates the rule that for a system obeying TRI, time-reversed

states are prepared by interchanging the initial and final forward states and reversing the signs of time and momentum. Since position is unaffected by T, the sign of angular momentum, $\vec{x} \times \vec{p}$, is also reversed.

In quantum mechanics, a transformation which changes a state Ψ of a system into another state Ψ' of the same system is an operator. Thus, if a system obeys TRI, T is an operator, and its explicit form can be sought. This was first done in 1932 by E. Wigner.[30] Results stated in this section concerning the form of the T operator are due to Wigner.

If a system obeys the Schrödinger equation,

$$i\hbar \, \partial\Psi/\partial t = H\Psi \quad ,$$

then the time reversed equation is

$$i\hbar \, \partial\Psi'/\partial t' = H'\Psi' \quad ,$$

where $t' = -t$, $\Psi' = T\Psi$, and $H' = THT^{-1}$. Note that Schrödinger's equation is invariant under T if and only if $H' = H$. In addition, if the system obeys TRI, T must preserve the transition probability:

$$|\langle T\Psi_1 | T\Psi_2 \rangle| = |\langle \Psi_1 | \Psi_2 \rangle| \quad .$$

The most general operator satisfying these conditions can be written in the form $T = UK$, where U is a unitary operator and K denotes complex conjugation of the quantity following it. The form of U depends on the particular representation used. T commutes with observables which are either time-independent or which depend on even powers of the time variable, such as position coordinates or total energy. T anticommutes with observables which depend on odd powers of t, such as linear and angular momenta. For the Schrödinger theory without spin, in the position coordinate representation, the commutation relations imply that U is of modulus one. Since the phase is arbitrary, U may be taken

to be the identity operator, so that T = K. For the case of n spin ½ particles, the commutation relations imply that

$$U = \sigma_y(1)\,\sigma_y(2)\cdots\sigma_y(n) \quad ,$$

where $\sigma_y(j)$ is the imaginary spin operator of the jth particle and the spin operators are the Pauli matrices:

$$\sigma_x = \begin{bmatrix} 0 & 1 \\ 1 & 0 \end{bmatrix} \quad , \quad \sigma_y = \begin{bmatrix} 0 & -i \\ i & 0 \end{bmatrix} \quad , \quad \sigma_z = \begin{bmatrix} 1 & 0 \\ 0 & -1 \end{bmatrix} \quad .$$

If a state is specified by eigenvalues, m, of σ_z , then

$$T\,|\,m_1\,,\cdots m_n\,\rangle = (i)^{2(m_1+\cdots m_n)}\;|\,-m_1\,,\cdots -m_n\,\rangle \quad . \qquad (1.4)$$

Similar relations hold for eigenstates of orbital and total angular momentum.

There are two general predictions of TRI which make experimental tests possible. These will be discussed in terms of the scattering matrix, which is a function of the hamiltonian, S = S(H). It has already been remarked that TRI implies $THT^{-1} = H$. This means that any operator which is part of a time-reversal invariant hamiltonian must commute with T. Operators which anticommute with T, such as transverse polarization, $\vec{\sigma} \cdot (\vec{p}_1 \times \vec{p}_2)$, are forbidden to appear in the hamiltonian. The appearance of such a term in an experimental process implies a violation of TRI if and only if the S-matrix is proportional to the hamiltonian. That is, such a test is valid to the extent that there are no final-state interactions, so that first order perturbation theory (the Born approximation) is valid.

The second testable prediction of TRI, the one used in this experiment, is the reciprocity theorem. This theorem states that for a system which obeys TRI the S-matrix element for the time-reversed process ("inverse") is the same as for the forward process:

$$\langle T\Psi_i \mid S \mid T\Psi_f \rangle = \langle \Psi_f \mid S \mid \Psi_i \rangle \quad . \tag{1.5}$$

This implies that the reaction rates, and therefore the differential and total cross sections, of the direct and inverse reactions will be kinematically related.

Consider the case of two-body scattering in the center of mass: $a + b \rightarrow c + d$, $\vec{p}_b = -\vec{p}_a$, $\vec{p}_c = -\vec{p}_d$. It is experimentally convenient not to have to detect spins. Summing over final spin states and averaging initial polarizations, the reciprocity theorem leads to

$$\frac{d\sigma}{d\Omega}(\leftarrow) = \frac{(2s_a + 1)(2s_b + 1)}{(2s_c + 1)(2s_d + 1)} \frac{p_a^2}{p_d^2} \frac{d\sigma}{d\Omega}(\rightarrow) \quad .$$

Since the ratio of direct and inverse differential cross sections is independent of angle, it follows that the total cross sections have this same ratio and that the angular distributions are identical. If the angular distributions of $a + b \rightarrow c + d$ and $d + c \rightarrow b + a$ at the same c.m. energy are observed to be different, then TRI is violated in the reaction. The converse may not be true, however. Even if the angular distributions are the same after summing over and averaging spin states, TRI violating effects may be present in different spin channels.

Care must be exercised in searching for violations of either type of prediction of TRI because the effect being sought may be forbidden or reduced by other symmetry principles. For example, the static electric dipole moment of a particle with spin is required to be zero both by TRI and by parity conservation (see section I.C). Other important examples of principles forbidding the observation of violation of TRI under certain circumstances are "detailed balance" and current conservation.

Consider the reciprocity theorem (1.5) and schematically represent the initial and final wave functions as

$$|\Psi_i\rangle = |\alpha , \vec{p}_i , m_i\rangle \quad , \quad |\Psi_f\rangle = |\beta , \vec{p}_f , m_f\rangle \quad , \text{ where,}$$

for initial and final states, respectively, p_i, p_f represent all momenta, m_i, m_f represent the orientation of all spins, and α,β represent all other (even under T) characteristics such as particle identities. Then, using equation (1.4) and conservation of statistics,

$$\langle \beta , \vec{p}_f , m_f | S | \alpha , \vec{p}_i , m_i\rangle = \pm 1\langle \alpha , -\vec{p}_i , -m_i | S | \beta , -\vec{p}_f, -m_f\rangle \ . \quad (1.6)$$

Now suppose that the S-matrix is proportional to the hamiltonian (no final state interactions); then the hermiticity of the hamiltonian alone leads to

$$\langle \beta, \vec{p}_f, m_f | H | \alpha, \vec{p}_i, m_i\rangle = \langle \alpha, \vec{p}_i, m_i | H | \beta, \vec{p}_f, m_f\rangle \ .$$

As in (1.6), predicted by TRI, this is a relation between incoming and outgoing states, but momenta and spins are not reversed. If parity is conserved or, in the case of two-body scattering if there is merely rotational invariance, then the signs of the momenta can be changed to obtain the same result predicted by TRI except for spin. This result is called detailed balance and is the reason it was first thought that reciprocity tests of TRI would have to measure spin.[31] The way around this difficulty is to use a process which has final-state interactions so that detailed balance does not apply. A failure of TRI can then be observed by interference.

A discussion of the effects of current conservation on reciprocity tests is presented in the next section.

For proofs and further details concerning the time-reversal operator, the interested reader is referred to the work of Wigner,[30]

and to Bohr and Mottelson.[32] Derivations of the reciprocity theorem can be found in the latter and Blatt and Weisskopf,[33] Williams,[34] and Sakurai.[35] An extensive discussion of invariance principles can be found in the review article by Wick.[36]

SECTION C TIME REVERSAL INVARIANCE IN THE ELECTROMAGNETIC INTERACTIONS OF HADRONS

Following the discovery of CP noninvariance by Christensen et al.,[5] Bernstein, Feinberg, and Lee (BFL) examined the experimental evidence for the discrete symmetry properties of the strong and electromagnetic interactions.[31] Using the K_1°-K_2° mass difference, $|\Delta m/m_K| \cong 10^{-14}$, they concluded that the strong and electromagnetic interactions are invariant under CPT to accuracies of $\sim 10^{-14}$ and $\sim 10^{-12}$, respectively. Using the ratio of P-noninvariant to P-invariant amplitudes in nuclear reactions they concluded that the two interactions are invariant under P to accuracies of $\sim 10^{-5}$ and $\sim 10^{-3}$, respectively. Any violation of TRI in these interactions will thus be accompanied by a violation of C invariance and vice versa. The strong interaction was found to obey TRI to an accuracy of $\sim 2\%$. (This limit has since been reduced to $\sim 0.1\%$.[34]) The electromagnetic interactions of leptons are known to be invariant under C, P, and T separately from the very accurate experiments on (g-2) and the Lamb shift. At the time of BFL's investigation there was, however, no evidence for invariance under C or T of the electromagnetic interactions of hadrons (EMIH). BFL went on to point out that the CP noninvariance observed in the K° system might be due to a failure of C and T invariance in EMIH.

One reason that no experimental information on TRI in EMIH existed in 1965 is that observation of T noninvariance is often forbidden by conservation of current. Invariance under continuous Lorentz transformations and P implies that the matrix element characterizing the electromagnetic interaction of a single physical nucleon obeys the following relation:[31]

$$\langle N' \mid J_\mu(x) \mid N \rangle \propto \gamma_\mu F_1 + i(N_\mu' + N_\mu)F_2 + (N_\mu' - N_\mu)F_3 \quad ,$$

where N_μ, N_μ' are the initial and final nucleon 4-momenta, and F_1, F_2, F_3 are functions of the square of the 4-momentum transfer, $q^2 \equiv (N_\mu' - N_\mu)^2$, only. Hermiticity requires that all the F's be real, while TRI requires that F_3 be imaginary, so $F_3 \neq 0$ implies T noninvariance. However, conservation of the electromagnetic current requires $F_3 = 0$, so that no TRI violating effects can be observed when the nucleons are on the mass shell.

Subsequent to the suggestions of BFL, a number of experimental tests of T and C invariance in EMIH have been performed. Six of these tests which have achieved accuracies which might have enabled them to see expected effects due to maximal violations are very briefly discussed below. None of the tests has shown a significant violation, but calculations of expected effects due to possible violations are so model-dependent that it is difficult to generalize and conclude that T noninvariance could not show up elsewhere. Since it is a distinguishing feature of EMIH that isotopic spin can change by an integer ($|\Delta I| = 0,1$) in the first order interaction, the possible values of $|\Delta I|$ in each test are noted. TRI in the present experiment is discussed in section I.D.

(1) Electric dipole moment of the neutron ($|\Delta I| = 0,1$)

For a particle with spin, a static electric dipole moment, $\vec{D}$, must have a fixed orientation with respect to the spin, $\vec{D} = k\vec{\sigma}$. Under T, $\vec{D}$ is even and $\vec{\sigma}$ is odd, so TRI implies $|\vec{D}| = 0$. Under P, $\vec{D}$ is odd and $\vec{\sigma}$ is even, so P invariance also requires $|\vec{D}| = 0$. In 1965 Feinberg[37] estimated that if TRI were maximally violated in EMIH and if P invariance were maximally violated in a first order weak, $\Delta S = 0$, 4-baryon

interaction, then the static electric dipole moment of the neutron might be of order $|D| \sim e\,(G_F/m_p^2)m_p \sim 10^{-19}$ e−cm, which was then the experimental limit. The current experimental limit is $|\vec{D}| = 1.8 \pm 1.1 \times 10^{-23}$ e−cm.[38] This limit is still not considered conclusive evidence for TRI in EMIH since other estimates of the effect of a violation have been made which are this small.

(2) $\pi^- + p \rightleftarrows n + \gamma$ ($|\Delta I| = 0,1,2?$)

A test of reciprocity can be made by comparing the differential cross section of $\pi^- + p \rightarrow n + \gamma$ with that of $\gamma + n \rightarrow \pi^- + p$ deduced from $\gamma + d$ experiments. The former reaction has recently been studied and the comparison made by Berardo *et al.*[39] at center-of-mass energies of 1245, 1337, and 1363 MeV. They report no significant violation of reciprocity except at 1245 MeV where the absolute differential cross section disagrees with that predicted by reciprocity by about 30% (2σ) for $\theta_{\gamma\pi} > 90°$. Using a model by Christ and Lee[40] in which a phase, φ, which violates TRI is added to the T-invariant phases of the conventional multipoles, they interpret their results as $|\varphi_{M1^+}^{3/2}| = 10° \pm 5°$.

(3) Inelastic electron scattering from polarized protons ($|\Delta I| = 0,1$)

If all inelastic final states of e + p (polarized) → e + (anything) are included, then a correlation of the normal to the electron scattering plane with the target polarization, $\hat{\sigma}_p \cdot (\hat{p}_e \times \hat{p}_e')$, is odd under T. If N^+ is the number of events with a positive correlation, N^- the number with negative correlation, and P the average magnitude of the target polarization, then $A \equiv (N^+ - N^-)/P(N^+ + N^-)$ is required to be zero by TRI, if the scattering proceeds by one-photon exchange. A non-zero

value of A would be due to interference of the transverse and scaler part of the virtual photon. Chen et al.[41] find no significant deviation from A = 0 in any kinematic region and A = .038 ± .043 at the Δ(1236), where $|\Delta I| = 1$. Rock et al.[42] find similar results except at a missing mass of 1200 ± 50 MeV where A = (4.5 ± 1.4) %.

(4) $\eta^\circ \to \pi^\circ + e^+ + e^-$ $(|\Delta I| = 1)$

The quantum numbers of the eta meson are $I^G (J^P)\ C = 0^+ (0^-) +$. If this decay proceeds by one photon exchange, $\eta^\circ \to \pi^\circ + (\gamma \to) e^+ + e^-$, then it is forbidden by C invariance, although the process $\eta^\circ \to \pi^\circ + (\gamma + \gamma \to) e^+ + e^-$ is allowed. Calculations show that the branching ratio of the two-photon process to all eta decays should be $\sim 10^{-4}$ to 10^{-5}. If C invariance is maximally violated, the expected branching ratio of the one-photon to all eta decays is ~ 0.5. Bazin et al.[43] report a world average of the branching ratio limit of

$$\frac{R\ (\eta^\circ \to \pi^\circ + e^+ + e^-)}{R\ (\eta^\circ \to \text{all})} < 2 \times 10^{-4} \quad .$$

This limit is an indication that a large violation of C (and T) invariance in the isovector ($|\Delta I| = 1$) current of EMIH is unlikely.

(5) $\eta^\circ \to \pi^+ + \pi^- + \pi^\circ$ $(|\Delta I| = 0,1,2)$

Since the G-parity of the η° is + and of 3π is -, this decay is electromagnetic. C invariance requires the energy distributions of the π^+ and π^- mesons to be identical, since C interchanges π^+ and π^- without affecting their momenta. If $N^+(N^-)$ is defined as the number of decays where the energy of the $\pi^+(\pi^-)$ is greater than the energy of the $\pi^-(\pi^+)$, then an asymmetry can be defined by $A = (N^+ - N^-)/(N^+ + N^-)$. In the absence of final-state interactions, hermiticity and CPT

invariance require A = 0. Final-state π-π interactions lead to the expectation that if C is maximally violated, A could have a value of a few percent. The most recent published experiment, performed by a Columbia group, found A = (1.5 ± 0.5) %.[44] The experiment has been repeated by Columbia, and the new result is A = (0.03 ± 0.22) %.[45]

(6) $\underline{\eta^\circ \to \pi^+ + \pi^- + \gamma}$ ($|\Delta I| = 0,1,2$)

The discussion concerning $\eta^\circ \to \pi^+ + \pi^- + \pi^\circ$ is applicable to this decay, and the Columbia group has also measured it twice. The latest published result is A = (2.4 ± 1.4) %.[46] The new result is A = (0.5 ± 0.6) %.[47]

SECTION D THEORETICAL ASPECTS OF TIME-REVERSAL NONINVARIANCE IN $n + p \rightleftarrows d + \gamma$

In 1965, D. F. Bartlett and K. Goulianos noticed some features of the reactions $n + p \rightleftarrows d + \gamma$ ($\rightarrow$ (1.1), $\leftarrow$ (1.2)) which make them appropriate for a reciprocity test of TRI in EMIH. Reaction (1.2) had been measured reasonably well, and it is experimentally possible to reverse it and measure reaction (1.1). The total cross section of (1.2) has a large bump at $E\gamma \cong 290$ MeV which is due to the production of the $\Delta(1236)$ $J = I = 3/2$ nucleon isobar in an intermediate state. A nucleon is thus excited off the mass shell and there are final-state interactions so that current conservation and detailed balance do not preclude the observation of a violation of TRI. In addition to the resonance, background amplitudes are also present, so a possible violation of TRI could be observed by interference.

The interest of Bartlett and Goulianos in reactions (1.1) and (1.2) led to their communicating with S. Barshay, who was independently studying reciprocity relations. Barshay then proposed a specific model for possible violation of TRI in $n + p \rightleftarrows d + \gamma$.[48] Barshay's model makes three important predictions. First, the effects of TRI violation should be observable only near the resonance peak. Second, the difference between the center-of-mass angular distributions of reactions (1.1) and (1.2) should be proportional to the second order Legendre polynomial (symmetric about 90°) and may be as large as 40% if TRI is maximally violated. Third, there should be no violation in the ratio of total cross sections predicted by TRI.

In the interest of completeness and to motivate the derivation of equation (1.11), which provides a parameterization of possible TRI

violation, a more detailed description of Barshay's model should be given. Such a description has, however, already been given by C. Friedberg.[49] To avoid plagiarism or clumsy paraphrasing, part of his discussion is quoted below:

> Barshay assumes that time reversal failure may be evidenced at the vertex $\gamma + N \rightleftarrows N^*$, where N^* denotes the 3/2,3/2 isobar $\Delta(1236)$. This vertex certainly contributes to the well known bump in the photodissociation total cross sections, and is off the mass shell as required by BFL. If the failure of T is manifested by the appearance of a non-zero phase at the γNN^* vertex, then a large reciprocity failure might occur, if the 'bad' amplitude interfered with a suitable background amplitude. This situation is represented schematically in Figure I.1, where (a) is the resonant amplitude in Barshay's model and (b) is a typical background graph.
>
> Barshay derives the following expression for the matrix element for $\gamma + d \rightarrow n + p$:

$$M = \frac{e^{i\Delta}}{|\vec{k}| + m - m^* + i\gamma/2} M_1 \left[3\hat{p}\cdot\hat{t}\ \hat{p}\cdot\hat{k} \times \hat{\epsilon} - \hat{t}\cdot\hat{k} \times \hat{\epsilon}\right] \chi_2\, \sigma^2\, \chi_1$$

$$+ a_o\ \hat{t}\cdot\vec{k} \times \hat{\epsilon}\ \chi_2^T\, \sigma^2\, \chi_1 + i b_o\ \hat{t}\cdot\hat{\epsilon}\ \chi_2^T\, \vec{\sigma}\cdot\vec{p}\, \sigma^2\, \chi_1 \qquad (1.7)$$

> where Δ is the T-violating phase, k is the CMS photon momentum, m the nucleon mass, m^* the isobar mass, $\gamma^* \approx 120$ MeV the isobar width, $\hat{p}$ the nucleon momentum, $\hat{t}$ the deuteron spin pseudo-vector, $\hat{\epsilon}$ the photon spin vector, and χ_i the nucleon spinors (χ_i^T are the transposed spinors). M_1 includes the remainder of the resonant $M(1) \rightarrow {}^1D_2$ amplitude, and includes an integral over the internal deuteron momentum which Barshay treats as an adjustable parameter to produce a 27 μb contribution to the total cross section (of 75 μb) at the resonance peak. Likewise, a_o and b_o, which represent two background amplitudes, have been chosen to give 3μb to $M(1) \rightarrow {}^1S_0$ and 45 μb to $E(1) \rightarrow {}^3P_0$ transitions, respectively. Although Barshay makes no attempt to derive the matrix elements for the background amplitudes, he does show that they are of a

reasonable size by calculating a mass μ:

$$\mu = \left\{ \frac{a}{\sqrt{8\pi}} \frac{e}{\sqrt{4\pi}} \left[\frac{m^2}{m_d \, |\vec{k}| \, E^2} \right]^{\frac{1}{2}} \frac{1}{a_o \text{ or } b_o} \right\}^{\frac{1}{2}} \approx m_\pi \quad ,$$

where a is the deuteron two-nucleon coupling constant $a^2/4\pi \approx .5$, and E is the C.M. energy of the nucleon.

For each of the three terms in M, the right-hand spinor factors project out the $^1D_2$ magnetic dipole, the $^1S_0$ magnetic dipole, and the $^3P_0$ electric dipole, respectively. Except for the $e^{i\Delta}$ term, M is time reversal invariant. Therefore the reversed matrix element will differ only by the phase factor $e^{-i\Delta}$. At the resonance peak (or slightly higher), the <u>real</u> part of the resonance energy denominator vanishes (first term in eqn. (1.7)--M_1 is real), so that the phase of the first term would become relatively real if $\Delta \approx \pi/2$, and could then interfere with the real $^1S_0$ magnetic dipole amplitude. This is the crux of Barshay's model. He finds the following expressions for the cross sections in μb (with the statistical and phase space factors moved around):

$$\frac{6\,|\vec{k}|}{p} \frac{d\sigma}{d\Omega} = 1.66[8.66+3\sin^2\theta \pm .94\cos(\delta_r+\Delta)(3\sin^2\theta-2)] \qquad (1.8)$$

for reaction (1.2) and

$$\frac{4p}{|\vec{k}|} \frac{d\sigma}{d\Omega} = 1.66[8.66+3\sin^2\theta \pm .94\cos(\delta_r-\Delta)(3\sin^2\theta-2)] \qquad (1.9)$$

for reaction (1.1). The $\pm$ indicates a phase uncertainty--the model cannot predict (for instance) whether the 90° point for reaction (1.2) would be above or below the 90° point for reaction (1.1). In order to account for non-zero internal deuteron momenta, Barshay takes the phase of the resonant denominator so that $|\tan\delta_r| = 3$. He then defines the asymmetry A as the difference of eqns. (1.8) and (1.9) divided by their sum. He finds that if $|\Delta| = \pi/4$, then for $\theta_n = 0$ or π, $|A| = 15\%$, and for $\theta_n = \pi/2$, $|A| = 5\%$. Since the term multiplying $\cos(\delta_r \pm \Delta)$ is proportional to a second order Legendre polynomial, integration of (1.8) and (1.9) will give identical results. Thus in this model, the total cross sections

obey reciprocity.

Equations (1.8) and (1.9) can be rewritten in the form

$$d\sigma/d\Omega \propto 1 + A_2 P_2(\cos\theta) \quad , \tag{1.10}$$

where $P_2(\cos\theta) = \frac{1}{2}(3\cos^2\theta - 1)$ is the second Legendre polynomial and contains all the dependence on θ, and

$$-A_2 = [1 \pm .94 \cos(\delta_r \pm \Delta)]/5.33 \quad ,$$

where the plus sign in front of Δ is for reaction (1.2) and the minus sign is for (1.1). The expression for A_2 in both reactions can be solved for Δ to obtain

$$\sin\Delta = 3\,[A_2(\gamma d \rightarrow np) - A_2(np \rightarrow d\gamma)] \quad . \tag{1.11}$$

Barshay's model ignores the sizable forward-backward asymmetry in the measured angular distributions of photodisintegration, which would add a term $A_1P_1(\cos\theta)$ to (1.10) where $A_1 \sim A_2$.

The above considerations led to the first two measurements of reaction (1.1).[26-29] The present experiment was inspired by the inconclusive results on the angular distribution near T_n = 580 MeV reported by Bartlett et al. in 1969[26,27] and Schrock et al. in 1970.[28] Neither experiment showed any evidence of violation of TRI in the total cross sections. Figure I.2 is a reproduction of a figure in C. Friedberg's thesis[50] which shows the measured total cross section of (1.1) as a function of energy and the cross section inferred from (1.2) by reciprocity. The resonance peak and nonresonant background are clearly visible. The measured and inferred cross sections agree to within $\sim$ 10%, where the accuracy of the comparison is limited by errors in the normalization of both reactions.

CHAPTER II

EXPERIMENTAL APPARATUS

SECTION A INTRODUCTION

The main consideration in designing the apparatus for this experiment was extraction of the desired signal,

$$n + p \rightarrow d + \gamma \quad , \tag{1.1}$$

from the kinematically similar background reaction,

$$n + p \rightarrow d + \pi^\circ \ (\rightarrow 2\gamma) \quad , \tag{2.1}$$

which has a cross section about 70 times greater than that of the signal. Without this background, the angular distribution for the $d\gamma$ reaction could be determined by measuring only the neutron and deuteron vector momenta with sufficient accuracy to bin the data. With the $d\pi^\circ$ background, it becomes important to accurately measure as many of the kinematic variables as possible in order to extract the signal. The energy of the photon was the only such variable not measured because it cannot practically be measured with an accuracy near enough to the accuracy of the other variables ($\sim \pm$ 1%) to add useful information.

The neutron beam for this experiment was provided by the Princeton--Pennsylvania Accelerator (PPA) at the end of 1970. With some extra equipment and a good deal of effort on the part of the crew, the PPA, nominally a proton synchrotron, was able to accelerate deuterons to kinetic energies up to and beyond 1500 MeV as we required. The deuterons were stripped in an internal beryllium target to produce a neutron beam which was filtered free of gamma rays, swept of charged particles, and collimated before passing through a liquid hydrogen target 230 feet from the internal target. The high intensity of the beam striking the hydrogen target, roughly 5×10^6 neutrons per second, allowed the use of an apparatus of low angular acceptance but capable of achieving the desired high resolving power.

A plan view diagram of the apparatus near the hydrogen target and farther downstream is shown in Figure II.1 and photographs of it in Figures II.2 and II.3. The velocity, hence the momentum, of a neutron which caused an event was measured by recording its time of flight (TOF) from the internal target to the thin counter, N, which detected the deuteron emerging from the hydrogen target. The start signal for the TOF measurement was provided by the rf accelerating voltage of the PPA (RF). The deuteron was also detected by one of two pairs of large counters, D1 through D4, and its velocity was obtained by measuring its TOF from the N counter to these D counters. This is a unique aspect of this experiment, as all other measurements of $n + p \rightarrow d + \gamma$ have used magnet spectrometers to measure the deuteron's momentum.[26-29] The direction of the deuteron was measured using six magnetostrictive read-out wire spark chambers. The error in this measurement was decreased by the use of three helium bags to reduce multiple scattering of the deuteron in air. The photon was converted in one of two $\frac{1}{4}$-inch ($\cong$ 1 radiation length) thick sheets of lead. In front of each converter an anti-counter, GA, rejected charged particles. Behind the converters there were two more wire spark chambers, and behind the chambers there were two pairs of "gamma" counters, G1 through G4, which detected electrons. The neutron beam was monitored primarily by the proton monitor telescope, which consisted of the counters N, PM1, and PM2, and selected by time of flight recoil protons at 30° in the laboratory. Additional monitoring was provided by the NM telescope, which consisted of an anti-counter, a $\frac{3}{4}$-inch thick polyethylene cube, and two small counters. The NM telescope was located in the beam 60 feet downstream of the hydrogen target. There was also a beam spill intensity monitor, not shown in the diagram, which was a Čerenkov counter near the

internal target with its output averaged over 2 μsec. It was used in correcting for rate dependent effects.

Data were taken in nine separate bins of the center-of-mass deuteron angle, θ_d^* (= 180° - θ_γ^*), approximately 15° wide, spaced approximately every 20° in the center of mass system for each of four separate energy runs with mean laboratory kinetic energies, T_n, of 475, 560, 625, and 750 MeV. The apparatus was designed to subtend approximately the same solid angle in the center of mass sytem for each angular bin. This was accomplished by mounting the gamma assembly on a cart connected by an 8-foot radius arm to a pivot 4 feet downstream of the hydrogen target so that it was constrained to move along a locus which approximated the $n + p \rightarrow d + \gamma$ kinematic ellipse for T_n = 600 MeV (see Figure II.4). For each T_n run and position of the gamma assembly, the D counter assembly was moved to a position where the deuterons associated with photons striking the converters didn't quite fill the D counters.

In order to reduce the number of unwanted triggers from reaction 2.1, the D counters and everything in the gamma assembly with the exception of the spark chambers were divided into upper and lower sets so that the apparatus could be triggered on up-down or down-up deuteron-gamma pairs only. The approximately 6-inch wide vertical separation of the upper and lower sets also allowed the gamma and D counter assemblies to be placed in the beam to collect the extreme backward-gamma forward-deuteron events.

Whenever the fast (nsec) electronic logic decided an event had occurred, the spark chambers were fired, and the slow (μsec) electronic logic recorded the coordinates of all sparks, the timing and amplitude of pulses from the counters and RF, and the beam intensity. The slow

logic then sequentially sent this data to an on-line PDP-10 computer which wrote it on magnetic tape. The computer also made on-line histograms of quantities which were useful in monitoring the operation of the apparatus and performing a preliminary analysis of the data.

SECTION B NEUTRON BEAM

For each energy run, deuterons were accelerated by the PPA to a kinetic energy twice the desired T_n. The circulating deuteron beam was spiraled inward onto a 5-inch long by $\frac{1}{2}$-inch high by $\frac{3}{4}$-inch wide beryllium target for a spill time which varied between 2 and 8 milliseconds. Roughly 20% of the deuterons were stripped of their protons by the target and formed a neutron beam tangent to the circulating beam. Such a 0° beam cannot have any polarization since the accelerated deuterons do not.

The neutron beam was defined by a set of three 32-inch long collimators of circular cross section. Each of these consisted of concentric brass tubes with the outermost set in lead surrounded by zinc bricks. The diameters of the collimators and the distances of their centers from the Be target were: 1-inch diam. 34.8 feet, 2.5-inch diam. 148.3 feet, 3.5-inch diam. 186 feet (see Figure II.5). The resulting beam had a 4-inch diameter at half intensity at the hydrogen target with less than 0.3% of the beam outside the 5-inch diameter of the liquid hydrogen (see Figure II.6). The beam profile was measured using a remotely positioned telescope containing a $\frac{1}{4} \times \frac{1}{4} \times \frac{1}{4}$-inch counter with a brass screw in front of it in which the neutrons could interact. The profile was also measured by extrapolating tracks in the deuteron chambers back to the hydrogen target.

A 1-inch (4.4 radiation lengths) thick lead plate placed just upstream of the second collimator reduced the gamma contamination from $\sim$ 10% to less than 0.2% where it was difficult to detect. Charged particles were removed initially by the synchrotron ring magnets and just downstream of the third collimator by an 18D36 magnet run at

$\sim$ 12 kilogauss which would bend 2 GeV/c positive particles 9° downward. To reduce interactions in the air, there was a 20-foot long vacuum pipe beginning 8 feet after the sweeping magnet. A .05-inch thick beam anti-counter, AB, was placed after the vacuum pipe and followed by a 7-foot long helium bag which ended just outside the gamma cart circle.

The absolute intensity of the beam as measured by the proton monitor telescope using the known cross section for np elastic scattering[51] for 30° protons in the laboratory could be determined to about ± 15%. No attempt has been made to use this information to determine an absolute cross section in this experiment since errors in the absolute efficiency of the apparatus are of the same order, and the total cross section of $n + p \rightarrow d + \gamma$ is already known to ± 10%.[50] Typical average intensities during the four energy runs, $T_n \cong 475$, 560, 625, 750, were 2.8, 5.7, 5.1, 12.0 x 10^6 neutrons/sec through the hydrogen target. The trend toward higher intensities at higher energies is due to increased forward peaking of the stripped neutrons in the laboratory frame. The instantaneous intensity sometimes went as high as 10^9 neutrons/sec, mostly due to spikes in the spill.

Although only an approximate description of the neutron beam spectrum is needed for analysis of this experiment, a fairly careful description will be given here for experimenters who may be interested in stripped deuteron beams. Figures II.7 and II.8 show sample neutron spectra for all four energy runs with $\theta_d^* \cong 135°$. The graphs labeled "raw" have the cross section for $n + p \rightarrow d + \gamma$ still in them. These histograms were made by the PDP-10 computer during analysis and show the number of events which closely fit $n + p \rightarrow d + \gamma$ kinematics vs T_n as measured by TOF. Reference to Figure I.2 shows that the total cross section does not change much in the region from T_n = 500 to 700 MeV,

which is the region of the two central energy runs, but undergoes changes by factors of about 1.6 and 3 in the regions of the 475 and 750 MeV runs. To obtain the spectra for these runs corrected for $d\sigma/dT_n$, a linear fit to the cross section in each region was made, and the number of events in each T_n bin was divided by the fitted cross section normalized to 1 at the median T_n. The simple linear approximation is justified by the relatively small change of the spectrum in the worst case, $\langle T_n \rangle \cong 750$. The median of each spectrum is shown by an arrow.

Table II.1 gives the standard deviation of these approximately Gaussian spectra and calculated factors contributing to these widths. There is a basic width due to Fermi momentum of the neutron inside the deuteron, a broadening due to energy loss by the deuteron as it penetrates the Be target, and additional width due to variations in the deuteron momentum with spill time and to TOF resolution. The variation of T_n due to the TOF resolution, Δt, is given by

$$\Delta T_n = (m_n c/d)\Delta t \; (\langle p_n \rangle / m_n c)^3 \quad ,$$

where m_n is the mass of the neutron, d is the distance over which the TOF was taken, and $\langle p_n \rangle$ is the average momentum of the neutron in the laboratory. The TOF resolution was ± 1.2 nsec for the lower three energies and ± 1.5 nsec for $\langle T_n \rangle = 750$. The energy loss by the deuteron due to ionization in the target (± 2.5 inches of beryllium) was a flat distribution and its equivalent standard deviation was taken to be 0.7 times its width. The root mean square value of the momentum of the neutron inside the deuteron, $\langle P_{int}^2 \rangle^{\frac{1}{2}}$, was chosen to give the best fit of the calculated widths to the measured widths and had a value of 26.5 ± 2 MeV/c. This value agrees fairly well with that calculated from the Hulthén wave function, $\langle P_{int}^2 \rangle^{\frac{1}{2}} = 28.5$ MeV/c.

SECTION C LIQUID HYDROGEN TARGET

The target protons were contained in a cylindrical flask of liquid hydrogen 2 inches thick along the beam direction and 5 inches in diameter. Two inches was chosen as a compromise between thickness for rate and thinness for defining the interaction point and reducing the multiple scattering of the emerging deuteron. Although liquid hydrogen targets must be surrounded by vacuum for thermal insulation while the hydrogen is near atmospheric pressure, the consideration of multiple scattering requires thin walls facing the beam direction. The resulting flask design is shown in Figure II.9. Two "boiler end" shaped domes of .010-inch thick Mylar contained hydrogen gas at the same pressure as the liquid hydrogen which could then be confined between two flat walls of .002-inch (2-mil) thick H-film. H-film was also used in the form of a $\frac{1}{2}$-inch thick ring as the basic structure to which all other parts of the flask were glued with epoxy. Resistors used to detect liquid hydrogen were placed at the bottom of the dome sections to make sure there was no liquid there. The entire flask was wrapped with 10 layers of $\frac{1}{4}$-mil aluminized Mylar and appears as a silvery ball inside the evacuated target housing in Figures II.2 and II.3.

The flask was suspended in the target housing by fill and vent tubes, which connected to a standard PPA liquid hydrogen target system with a 15-liter reservoir fed via a transfer line from a 100-liter dewar. The lower part of the target housing was a special "gaping jaws" design to eliminate flanges and other material which could convert gamma rays and cause sharp local changes in gamma detection efficiency. The only target housing through which the gamma rays passed was a .015-inch thick Mylar vacuum window.

SECTION D COUNTERS

Table II.2 describes the 17 scintillation counters and one Čerenkov counter used in the experiment. The Čerenkov counter was used to monitor the beam spill intensity and will be discussed later in this section. All other counters had plastic scintillant and acrylic plastic light guides. Five-inch diameter Amperex XP 1041 photomultiplier tubes were used for the four large D counters, and 2-inch RCA 8575 tubes were used for all other counters. The thin counters, N and AB, were wrapped with 5 layers of $\frac{1}{4}$-mil aluminized Mylar instead of tape to minimize material in the beam. Efficiencies were measured by counting triple coincidences with two small counters in a charged test beam.

Since TOF measurements were an important part of this experiment, variations in the time between the passage of a particle through a counter and the production of an electronic logic pulse had to be carefully taken into account. Conditions affecting this delay included high voltage drift, position where the particle struck the counter, and photomultiplier pulse height.

Slow changes in the high voltage on the photomultiplier tubes of less than 10 V or 0.5% were difficult to prevent but could cause a maximum timing shift of only 0.2 nsec (0.1 nsec for most of the counters) and did not seem to be serious.

The variation of timing with position was studied in a charged test beam for the D, G, and N counters by placing them on a movable stand between two fixed $3\frac{1}{2} \times 3\frac{1}{2}$-inch counters which defined the beam size. The average TOF of beam particles between one of the small counters and different positions on the counter being tested was measured to an accuracy of ± 0.1 nsec at each position. Taking the TOF

for the position on the longitudinal axis of the counter nearest its light guide to be zero, the delay as a function of position is shown in Figure II.10 for the D3 counter and one of the four identical gamma counters. These functions of delay for a matrix of positions on each counter were used by the computer subroutines which calculated corrections to the TOF measurements in the experiment.

The variation of timing with photomultiplier pulse height was also studied in the charged test beam, although final measurements had to be made under actual running conditions. In the test beam, counters were operated at raised high voltages so that they produced 2.0 V pulses. The delay as a function of the attenuation of these pulses was found to be given by

$$\Delta t = \frac{b\delta}{h}\left(1 - \frac{h}{A}\right) \quad , \tag{2.2}$$

where δ = 0.1 V was the discriminator threshold, $b \cong 2$ nsec was the rise time of the pulses, h was the amplitude of the pulses for which the delay was taken to be zero, and A was the amplitude of the pulses for which the delay was being measured. This formula is exact for pulses of triangular shape, and was found to hold within ± 0.1 nsec for pulses between 0.15 V and 1.5 V in amplitude. The actual formulas used to correct for the effect of pulse height were determined from the data because b and h in equation (2.2) depended on position in the counter, high voltage, and the analog-to-digital converter (ADC) used to measure the pulse height. In addition, a correction had to be made to the basic formula for the gamma counters when they detected several electrons and produced a pulse height greater than 1.5 V.

During the experiment, the resolution (σ) of the individual counters for average particles they detected (about twice minimum

ionizing) was ± 0.50 nsec for the N counter, ± 0.40 nsec for the gamma counters, and ± 0.75 nsec for the D counters. Part of the error for the D counters was due to an uncertainty in the position of the multiply scattered deuteron after its track was extrapolated 30 to 60 feet. The typical error in position of ± 1.5 inches gave rise to a timing error of ± 0.3 nsec. Timing corrections and errors will be discussed further in section III.C.

The spill intensity monitor (SIM) was a Čerenkov counter with a lucite radiator mounted about 10 inches from the internal target. A 0.04 μF capacitor was connected from the anode pin of this counter's photomultiplier tube to ground, so that, in parallel with the 50-ohm termination of the signal cable, it integrated the output of the counter over 2 μsec. Whenever the electronic logic triggered, a 25-nsec segment of this integrated signal was sent to a charge sensitive analog-to-digital converter to provide a measurement of the beam intensity for a time preceding a trigger roughly equal to the sensitive time of the spark chambers. This measurement was important because the beam intensity varied by a factor of several hundred during the very irregular spill and the efficiency of the apparatus for finding one deuteron associated with one gamma ray was a function of the intensity due to spark chamber loading. The use of the SIM reading in measuring this efficiency will be discussed in section III.G.

SECTION E SPARK CHAMBERS

The construction of the spark chambers is shown schematically in Figure II.11. All eight chambers had magnetostrictive readout with x and y planes wound on opposite sides of 3/8-inch thick G-10 epoxy fiber glass frames. The dimensions of the active areas in inches were: D1 & D2 18 × 12, D3 & D4 24 × 18, D5 D6 G1 & G2 38 × 24. The deuteron chambers had the long dimension horizontal, while the gamma chambers had it vertical. The deuteron chambers were located 6.31, 11.31, 26.31, 27.81, 79.31, and 84.68 inches downstream from the center of the hydrogen target. They had a narrow frame member on the gamma side to minimize material which could convert gammas prematurely.

Since the major consideration in designing the chambers was minimum material in order to reduce multiple scattering of the deuteron and interactions in the beam, .002-inch diameter beryllium-copper wires were used. The wire spacing was 0.635 mm or 40 wires/inch. Such thin wires do not charge rapidly enough for good spark formation, so a .0005--inch thick aluminum "capacitance charging" foil was fastened to the outside of the Aclar pressure window and connected to the same bus as the wire plane. It was found that the same results as two full foils could be obtained with one of them merely ringing the active area of the chamber and extending 2 inches into it. Since the foils were delicate, they were covered with .001-inch Mylar.

The clearing characteristics of the chambers are shown in Figure II.12. These curves were taken by operating one of the middle-sized chambers in a charged test beam and measuring its efficiency as a function of the delay of its firing after the passage of a particle. The arrows at 0.7 μsec in the figure indicate the delay required for

the experiment's electronic logic to decide on an event and deliver the high voltage pulse to the chambers. The test chamber was pulsed at -4.0 KV and the dc clearing potential applied to the high voltage plane.

Due to the bulging of the pressure windows, over half of an ionization trail in a chamber was not between the wire planes. Electrons from the outer region on the high voltage side of the chamber diffusing into the space between the planes caused the long tails on the clearing curves in part (a) of Figure II.12. An external, grounded clearing plane of $\frac{1}{4}$-mil aluminized Mylar was used outside the high voltage side of the chamber so that a negative clearing field could push electrons away on both sides of the high voltage plane and thus clear the chamber. The curves in part (b) of Figure II.12 were obtained using the clearing plane.

The addition of isopropyl alcohol vapor to the 90% neon 10% helium gas mixture steepened the falloff of efficiency with delay. About 15% of the gas was allowed to flow through the top half of a 2-gallon jug half filled with alcohol and kept at 20° ± 1°C. The total gas flow for all eight chambers was 1.5 standard ft^3/hr.

After consideration of the results of these tests and others performed with the chambers in their final positions, a clearing potential of -40 V for all chambers was decided upon for use during the experiment.

Whenever the fast electronic logic decided an event had occurred, high voltage pulses were delivered to the chambers and their fiducial wires by the system diagramed in Figure II.13. The event trigger logic signal was amplified to the point where it could trigger a spark gap (5 kV) by an E.G. & G model HV 100/N high voltage pulser. The spark gaps were the same ones designed for the first Princeton

$n + p \rightarrow d + \gamma$ experiment by K. Goulianos. These gaps were extremely reliable and did not need to be replaced with a new set until near the end of the experiment after over one million pulses. They were pressurized with nitrogen gas at about 10 psig. The spark gap circuits were located within a few feet of the chambers they pulsed so that the cables connecting them to the chambers could be kept short. This meant the circuits were close to the hydrogen target, so, as a safety precaution they were enclosed in gas tight containers filled with nitrogen slightly above atmospheric pressure. Three of the spark gap circuits are visible in Figure II.3. The deuteron chambers were pulsed from 5000 pF capacitors at 4.4 kV and the gamma chambers at 4.2 kV. The four fiducial wires of each chamber were connected in series and pulsed from 2500 pF capacities through 100 Ω resistors.

Full discussions of chamber resolution and efficiency are postponed to sections III.B and III.G, but a few typical numbers are given here. The location sparks could be established with an error on the order of the wire spacing, 0.6 mm, or better. This error, however, was much smaller than that introduced by multiple scattering of the deuteron in the target assembly or by the spread of the electron shower from the gamma ray. Spark formation efficiencies were typically better than 99%. The magnetostrictive read-out of most wands was also nearly perfect, but some wands had typical efficiencies of only 96% and one of them dropped to 84% when the spark gaps began to go bad. Even such low efficiencies were not serious, however, because only one of each pair of chambers was required to fire, and because the efficiency could be accurately monitored using $np \rightarrow d\pi^\circ$ events.

In order to reduce the spread of the electron shower in the gamma chambers, both chambers were mounted as close to the lead converters as

possible. The first gamma chamber was mounted only 1/8 inch behind the converters, and the two chambers were $\frac{3}{4}$ inch apart. Pressure differences between the gas systems of the two chambers had to be eliminated because their bulging pressure windows were in contact. The G chambers were mounted with their high voltage planes facing toward each other, with a clearing plane between them. The clearing plane was dc grounded through a 1-megohm resistor, and kept at the same potential as the chamber high voltage planes by pulsing it with a "fiducial" capacitor whenever the chamber was pulsed.

SECTION F ELECTRONIC LOGIC

The electronic logic performed the following functions: deciding when an event or proton monitor count had occurred and triggering the spark chambers and/or the rest of the logic, collecting information about either type of trigger and reducing it to digital form, and sending this information to the on-line computer to be written on magnetic tape. The first of these functions was performed by the fast logic, which handled pulses between 3 and 200 nsec in duration (width), and consisted of standard commercial NIM modules. The fast logic also provided gating, pulse shaping, and delay of signals used by the slow logic for TOF measurement. The slow logic handled pulses between .2 μsec and .05 sec wide and consisted of modules designed by T. Droege and assembled by the PPA electronics shop.[52] The data collection modules of the slow logic accepted pulses from the counters and chambers, measured their amplitude and/or timing and scaled certain coincidences, converted this information into digital form, and stored it until interrogated. The rest of the slow logic coordinated the interrogation of each data collection module and the sending of its information to the computer.

Diagrams of subsystems of the electronic logic are shown in Figures II.14 and II.16 through II.18. Logic units are represented as rectangles with arrowheads for inputs and dots for outputs. The electronic or logical function of each unit, such as AND for a coincidence circuit, is shown inside its rectangle. Above and below the rectangle, the use to which a unit was put, such as GT for "gamma top," and the width of its output pulse is sometimes also shown.

The event trigger logic is diagramed in Figure II.14. An event

could be one of two types depending on whether the top gamma and bottom deuteron counters fired (GT-DB) or the bottom gamma and top deuteron counters did (GB-DT). The formation of the latter type of trigger is not shown in the diagram, but it was identical to that of the former type. The fast logic formed a GT-DB coincidence from what were basically two triple coincidences: front and rear top G counters plus the N counter, which formed GT, and front and rear bottom D counters plus N, which formed DB. These triple coincidences were complicated by several factors. In order to compensate for the different locations of the C and D counters as data was taken at different angles and still maintain tight coincidences, variable N-G, N-D, and G-D delays were necessary. The dependence of the average velocity of the deuteron on T_n had to be taken into account for the N-D delay, and the G-D delay was set equal to the N-D delay minus the N-G delay. In order to veto events where the supposed neutron or photon was really a charged particle, signals from the beam anti-counter, AB, and the two GA counters were fanned in to form a single veto signal which was fanned out to separately veto the GT and GB coincidences and the proton monitor. The 8-nsec jitter caused by the 4-ft length of the D counters was reduced to less than 2 nsec by averaging the time of signals from the front and rear counters, which had their tubes at opposite ends, using a "position compensator" (PC) circuit designed by C. Friedberg. A schematic circuit diagram of the position compensator is shown in Figure II.15. The PC signal, whose arrival time varied with the TOF of the deuteron, triggered a DB coincidence if it fell within the 50 nsec gate provided by the delayed N signal. This N gate width accepted all deuterons from $d\gamma$ and $d\pi^\circ$ events while excluding 80% to 95% of all protons. The PC deuteron signal was used only in the trigger logic;

TOF measurements were made separately for each counter. The pulse widths and relative delays are shown in the upper right hand corner of the diagram.

The proton monitor logic is diagramed in Figure II.16. A coincidence was formed between the PM1 counter and the position--compensated signal from the two photomultiplier tubes of the PM2 counter. This PM signal was vetoed by a signal from the anti fan-out whenever any of the anti-counters detected a particle, so the proton monitor had the same dead-time as the event logic. PM was placed in coincidence with the delayed signal from the N counter to form PMN1. After suitable delay, PM also provided the stop signal for the measurement of the recoil proton's TOF. PMN1 was scaled and used as a second gate for the N signal to ensure that a PMN2 coincidence was always initiated by N and never by PM. A final coincidence, PM/8, was formed between PMN2 and every eighth PMN1 pulse. PM/8 was used to trigger and gate the slow logic associated with proton monitor measurements and to supply the start signal for the measurement of the recoil proton's TOF. Only every eighth count was used because otherwise the apparatus would have spent most of its time recording proton monitor triggers.

Since the rf accelerating voltage of the PPA (RF) was used to mark the beginning of the neutron's flight, it was necessary to isolate the wave crest or "bucket" associated with the particle bunch which gave rise to the neutron causing the event and use it as the start signal for the measurement of the neutron's TOF. This was done by the logic shown in the top half of Figure II.17. The attenuated RF signal was first converted to a train of 3 nsec pulses by a discriminator. The appropriate pulse was then selected from this train by coincidence with

the signal from whichever pair of G counters fired. The G OR delay was adjusted to compensate for the differences in timing between the different locations of the G counters. The output of the first coincidence, RF #1, was not used as the start signal but was used instead to gate the RF pulse train delayed by 30 nsec. This was done to avoid trouble in the case shown at the right of the diagram where the G OR signal would have become the start signal because it arrived in the middle of the RF pulse.

The slow logic is diagramed (very schematically) in Figure II.18. Upon receiving a trigger from either the event logic or PM/8, the control and sequencing systems provided clearing, gates, timing and other services while the data collection modules, described in the paragraphs below, received data. After sufficient collection time, the control and sequencing system signaled the scanning modules to interrogate the data collection modules. A pulse from a scanner caused a collection module to deposit a data word on the 12-bit data bus connected to the output modules. One of the output modules was the link to the on-line PDP-10 computer; others included a Nixie read-out for word-by-word examination, a paper tape punch, and an electric typewriter. If a trigger was from the event trigger discriminator, all scanners were activated and all data collection modules were interrogated. These included the event register, 16 spark chamber modules, 10 analog--to-digital converters, 10 time-to-digital converters (digitimes), 9 scalers, and the spill clock. If a trigger was from PM/8, only the PM scanner, which interrogated the spill clock, SIM ADC, and PM digitime, was activated.

The event register received pulses from the N, D, and G counters and set one bit of its 12-bit word for each of the counters according

to whether or not the counter delivered a pulse during the event gate.

The 16 spark chamber modules, called gates, provided dc power to and received pulses from the amplifiers attached to the magnetostrictive delay lines of the spark chamber wands. Each gate measured the times between its reception of the first pulse and up to four following pulses by having the first pulse start four clock scalers and each succeeding pulse stop one of them. The first pulse received was that of the fiducial wire nearest the amplifier, typically followed by one or two sparks and the second fiducial. The computer could distinguish the second fiducial because of its fixed position. The slow logic sequencing system provided five pulses, separated by a fixed short time, which arrived after the second fiducial pulse to start and stop all scalers if normal pulses failed to do so. The clock rate was 16 MHz so that with a magnetistrictive pulse velocity of about 5 mm/μsec, the 4095 counts available in the 12-bit scalers easily covered one-meter wands at about 3 counts/mm.

The analog-to-digital converters measured the charge contained in pulses from the N, G, and D counters. The full range of the ADC's was 127 units at about ½ volt-nanosecond per unit into the 50-Ω input. The amplitudes of pulses from minimum ionizing particles in the counters were set to be about 6 to 10 units to insure that pulses from highly ionizing particles or showers could be analyzed. This setting provided sufficient accuracy to correct TOF measurements for the effects of pulse height variation.

The slow logic modules used to measure TOF, called digitimes, required three pulses from the fast logic: start, stop, and a gate. The logic providing these pulses is shown in the bottom half of Figure II.17. The start signal came from the counter being timed,

through its discriminator, a long cable for delay, another discriminator, and an "or" circuit. A 200-nsec wide gate, the stop pulse, and the "late start" pulse came from the event trigger pulse through fan-outs. The "or" circuit before the digitime start input allowed the digitime to be started by the late start pulse if there was no pulse from the counter. The late start came from the same source as the stop so that a specific digitime reading corresponding to 15 nsec signified that the counter had not fired.

The digitimes had a full range of $\sim$ 300 nsec divided into 4096 counts or $\sim$ 14 counts/nsec. They were individually calibrated using continuously variable delay boxes, accurate to 0.02 nsec. They were found to be linear to $\pm$ 1 count in the central 200 to 270 nsec of their range, and the calibration of each digitime was reproducible to $\pm$ 1 count or $\pm$ 0.07 nsec over this part of its range. All digitimes were actually used only in the central 150 nsec of their range or less.

The total number of occurrences of each of the following 9 types of coincidence was recorded on a 24-bit (2-word) scaler at each event: event triggers, GT-DB, GB-DT, PMN1, NM (neutron monitor), GT, GB, DT, DB.

The spill clock measured the time in units of 0.05 msec at which an event or proton monitor trigger occurred relative to the acceleration cycle of the PPA. The clock was reset and started at the initiation of each cycle (19.5 times per second) and stopped by the trigger pulse.

SECTION G HELIUM BAGS

The helium bags used to reduce the multiple scattering of the deuteron are worth mentioning because they were made of Mylar instead of the more usual polyethylene. Helium and air diffuse through Mylar about ten times slower than through the same thickness of polyethylene. This is important because if our large bag had been made of 4-mil polyethylene, it would have contained about 30% air by weight after just one week without flushing. Mylar has not been used much in the past for helium bags because it is difficult to bond. Although RTV 731 silicone rubber will bond two strips of Mylar together, bags which were simply glued together with this sealant tended to fall apart at the seams. This problem was overcome by the use of 3M type 4016 1/16-inch thick double-sided urethane foam tape to provide mechanical strength as an adhesive and to space the Mylar sheets so that the RTV 731 could cure properly and seal the joint. Figure II.19 shows such a seam in cross section.

Our large bag was 22 ft long, 3 ft × 4 ft at the upstream end, and 8 ft × 6 ft at the downstream end. It was made of 5-mil Mylar. The purpose of the large bag was to reduce multiple scattering and thus allow accurate extrapolation of the deuteron track to the point where it passes through the D counters so that the proper timing correction could be made. Two smaller bags with 2-mil thick windows just filled the spaces between the D2 and D3 chambers and the D4 and D5 chambers. There was also an 8-inch diameter, 7-foot long bag with 1-mil windows to reduce interactions of the neutron beam after the AB counter.

CHAPTER III

DATA REDUCTION AND ANALYSIS

SECTION A INTRODUCTION

The task of the apparatus was completed when it had provided numbers on magnetic tape describing over one million events, about 3% of which were $n + p \rightarrow d + \gamma$. The task of the data reduction and analysis was to transform these numbers into four angular distributions for this reaction, one for each energy, in the center of mass of the n-p system. A point on the angular distribution at one of the four energies is given by the number of $d\gamma$ events in an angular bin divided by the relative efficiency of the apparatus and data reduction for that bin and by the number of incident neutrons. The number of $d\gamma$ events in each angular bin was determined by means of the data reduction and analysis computer program, Hist, which converted spark chamber and counter information for each event on magnetic tape into kinematic quantities which were compared with the kinematics of $n + p \rightarrow d + \gamma$. The efficiency was the product of individually determined efficiencies of two types: calculated and measured. The calculated efficiencies included the geometrical acceptance of the apparatus, the gamma-ray conversion efficiency, and the loss of deuterons due to interactions. The geometrical acceptance and many other useful quantities were calculated by a Monte Carlo computer program, DGMC, which simulated $d\gamma$ events and noted what fraction of them were detected. There was also a similar Monte Carlo program, DPMC, which simulated $d\pi^\circ$ events. The probability that a gamma ray striking one of the lead converters would produce a detectable electron shower was calculated by a separate "gamma efficiency" Monte Carlo program. The measured efficiencies, such as those of the spark chambers and data reduction, were determined by Hist from its knowledge of its progress during the data reduction.

Measurement of these efficiencies was made possible by the large number of $d\pi^\circ$ background events. Hist also totaled proton monitor counts to obtain a number proportional to the number of incident neutrons.

Hist presented most of its information in the form of histograms of the number of events as a function of any of the 165 variables in the histogram block that the user desired. "Event" as used here could mean any occurrence which triggered the electronic logic, including proton monitor counts, or could be limited to very specific types of triggers by cuts on any of the variables in the histogram block. Hist was written in two versions, on-line and off-line. The on-line version read its data from the experiment through the computer link to the slow logic (PDP-10 real time access device), stored it in a buffer, and wrote it out again on magnetic tape while processing it and making histograms. Only the original data was written on tape--no computed quantities were saved. The off-line version read its data from the tapes written by the on-line version. The two versions were assigned different types of quantities to histogram. The on-line version histogramed quantities useful for the examination of the functioning of the apparatus. The off-line version histogramed kinematic and other quantities useful for the separation of $d\gamma$ events from background.

The main program, with some bookkeeping subroutines, read and checked the histogram control information provided by the user, set up the required arrays, accepted run information from the user or read it from the desired tape, read constants which depended on the run information, and read the first event. Events were completely processed, one at a time, by the subprogram Spec. After Spec processed each event, Hist incremented the appropriate histograms, and read the next event. When the run was over or the last event on the tape processed, Hist

called the Finish subroutine to calculate proton monitor and efficiency information, and print the results. Hist then printed out the histograms.

When Spec received an event, it determined whether the event was from a proton monitor trigger or a normal trigger and processed it accordingly. If an event was from the proton monitor, Spec flagged it as such, calculated the TOF of the recoil proton, and recorded the flag, TOF, spill time, and SIM ADC in the block of histogram variables. When Spec received a normal event, it did some bookkeeping with the readings of the scalers, spill time clock, and SIM ADC, and then called six subprograms: Scheck, Tcheck, Trkfit, Gamfit, Timing, and Analys. Scheck examined the readings of the 64 spark chamber wand scalers and converted them to millimeters in preparation for the track fitting routines. Tcheck examined the contents of the event register to determine which counters had triggered. Trkfit attempted to fit lines to all the appropriate combinations of sparks in the deuteron chambers, returning the parameters of the deuteron track if there was one and error codes if there was more or less than one. Gamfit located the gamma conversion point if there was one and only one and returned error codes otherwise. Timing converted counter information into the velocities and momenta of all particles, incorporating all necessary corrections. Analys calculated kinematic quantities and compared them with the values of the same quantities predicted by the kinematics of $n + p \rightarrow d + \gamma$.

The Monte Carlo programs DGMC and DPMC made histograms of the number of simulated events vs any of the variables they generated for each event. The simulation of an event had three parts: generation of the "actual" quantities of the event and tests of whether or not the event was accepted by the apparatus, generation of "measured" quantities

from the "actual" quantities using given measurement errors, and kinematic analysis using the "measured" quantities. Although only the first part of DGMC was necessary to compute the acceptance of the apparatus, the full versions of both DGMC and DPMC were indispensable for other uses. Before any data was taken, preliminary versions of both programs were run for each beam energy to determine the optimum position of the D counters to match each of the nine positions of the gamma assembly and to determine the proper settings of electronic delays and gate widths. DGMC also showed the mean value and the extent of the θ_d^* bin associated with each position. Estimates of measurement errors were checked by comparing histograms of simulated events vs various kinematic quantities with histograms of real events vs the same quantities. These checks were important because the errors on measured variables were necessary input for the least-squares fits used to separate $d\gamma$ events from background. DGMC and DPMC also showed the different shapes of signal and background in simulations of the histograms used to perform the separation.

SECTION B RECONSTRUCTION OF TRACKS

This section describes the reconstruction of particle tracks, hence angles, in real space from the readings of the spark chamber wand scalers which was performed by subroutines of Spec. First, it is necessary to describe the coordinate system in which this was done.

The laboratory coordinate system is sketched in Figure III.1. The origin was located at the center of the hydrogen target, and the $\hat{z}$ axis was defined to be along the beam direction pointing downstream. The $\hat{y}$ axis was vertically upward, and the $\hat{x}$ axis completed a right-handed coordinate system by pointing horizontally toward the deuteron side of the apparatus. The polar angle, θ, of a particle track was the angle between the $\hat{z}$ axis and the track, and its azimuthal angle, φ, was the angle between the $\hat{x}$ axis and the projection of the track onto the $z = 0$ plane.

Of the three moving particles in $n + p \rightarrow d + \gamma$, the apparatus measured the direction of only two, the deuteron and gamma ray. The direction of the neutron was known in advance from the beam geometry to be $\theta_n = 0.0 \pm 0.8$ milliradians. The track of the deuteron was reconstructed first, and the "interaction point" was defined to be at the intersection of the deuteron track with the mid-plane of the target ($z = 0$ plane). Since the direction of a gamma ray is difficult to measure directly from its electron shower, the gamma assembly was designed to measure the location of the vertex of the shower only, and the gamma track was formed by connecting this point with the interaction point. Since the deuterons were confined to a forward cone of $\sim 15°$ half-angle, the error in the position of the interaction point due to the 2-inch target thickness was essentially $\pm$ 1 inch in its z

coordinate. This resulted in a non-Gaussian (flat) uncertainty in θ_γ of 1 inch x (sin θ_γ)/r, where r was the distance from the origin to the gamma shower vertex. This error dominated other errors in θ_γ and peaked at .013 radians for θ_d^* near 40°. Fortunately, this uncertainty was not serious for many of the angular bins where it was large, because for large gamma-ray angles the kinematic separation of $d\gamma$ events from $d\pi^\circ$ background depends mostly on the deuteron direction.

The error in the deuteron direction was completely dominated by the multiple scattering of the deuteron in the material of the target assembly, the N counter, and the first two D chambers. Even if only one chamber of each of the three pairs fired, the chamber resolution of ± 0.5 mm combined with the 2-meter separation of the first and third pair would give an angular resolution of ± 0.35 milliradian. The average amount of material traversed by a deuteron up to the second D chamber included 0.20 grams of hydrogen, 0.19 grams of carbon, and 0.0018 grams of copper. This resulted in a mean scattering angle of from 1.7 milliradians for the fastest deuterons measured (1600 MeV/c) to 6.7 milliradians for the slowest (700 MeV/c).

Reconstruction of both tracks began with the subroutine Scheck which examined the readings of the four scalers associated with each wand and set flags for error conditions. Scheck then converted scaler readings from good sparks into millimeters. The conversion was done using the known velocity, in millimeters per scaler count, of magnetostrictive pulses in the delay line of each wand. This velocity was equal to the fixed distance between the fiducial wires divided by the scaler reading of the fiducial pulse. The reader should note that the "sparks" reconstructed by Scheck were only one-dimensional, so that the number of possible two-dimensional spark locations in a chamber was

the square of the number of physical sparks in that chamber. Events which did not have at least one "spark" in each view for each pair of chambers were flagged as having failed Scheck. The proportion of events failing Scheck varied from 0.02% to 2.0% and was typically about 0.1%.

Trkfit attempted to reconstruct a deuteron track by fitting a straight line to every combination of possible spark locations in the D chambers. This was the most time-consuming procedure in all of the data reduction, so the number of possible combinations was lessened in two ways. First, sparks were eliminated which were in areas of the chambers where they could not possibly lie on a line which extrapolated through the target and the D counters. Second, if there was a pair of sparks in D chambers 3 and 4 or in 5 and 6 which were suitably close in x or y, then they were treated together as a pair. A root-mean-square deviation,

$$\chi_L = \left[\frac{1}{N-2} \sum_{i=1}^{N} \left[(x - x_i)^2 + (y - y_i)^2 \right] \right]^{\frac{1}{2}} ,$$

was computed for each fitted line, where N was the number of (3-dimensional) sparks on the line. If $\chi_L \leq 5.0$ mm for a line, and the line extrapolated through the hydrogen target and the D counters, then it was considered a good line. The cut on χ_L was quite loose since the mean value of χ_L for all good lines was about 1 mm. If two good lines had three or more sparks in common, only the line with the most sparks on it was saved, or if they had the same number of sparks, the line with the best fit was saved. If there was no good line, or if there were two or more good lines, the event was flagged as having failed Trkfit. The proportion of events failing Trkfit varied from

4.0% to 30.7%, depending primarily on the flux of charged particles from the hydrogen target passing through the D counters. This inefficiency will be discussed in some detail in section III.F. When Trkfit succeeded in reconstructing a deuteron track, it noted which wands failed to have sparks on the track. The number of failures for each wand was totaled, and the percent inefficiency was printed out by Hist.

Gamfit attempted to locate the gamma shower vertex by sparks in the first gamma chamber, G1, where the shower was still compact. If electrons in the shower were just far enough apart for their magnetostrictive pulses to cancel, so that they were not detected on one or both of the G1 wands, then they would be farther apart in G2 and detected there separately. Gamfit began with the top view (horizontal wand) of G1 by combining sparks within 30 mm of each other and replacing them with a "spark" at the mean of their positions. This procedure was repeated for G2 (but with a combining distance of 60 mm) only if no sparks had been found by Scheck in the top view of G1. The side views (vertical wands) were then treated in the same way. If an event had one and only one spark in each view of G1, it was passed by Gamfit, and the locations of those sparks determined the coordinates of the gamma shower vertex relative to the G chambers. If an event had no sparks in either view of G1, it was failed unless there was one and only one spark in each view of G2. If an event had two or more sparks in either view of G1, it was failed unless there were sparks in G2 within $\pm$ 45° relative to the normal to the chamber plane behind one and only one of them.

There was a modification of the above criteria which was only important when the gamma assembly was in the neutron beam (position 9, $\theta_d^* < 16°$). In that position between 1% and 6% of the events had an

extra spark near the center of the chamber. Sparks in the vertical wands within ± 2.5 inches of y = 0, where there was no material in front of the chambers, were ignored during vertex location, but if one was found along with a normal spark ($|y_s| > 2.5$ inches), special conditions were applied to sparks in the top view in order to avoid a dip in the efficiency of Gamfit. If there was a spark outside the region above and below the beam, then it was treated normally. If both sparks in the top view were within ± 2.0 inches of the center of the chambers, however, it was impossible to tell which was the normal spark, so their horizontal coordinates were averaged. This resulted in an error in the x-coordinate of the vertex of less than ± 2 inches and typically ± 1 inch for these events or ~ ± 0.02 radians in the direction of the gamma ray. This error was not important because in position 9 the kinematic separation of dγ events depends primarily on momenta and is about 10 times less sensitive to the direction of the gamma ray than it is to the direction of the deuteron.

When Gamfit had located the gamma shower vertex relative to the gamma chambers, it rotated and translated the top view to get the vertex coordinates in real space.

SECTION C RECONSTRUCTION OF VELOCITIES

The subprogram Timing calculated the TOF of the neutron, deuteron, and gamma ray, and knowing the flight paths of the particles from their reconstructed tracks, reconstructed the velocity of each particle and the momentum and energy of the neutron and of the deuteron. The TOF of the deuteron and gamma ray were calculated using the counters which intercepted their tracks. Events for which Tcheck indicated that a counter in the path of a particle track did not fire were flagged as having failed Timing, as were events for which the vertical slopes of the deuteron and gamma-ray tracks were of the same sign.

The time at which each counter delivered a pulse to its digitime was determined relative to the time of the event trigger pulse by converting the digitime reading to nanoseconds. This raw time was then corrected for the effects of the position of the particle in the counter and pulse height. The change in time as a function of the position of a particle in the N, G, and D counters was measured as described in section II.D and stored in the computer in the form of a matrix. Timing subtracted the delay due to position of the track in a counter determined by interpolating the values of the matrix surrounding the point where the reconstructed track intersected the counter. The delay as a function of pulse height was determined from equation 2.2, where h, the amplitude of pulses from minimum ionizing particles, was measured in ADC units for a matrix of positions. The effect of variation of the factor b/h with position, where b was the rise time, was automatically included in the measurements of delay vs position, so $b\delta/h$ was a measurable constant for each counter. For the G counters, equation 2.2 was modified to

$$\Delta t = \frac{b\delta}{h}\left(1 - \frac{h}{M}\right) + 3.9\left(\frac{h}{M} - \frac{h}{A}\right)$$

if the pulse height, A, of an electron shower was greater than a certain value, M. Using both formulas the data could be fit to within ± 0.05 nsec for pulse heights between h/3 and 7h. M was equal to 3h for the front G counters, G1 and G3, and 5h for the back G counters G2 and G4, which produced somewhat smaller pulses.

To compensate for the different electronic delay of signals from each counter, a "tzero" constant was subtracted from the corrected time. Tzero for a counter was equal to its raw time minus the N counter's raw time for a minimum ionizing particle imagined to pass simultaneously through all counters at the point on their longitudinal axes nearest the light guides. Tzero for each G counter was adjusted to produce an average beta of the gamma ray for that counter of 1.0. The final determination of the tzeros for the D counters and RF was made by fitting the reconstructed deuteron and neutron momenta to the kinematics for $n + p \rightarrow d + \pi^\circ$ as described in section III.D.

The velocities of the particles were reconstructed using the fully corrected time from each counter. The deuteron's velocity was first calculated roughly using its TOF from the N counter to the front D counter. This velocity was used to determine the time taken by the deuteron to travel along its track from the interaction point to the N counter (~ 6.5 inches) and from the front D counter to the back D counter (1.5 inches). Thus the time of the interaction, the average time from the two D counters, and the difference in the deuteron timing by the D counters were known. Events for which the two D times

differed by more than 3 nsec ($\sim$ 4.5 standard deviations) failed Timing. The times from the two G counters were averaged in a similar way, using the speed of light to correct for the distance between them, with the same criterion on the difference. The velocity of the gamma ray was then calculated using the average G time and the N time. Cuts were made by Hist to reject events where the beta of the "gamma ray" differed from 1.0 by more than 5 standard deviations. The time of the interaction was calculated again using the average G time and assuming the speed of light for the gamma ray. This interaction time was given a weight of $\frac{3}{4}$ and the interaction time from the N counter a weight of $\frac{1}{4}$ in making a final calculation of the velocity of the deuteron using the average D time. The same weighted average interaction time was used along with the RF time to calculate the velocity of the neutron.

A final correction to the beta of the neutron was necessary to correct for the shift of the internal deuteron beam bunches relative to the rf accelerating voltage as a function of spill time. As acceleration decreased near the maximum of the magnetic field curve, the phase lag of the particle bunches relative to the rf voltage also decreased until it crossed zero just after the maximum magnetic field was reached. A phase lead then grew as the beam was decelerated to allow a long spill (up to 8 msec out of a 51 msec magnet cycle). This phase change resulted in a variation of the beta of the neutron which was given by

$$\beta_n = \beta_{max} \left[1 - \omega^2 (t_{ev} - t_o)^2\right] ,$$

where β_{max} was the uncorrected beta of the neutron, t_o was the time of zero phase lag, t_{ev} was the event time in msec measured by the spill clock, and ω was determined empirically along with t_o. This formula worked for the lowest three energy runs, $T_n \cong 475$, 560, and 625 MeV,

with an error equivalent to a ± 1.2 nsec error in the TOF of the neutron. Values of ω^2 and t_o for these three runs were .00136, .0011, .0013 and 1.3, 1.8, 1.8 milliseconds. For the $T_n \cong 750$ MeV run the above formula failed and was replaced by

$$\beta_n = \beta_{max} \{1 - .0141 [1 - \sin(\frac{\pi}{5} (t_{ev} + 1))]\} ,$$

which fit the data with an error equivalent to a ± 1.5 nsec error in the neutron's TOF.

In addition to the cut on the beta of the gamma ray, Hist also made cuts on the betas of the neutron and the deuteron. The cut on the beta of the neutron was made at 5 standard deviations from the mean and served to remove the few events which were caused by particles other than neutrons or which had a spurious TOF measurement. The cut on the beta of the deuteron was broad enough not to remove any $d\gamma$ events or more than 1% of the $d\pi^\circ$ events yet narrow enough to exclude over half of the triggers where the "deuteron" was really a proton. The effects of all cuts on efficiency are discussed in section III.G.

Once the correct velocities were determined, the momenta and energies of the neutron and deuteron were calculated using the known masses of the presumed particles. These quantities for the deuteron were corrected for energy loss due to ionization in the material of the target assembly and N counter. The error in the momentum of the deuteron due to the over-all error in its TOF of ± 0.7 nsec ranged from 0.74% at $\theta_d^* \cong 99^\circ$ during the $T_n \cong 475$ MeV run to 1.30% at $\theta_d^* \cong 8^\circ$ during the $T_n \cong 750$ MeV run. The errors in the momentum of the neutron due to the error in its TOF of ± 1.2 nsec for the three lowest energy runs and ± 1.5 nsec for the 750 MeV run were 0.88%, 1.05%, 1.20%, and 1.7% for $T_n \cong 475$, 560, 625, and 750 MeV.

SECTION D KINEMATIC ANALYSIS

Using the reconstructed particle angles and momenta, the subroutine Analys calculated useful kinematic quantities and performed three different kinds of Chi-square fits to the hypothesis that an event was $n + p \rightarrow d + \gamma$. The values of χ^2 from two of the fits were used in the separation of $d\gamma$ events from background.

One of the most useful kinematic quantities was the value of the square of the mass of the neutral particle, M_x^2, calculated using all measured quantities except the angle of the gamma ray:

$$M_x^2(n,d) = (E_d - E_n - M_p)^2 - (p_d^2 + p_n^2 - 2p_d p_n \cos\theta_d) \quad .$$

A histogram of events vs $M_x^2(n,d)$ shown in Figure III.2 for a typical angular bin, has a large peak at the square of the π° mass as well as a small peak at zero from $d\gamma$ events. The position of these two peaks relative to one another, which is one measure of the separation of $d\gamma$ events from $d\pi^\circ$ background, was fairly independent of systematic errors in the TOF measurements of the neutron and deuteron. The absolute positions of these peaks, however, was sensitive to these errors. For events with θ_d^* around 0° a small increase in the neutron's TOF caused a large decrease in $M_x^2(n,d)$, while the same increase in the deuteron's TOF caused a small increase in $M_x^2(n,d)$. For events with θ_d^* around 180° the effects were reversed in direction and relative magnitude. Knowledge of these shifts of $M_x^2(n,d)$ allowed the final determination of the tzero constants for the D counters and RF and of the formulas used to make the final correction to the beta of the neutron.

Since $n + p \rightarrow d + \gamma$ is a two-body reaction, all the momenta in an event assumed to be from this reaction should lie in a plane, and the

coplanarity angle should be zero:

$$\theta_{copl} \equiv \sin(\theta_d) \sin(\varphi_\gamma - \varphi_d) = 0 \quad . \tag{3.1}$$

If this is so, conservation of energy and momentum yields the following three equations:

$$p_d \sin\theta_d = p_\gamma \sin\theta_\gamma \quad , \tag{3.2}$$

$$p_d \cos\theta_d + p_\gamma \cos\theta_\gamma = p_n \quad , \tag{3.3}$$

$$p_\gamma + E_d = M_p + E_n \quad . \tag{3.4}$$

(Equations (3.2) and (3.3) are illustrated by the kinematic ellipse shown in Figure II.4.) Since every variable except p_γ was measured, the above four equations, (3.1) through (3.4), with one unknown allow a three-constraint fit of an event to the kinematics of $n + p \rightarrow d + \gamma$.

To perform the first of the three types of fit, Analys minimized χ^2 by varying p_n, p_d, θ_d, and θ_γ in units of their standard deviations, subject to the two constraints of energy-momentum remaining if θ_{copl} was ignored. The minimum Chi square of this fit was called χ^2(no copl). The full three-constraint fit, χ^2(3 deg), was obtained by adding the square of θ_{copl} in units of its standard deviation to χ^2(no copl). Histograms of events vs χ^2(no copl) and χ^2(3 deg) for a typical angular bin are shown in Figures III.3 and III.4. An additional type of two--constraint fit was performed by ignoring the measured value of θ_γ. The minimized value of Chi square for this fit was called χ^2(no θ_γ).

SECTION E SEPARATION OF dγ EVENTS FROM BACKGROUND

The separation of dγ events from background was performed in two distinct ways by using the two different 2-constraint Chi square fits. This was done to avoid having to trust an elaborate and expensive Monte Carlo simulation of the shape of the background under the dγ peak in the 3-constraint Chi square fit. The method of both separations was similar and is described below using the energy-angle bin $T_n \cong 560$ MeV $\theta_d^* \cong 44°$ as an example. This bin was chosen because its signal to background ratio is average for the 36 bins.

The first separation was begun by selecting three regions of χ^2(no copl), 0 to 6, 6 to 12, and 12 to 18, and plotting the number of events in each of these regions vs θ_{copl}. These three histograms are shown in Figure III.5. Since χ^2(no copl) has two degrees of freedom, 95% of the dγ events should have $\chi^2 < 6$ if the errors in the measured kinematic variables used in the fit were assigned properly. These events appear as a peak in the first histogram, and practically all of them have $|\theta_{copl}| < 8$ mrad in this energy-angle bin. Since θ_{copl} is independent of χ^2(no copl) for background events, the shape of the background under the peak in the first histogram should be the same as the shape of the third histogram and of the second histogram once the small peak from the dγ events with χ^2(no copl) > 6 is removed. This small peak was measured by comparing the distribution of χ^2(no copl) for all events (Figure III.3) with the same distribution for events with $|\theta_{copl}| < 4$ mrad, where the signal is much clearer. If the shapes of the third and "cleaned" second coplanarity histograms differed significantly, the second was used to predict the background. The

fractional statistical error in the number of separated dγ events was equal to the reciprocal of the square root of the total number of events in the θ_{copl} peak (dγ and background) combined in quadrature with the fractional error in the background. Since the number of background events under the peak was estimated using a roughly equal number of events outside the peak, the absolute error in the number of dγ events was approximately the square root of the sum of the number of dγ events and twice the background.

For the example bin there were 1819 events with $|\theta_{copl}| < 8$ mrad and 772 events outside this region in the first histogram. Using the third histogram to predict the background gave 1465 dγ events in the peak of the first histogram. The fraction of events with $|\theta_{copl}| < 4$ mrad which had χ^2(no copl) > 6 and were therefore in the peak of the second histogram rather than the first was found to be .07. The total number of dγ events found by using the third histogram to predict the background was thus 1465/.93 = 1575. Subtracting the 7% of these 1575 dγ events which were in the peak of the second histogram from its $|\theta_{copl}| < 8$ mrad region gave a ratio of the number of events inside that region to the number outside of 0.38. This ratio times the 772 events outside in the first histogram gives 294 background events under the peak or 1525 dγ events. The total number of dγ events found by using the second coplanarity histogram to predict the background was thus 1525/.93 = 1640. The statistical error was ± 47 events or 2.9%.

The second method of separation used on the same data was begun by plotting histograms of events from each of three regions of χ^2(no θ_γ) vs $\Delta\theta_\gamma \equiv \theta_\gamma' - \theta_\gamma$, where θ_γ' was the value of θ_γ predicted by minimizing χ^2(no θ_γ). These three histograms for the example bin are shown in Figure III.6. Note that the background under the peak in $\Delta\theta_\gamma$ of the

first histogram, as predicted from the second and third histograms, has a different shape than that under the peak in θ_{copl} used during the first separation. The second separation yielded 1588 ± 47 dγ events in the example bin.

The average of the values obtained by the two methods was 1614 ± 47 dγ events. The statistical errors of the two values could not be combined to reduce the error of their average because both methods were extracting the same set of dγ events. For the same reason, the difference in the two numbers obtained (52 dγ events for the example bin) could not be due to the statistical error in the number of dγ events. Since the backgrounds subtracted by the two methods were at least partially made up of different events, part of the difference between the two numbers obtained was due to the statistical error in the background. Most of the difference, however, was due to the error introduced in the process of separation. To make sure that one method was not systematically biased relative to the other, the difference between the number of dγ events obtained by the first method and the average of the numbers obtained by both methods was divided by the statistical error and plotted for all 36 bins. The mean of this distribution was -.0035, gratifyingly close to zero. The standard deviation of the distribution for the nine $T_n \cong 475$ MeV bins was 0.19, which was small enough to ignore. The standard deviation of the other 27 bins was 0.54, which, when combined in quadrature with the statistical error, was equivalent to multiplying the latter by 1.14.

The results of the separation are summarized in Table III.1, which shows the number of dγ events in each energy-angle bin, as determined by the average of the numbers obtained by the two methods of separation, and the combined statistical and separation error in percent.

Since protons were not clearly distinguished from deuterons in this experiment, some assurance must be given that the shape of the background due to proton events was similar to the shape of the background from $n + p \rightarrow d + \pi^\circ$. Since the first Princeton $n + p \rightarrow d + \gamma$ experiment did unambiguously separate protons from deuterons,[53] it was possible to select proton events from that data and analyze them as deuteron events. When this was done, the proton events were found to produce the same coplanarity background shape as $d\pi^\circ$ events within the statistical error, ± 5% in the worst case. Examination of the distribution of the velocity of the "deuteron" in the present experiment indicated that only about 10% of all analyzed events were from protons, so the maximum error due to proton background could not exceed ± 0.5%. This can be safely ignored when compared to the statistical error in the number of $d\gamma$ events.

Possible errors due to $d\gamma$ events or background generated in the plastic windows of the hydrogen target or other material were also small enough to be inconsequential. Possible sources of error might have been a dependence on θ_d^* of the probability for $d\gamma$ events being rejected when they originated in plastic several inches from $z = 0$, and a difference in the shape of background generated in carbon in the plastic from the shape of normal background. The $d\gamma$ event rate was measured for $T_n \cong 475$, 625, and 750 MeV at $\theta_d^* \cong 24^\circ$, 96°, and 156° with the target empty of liquid hydrogen, using the NM counter telescope to monitor the beam. No statistically significant pattern emerged because the average $d\gamma$ event rate with the target empty was only .02 ± .01 times the rate with the target full. Seventy percent of this rate would be expected from the gaseous, but still cold (about 40° K), hydrogen in the target with $|z| < 2$ inches, and 30% of it from the 2-mil thick plastic windows at

$|z| = 1$ inch (see Figure II.9). Since a 1-inch displacement in the z coordinate of the interaction point caused one standard deviation in $\Delta\theta_\gamma$, $d\gamma$ events from the 10 and 15-mil thick plastic at $|z| = 3$ and 4 inches were almost all rejected by the separation process. The shape of the background with the target empty was observed to be similar to the shape of the background with the target full. The background rate with the target empty was about 12% of the rate with the target full, consistent with production in just the hydrogen of the plastic in the target and in half of the N counter.

SECTION F CALCULATED EFFICIENCIES

This section describes the calculation, for each energy-angle bin, of the Monte Carlo acceptance, the gamma-ray conversion probability, and the fraction of deuterons lost due to interactions in the hydrogen target and other material. The Monte Carlo acceptance was the fraction of events simulated by DGMC which entered the apparatus to be detected. It was not strictly the geometrical acceptance because DGMC allowed for the loss of gamma rays by premature conversion in the material through which they passed before reaching the anti-counters in front of the converters. The gamma efficiency program calculated the probability that a gamma ray striking the converters produced a detectable particle in the G counters by simulating photon-electron showers in lead. The loss of deuterons was calculated directly from known cross sections.

DGMC used random number generators to simulate $n + p \rightarrow d + \gamma$ events near the desired average T_n as described below. The kinetic energy of the neutron for each event was selected from a Gaussian distribution with a mean at the desired $\langle T_n \rangle$ and a standard deviation of 30 MeV. Kinematic quantities of the neutron and of the np center of mass were calculated from T_n. The point of interaction was selected at random within the hydrogen target. The azimuthal angle of the gamma ray, $\varphi_\gamma = \varphi^*_\gamma$, was chosen at random between $\pi/2$ and $3\pi/2$ to avoid wasting time on gamma rays which would have gone to the wrong side of the apparatus. The center-of-mass gamma-ray angle, θ^*_γ, was selected at random between 0 and π, and the laboratory angle θ_γ and momentum P_γ were calculated. A test was performed to see if the gamma ray struck either of the lead converters for any of the nine positions of the gamma assembly. If it did, the event was placed in the appropriate bin. Some of these events

were eliminated according to the probability that the gamma ray converted in the material (target flask and housing and D chamber edges) through which it passed. All surviving gamma rays were presumed to produce detectable electron showers as far as DGMC was concerned. The deuteron center-of-mass angles were obtained from the gamma-ray angles, and the laboratory kinematic quantities of the deuteron were calculated. The laboratory deuteron angles were modified by simulated multiple scattering in material through which the deuteron passed. A test was then performed to see if the deuteron struck the D counters. If the test was passed, the event was accepted.

The Monte Carlo acceptance for a θ_d^* bin at one of the four average beam energies was defined to be the number of simulated events accepted in the bin divided by twice the total number of events simulated by DGMC for that energy. The factor of 2 was included to make up for the events with $|\varphi_\gamma| < \pi/2$ which were not simulated, though such a normalization factor is unimportant in the determination of an angular distribution. The mean value and extent of θ_d^* for each bin were read from a histogram of the number of events accepted in the bin vs θ_d^*. All bins had a fairly flat distribution of θ_d^* with an extent of $\pm$ 8° except the bin at each energy where the gamma assembly was centered in the beam, for which $\theta_d^* \cong 8° \pm 6°$. DGMC simulated 4×10^5 events at $\langle T_n \rangle$ = 475, 625, and 750 MeV, for an average of about 4500 events in each bin, and 5×10^5 events at $\langle T_n \rangle$ = 560 MeV for an average of about 5600 events in each bin. The resulting statistical errors of about 1.5% and 1.3%, though small compared to the statistical errors in the real data, were included in the determination of the errors in the points of the angular distribution.

The gamma efficiency program was a modified version of a program

written by T. Kamae using the principles developed by J. C. Butcher and H. Messel.[54] The program used Monte Carlo techniques to simulate electromagnetic showers produced in material of a given atomic number by incident photons or electrons of given initial energy. The processes of pair production, bremsstralung, Compton scattering, ionization energy loss, and multiple scattering were included. Cross sections for pair production and bremsstralung were calculated from the Bethe-Heitler formula.

To calculate the gamma-ray conversion efficiency, the program was run for 10^4 photons incident on lead at each of the following energies: 100, 150, 200, 300, 400, and 600 MeV. The development of showers was simulated in 0.1 radiation length steps. The gamma-ray conversion probability was defined to be the fraction of incident photons which produced showers containing at least one electron of energy greater than 8 MeV at a depth of 1.0 radiation length. Although the absolute probability could only be considered accurate to ± 2%, the relative probability as a function of energy was much more accurate. Because of the high statistics and small variation of from 0.438 at 100 MeV to 0.512 at 600 MeV, the relative gamma-ray conversion probability could be interpolated to within ± .002 at the mean gamma-ray energy for each of the 36 energy-angle bins of the experiment.

A small fraction of the deuterons produced in the hydrogen target interacted before reaching the D counters. It was necessary to calculate this small loss of efficiency because it was a function of the energy of the deuterons and hence of θ_d^*. Almost all of the material through which the deuterons passed was either hydrogen (0.2 g/cm^2) or carbon (0.6 g/cm^2). The cross section for deuterons interacting in either material, $\sigma(d,A)$, was calculated approximately from known nucleon-nucleon

cross sections, $\sigma(n,N)$,[55] using

$$\sigma(d,A) = 0.97\ [\sigma(p,A)+\sigma(n,A)]\ ,$$

$$\sigma(n,A) = [(A-Z)\sigma(p,p) + Z\sigma(n,p)][1 - 0.55\ A^{0.26}]\ ,\ \text{and}$$

$$\sigma(p,A) = [(A-Z)\sigma(n,p) + Z\sigma(p,p)][1 - 0.55\ A^{0.26}]\ ,[56]$$

where A was the atomic weight of the material and Z was the atomic number. These approximations are justified by the fact that the largest spread of the fraction of deuterons lost as a function of θ_d^* for a given T_n was from 2.5% to 5.3%.

Tables III.2 through III.5 summarize the results for the calculated efficiencies at each of the four neutron beam energies. For each of the nine bins of θ_d^*, each table gives the mean value of θ_d^*, the width of the bin, the mean gamma-ray energy, the gamma-ray conversion probability, the Monte Carlo acceptance, the fraction of deuterons not lost, and the over-all calculated efficiency, which was the product of the three separately calculated efficiencies. The reader may note that all of the calculated efficiencies vary smoothly over a fairly small range.

SECTION G MEASURED EFFICIENCIES AND MONITORING

Inefficiencies which could not be calculated without reference to the data were measured by noting the fraction of (predominantly $d\pi^\circ$) triggers lost from each energy-angle bin with the application of the data reduction requirements. Such measurement makes sense if the trigger efficiency was constant for each angle and if the fraction of $d\gamma$ events lost with the application of the data reduction requirements was the same as the fraction of triggers lost. The high efficiency of the counters ensured a trigger efficiency which was greater than 99% and did not change with θ_d^* by more than 0.5%. At very low beam intensities, where no spurious triggers caused by uncorrelated particles or events containing extra particles should have occurred, the efficiency for reconstructed $d\gamma$ events should have been the same as the efficiency for all triggers. Since most triggers occurred at high intensity, however, a detailed study of efficiency as a function of intensity was necessary. This study used as a reference the number of proton monitor counts (PM/8) as a function of beam intensity, so that efficiency measurements and beam monitoring were intimately connected.

The off-line version of Hist made histograms of the number of proton monitor counts and of event triggers meeting certain requirements vs beam intensity in bins of 4 SIM ADC units. The proton monitor histogram used only PM/8 counts with the appropriate TOF of the recoil proton for the elastic peak. Let M_i be the number of such counts in the ith intensity bin and M be the total number of these "elastic" proton monitor counts. A histogram of proton monitor counts vs TOF for $T_n \cong 560$ MeV is shown in Figure III.7. The histogram of the number of these counts with a TOF between 27.5 and 37.5 nsec vs intensity is

shown in Figure III.8.

Hist made three histograms of the number of event triggers vs intensity. The first of these was for all triggers. Let $T1_i$ be the number of triggers in the ith intensity bin of the first histogram. The third histogram was for triggers which passed all data reduction requirements necessary for analysis as a possible $d\gamma$ event: passing Scheck, Trkfit, Gamfit, Timing, and the cuts on the velocities of the neutron, deuteron, and gamma ray. Let the value in the ith bin of the third histogram be $T3_i$ and the total be T3. Each of the first five of the seven data reduction requirements may have removed some $d\gamma$ events. The second histogram was for triggers which passed at least these first five requirements. Let $T2_i$ be the values in each bin of this histogram.

The subroutine Finish calculated the ratios $R1_i \equiv T1_i/M_i$, $R2_i$, $R3_i$ and their logarithms $\ln R1_i$, $\ln R2_i$, $\ln R3_i$ for each of the first 25 intensity bins. Finish then performed a least squares fit of a straight line to the first 12 points of each of the three sets of logarithms of the ratios. These straight lines on a logarithmic scale represent the exponential probability of detecting one and only one particle in a fixed time as a function of intensity. The average over all 36 energy--angle bins of χ^2 for the straight line fits to $\ln R3_i$ was 10.1 for 10 degrees of freedom. Figure III.9 shows $R3_i$ with statistical errors plotted on a logarithmic scale vs intensity and the lines fitted by Finish for five θ_d^* bins at $T_n \cong 560$ MeV.

The total measured efficiency was

$$(R2_o/R1_o) \cdot T3/(M \cdot R3_o) \quad , \tag{3.5}$$

where $R1_o$, $R2_o$, and $R3_o$ were the antilogarithms of the values at zero intensity of the lines fitted by Finish to $\ln R1_i$, $\ln R2_i$, and $\ln R3_i$.

$R2_o/R1_o$ was the intensity-independent efficiency extrapolated to zero intensity where it was unspoiled by extra particles and spurious triggers. $T3/(M \cdot R3_o)$ was the intensity-dependent efficiency for what were essentially $d\pi^\circ$ triggers. To check if this expression was valid for $d\gamma$ events, the number of separated $d\gamma$ events in each intensity bin divided by $T3_i$ was plotted as a function of intensity. To gain meaningful statistics, the numbers for all nine θ_d^* bins at $T_n \cong 560$ MeV were combined to obtain the graph shown in Figure III.10. This set of points fits a horizontal line with a χ^2 of 21 for 23 degrees of freedom, indicating that the loss of efficiency with intensity was the same for $d\gamma$ and $d\pi^\circ$ events.

Each factor in expression (3.5) for the measured efficiency had a statistical error, but each factor was computed using a subset of the same data, so the errors were not combined. $R3_o$ was computed using the smallest subset of data, so its percent error, computed by Finish, was taken to be the percent error in the reciprocal of the measured efficiency. This error was added in quadrature to the statistical and separation error in the number of $d\gamma$ events and the error in the Monte Carlo acceptance for each energy-angle bin to obtain the error in each point of the angular distribution.

Tables III.6 through III.9 give the measured intensity-independent and intensity-dependent efficiencies, their product (the total measured efficiency), the percent error in the reciprocal of the total measured efficiency, and the number of elastic proton monitor counts for each θ_d^* bin at each of the four neutron energies.

CHAPTER IV

RESULTS AND COMPARISONS

SECTION A THE ANGULAR DISTRIBUTION OF $n + p \rightarrow d + \gamma$

The unnormalized center-of-mass differential cross section of $n + p \rightarrow d + \gamma$ at $T_n \cong 475$, 560, 625, and 750 MeV for nine values of θ_d^* at each energy was calculated from the relation

$$\frac{d\sigma}{d\Omega}(\theta_d^*) \propto N(d\gamma) \,/\, (E_{calc} \cdot E_{meas} \cdot M) \quad ,$$

where, for each energy-angle bin, $N(d\gamma)$ was the number of events, E_{calc} and E_{meas} were the over-all calculated and measured efficiencies, and M was the number of elastic proton monitor counts.

A sum of Legendre polynomials was fit to these angular distributions:

$$\frac{d\sigma}{d\Omega}(\text{unnormalized}) = a_o + a_1 P_1(\cos\theta_d^*) + a_2 P_2(\cos\theta_d^*) + \cdots \quad .$$

It was found that the goodness of fit was not significantly improved by adding terms of higher order than P_2. The angular distributions were normalized to a total cross section of 4π by dividing each point by a_o. The fit to the normalized angular distributions is then

$$\frac{d\sigma}{d\Omega}(\text{normalized}) \cong 1 + A_1 P_1(\cos\theta_d^*) + A_2 P_2(\cos\theta_d^*) \quad ,$$

where $A_1 = a_1/a_o$ and $A_2 = a_2/a_o$.

Tables IV.1 through IV.4 show the unnormalized angular distributions of $n + p \rightarrow d + \gamma$ at $T_n = 475$, 560, 625, and 750 MeV with percent errors and the normalized angular distribution with absolute errors. The errors include the statistical and separation errors in the number of $d\gamma$ events, the statistical error in the Monte Carlo acceptance calculation, and the statistical error in the measured efficiency. Graphs of the normalized angular distributions and their second-order Legendre polynomial fits are shown in Figures IV.1 through IV.4. The

coefficients A_1 and A_2 and the χ^2 per degree of freedom of the fits are given in Table IV.5.

SECTION B COMPARISON OF THE ANGULAR DISTRIBUTIONS OF $n + p \rightleftarrows d + \gamma$

In order to compare the angular distribution of $n + p \rightarrow d + \gamma$ measured by this experiment with the angular distribution of its inverse process, $\gamma + d \rightarrow n + p$, previously measured by other experiments, two requirements must be met. The comparison must be made at the same center-of-mass energy, and the various "inverse" experiments must be suitably averaged. The condition of equal center-of-mass energies expressed in terms of the incident particle laboratory energies is $T_n = 2E_\gamma$ (equation (1.3)). Although this condition cannot be met exactly, the inverse experiments have been performed at a variety of energies and can be chosen so that a number of them will have approximately the right average energy.

The angular distributions of $n + p \rightarrow d + \gamma$ measured by this experiment at T_n = 475, 560, 625, and 750 MeV are plotted in Figure IV.5 along with the angular distributions at nearly equivalent energies reported by the four most recent and accurate deuteron photodisintegration measurements: Anderson et al.,[10] Buon et al.,[12] Sober et al.,[21] and Kose et al.[18] Two facts are apparent from visual inspection of the figure. One is that the angular distributions of the two reactions are at least roughly the same. The other is that Kose et al. do not agree with the other three measurements, so their data has not been used for numerical comparisons.

The process of averaging the inverse experiments was begun by fitting a sum of Legendre polynomials to the angular distribution measured at each energy by each experiment. This allowed all measurements to be normalized to the same total cross section. The

measurements by Buon et al. and Sober et al. were fit to within their errors by a second-order series; the greater accuracy of the measurements by Anderson et al. required a fourth-order series. A fifth order fit was then made to all the inverse data measured at E_γ near $T_n/2$ for each of our four values of T_n. The χ^2 per degree of freedom of these four over-all fits varied from 0.7 to 3.5. The discrepancies between the data sets were mostly due to the different energies at which the measurements were made. Multiplying the quoted errors of each of the experiments by 1.75 decreased the χ^2 of the over-all fits to statistically likely values. The parameters of the over-all fits are summarized in Table IV.6, which gives the energies of the experiments used, the χ^2 using quoted errors and 1.75 times quoted errors, and the coefficients, A_1 and A_2.

Comparison of the angular distributions of the two processes has been made in two ways. The first is to compute the χ^2 of a least--squares fit between the data points of this experiment and the over-all fits to the inverse experiments. This method is fairly model--independent in that it shows whether there is any statistically significant difference between the angular distributions of the two processes. The second method is to compare the coefficients of the Legendre polynomials in the fits to both reactions and to determine the TRI violating phase, Δ, in Barshay's model. The expression for Δ is given by equation (1.11).

The χ^2 method of comparison requires the assignment of an error to the over-all fit of the inverse data. Since the root-mean-square error of the points in the over-all fits using 1.75 times the quoted errors averaged about 3% for the four fits, a 3% error band was used. The relative normalization was allowed to vary to minimize χ^2. At $T_n = 475$,

560, 625, and 750 MeV, the χ^2 for 8 degrees of freedom, and the normalization are given in Table IV.7.

The determination of Δ in Barshay's model involves comparison of the angular distributions measured at the energy of the resonance peak. Because of the large width of the resonance (see Figure I.2), it is reasonable to consider the measurements at $T_n \cong 560$ and 625 MeV as both being on the resonance. The weighted average of the A_2 coefficients for these two measurements of the angular distribution is $A_2(np \rightarrow d\gamma) = -.175 \pm .023$. The weighted average of the inverse data gives $A_2(\gamma d \rightarrow np) = -.167 \pm .007$. Using these values, equation (1.11) yields $\Delta = 1.4° \pm 4.1°$.

CHAPTER V

CONCLUSION

This experiment has found no evidence for any violation of time-reversal invariance (TRI) in $n + p \rightleftarrows d + \gamma$. The angular distributions of the two processes agree within the errors, which are roughly 5% at each point. The value found by this experiment of the TRI violating phase in Barshay's model, $\Delta = 1.4° \pm 4.1°$, sets an upper limit on the magnitude of this quantity $|\Delta| < 5.5°$ with 68% confidence. As pointed out in section I.B concerning reciprocity tests which do not detect spin, such a test as this one cannot exclude the possibility of a violation of TRI which depends on spin.

REFERENCES

REFERENCES

1. D. Bartlett, C. Friedberg, P. Goldhagen, and K. Goulianos, Phys. Rev. Letters 27, 881 (1971).
2. T. D. Lee and C. N. Yang, Phys. Rev. 104, 254 (1956).
3. C. S. Wu, E. Ambler, R. Hayward, D. Hoppes, and R. Hudson, Phys. Rev. 105, 1413 (1957).
4. R. Garwin, L. Lederman, M. Weinrich, Phys. Rev. 105, 1415 (1957); J. Friedman and V. Telegdi, ibid. 105, 1681 (1957).
5. J. Christenson, J. Cronin, V. Fitch, and R. Turlay, Phys. Rev. Letters 13, 138 (1964).
6. R. Streater and A. Wightman, PCT, Spin and Statistics, and All That, Benjamin (New York, 1964), p. 142.
7. R. C. Casella, Phys. Rev. Letters 21, 1128 (1968).
8. Iu. A. Aleksandrov, N. B. Delone, L. I. Shovokhotov, and G. A. Sekol, JEPT 33, 614 (1957); translated in JEPT (Soviet Physics) 6, 473 (1958).
9. Lew Allen, Jr., Phys. Rev. 98, 705 (1955).
10. R. L. Anderson, R. Prepost, and B. H. Wiik, Phys. Rev. Letters 22, 651 (1969).
11. T. S. Benedict and W. M. Woodward, Phys. Rev. (letter) 85, 924 (1952).
12. J. Buon, V. Gracco, J. LeFrancois, P. Lehmann, B. Merkel, and Ph. Roy, Phys. Letters 26B, 595 (1968); B. Merkel, thesis.
13. D. R. Dixon and K. C. Bandtel, Phys. Rev. 104, 1730 (1956); D. R. Dixon, thesis, Univ. of Cal. Rad. Lab. UCRL-2956 (unpublished).
14. J. A. Galey, Phys. Rev. 117, 163 (1960).
15. W. S. Gilbert and J. W. Rosengren, Phys. Rev. 88, 901 (1952).

16. J. C. Keck and A. V. Tollestrup, Phys. Rev. 101, 360 (1956).

17. J. Keck, R. M. Littauer, G. K. O'Neill, A. M. Perry, and W. M. Woodward, Phys. Rev. 93, 827 (1954).

18. R. Kose, W. Paul, K. Stockhorst, and K. H. Kissler, Z. Phys. 202, 364 (1967); R. Kose, thesis, Universität Bonn, unpublished.

19. R. Littauer and J. C. Keck, Phys. Rev. (letter) 86, 1051 (1952).

20. A. M. Smith, S. J. Hall, B. Mann, and D. T. Stuart, J. Phys. A (Proc. Phys. Soc.) Series 2, Vol 1, 553 (1968).

21. D. I. Sober, D. G. Cassel, A. J. Sadoff, K. W. Chen, and P. Crean, Phys. Rev. Letters 22, 430 (1969); D. I. Sober, thesis, Cornell University, 1969, PPA report (unpublished).

22. E. A. Whalin, B. D. Schriever, and A. O. Hanson, Phys. Rev. 101, 377 (1956).

23. E. A. Whalin, Phys. Rev. 95, 1362 (1954).

24. T. Yamagata, M. Q. Barton, A. O. Hanson, and J. H. Smith, Phys. Rev. 95, 574 (1955).

25. For a review of the literature through 1966, see M. E. Toms, U. S. Naval Research Lab. Bibl. 31 (1967).

26. D. Bartlett, C. Friedberg, K. Goulianos, I. Hammerman, and D. P. Hutchinson, Phys. Rev. Letters 23, 893 (1969).

27. C. Friedberg, thesis, Princeton University, 1969, Joseph Henry Laboratories Report No. PURC-2137-13 (unpublished).

28. B. Schrock, J. Detoeuf, R. Haddock, J. Helland, M. Longo, K. Young, S. Wilson, D. Cheng, J. Sperinde, and V. Perez-Mendez, in High Energy Physics and Nuclear Structure, edited by S. Devons (Plenum, New York, 1970), pp. 727-738.

29. B. Schrock, R. Haddock, J. Helland, M. Longo, S. Wilson, K. Young, D. Cheng, and V. Perez-Mendez, Phys. Rev. Letters 26, 1659 (1971).

30. E. Wigner, Nachrichten von der Gesellschaft der Wissenschaften zu Gottingen, 546 (1932); translated in Group Theory and its Application to the Quantum Theory of Atomic Spectra (translated by J. Griffin), Academic Press (New York, 1959), chapter 26.

31. J. Bernstein, G. Feinberg, and T. D. Lee, Phys. Rev. 139, B1650 (1965).

32. A. Bohr and B. Mottelson, Nuclear Structure vol. 1, Benjamin (New York, 1969), appendix 1B.

33. J. Blatt and V. Weisskopf, Theoretical Nuclear Physics, Wiley (New York, 1952) chapter 10.

34. W. S. C. Williams, An Introduction to Elementary Particles, 2nd Ed., Academic Press (New York, 1971), chapter 6.

35. J. J. Sakurai, Invariance Principles and Elementary Particles, Princeton University Press (Princeton, 1964), chapter 4.

36. G. C. Wick, Ann. Rev. Nucl. Sci. 8, 1 (1958).

37. G. Feinberg, Phys. Rev. 140, B1402 (1965).

38. J. Baird, P. Miller, W. Dress, and N. Ramsey, Phys. Rev. 179, 1285 (1969); J. Baird, thesis, Harvard University, 1969 ORNL-TM-2308 (unpublished).

39. P. Berardo, R. Haddock, B. Nefkins, L. Verhey, M. Zeller, A. Parsons, and P. Truoel, Phys. Rev. Letters 26, 201 (1971); P. Berardo, R. Haddock, J. Helland, B. Nefkins, L. Verhey, M. Zeller, A. Parsons, and P. Truoel, Phys. Rev. Letters 26, 205 (1971).

40. N. Christ and T. D. Lee, Phys. Rev. 148, 1520 (1966).

41. J. Chen, J. Sanderson, J. Appel, G. Gladding, M. Goitein, K. Hanson, D. Imrie, T. Kirk, R. Madras, R. Pound, L. Price, R. Wilson, and C. Zajde, Phys. Rev. Letters 21, 1279 (1968); J. Chen, thesis, Harvard University, 1969 (unpublished).

42. S. Rock, M. Borghini, O. Chamberlain, R. Fuzesy, C. Morehouse, T. Powell, G. Shapiro, H. Weisberg, R. Cottrell, J. Litt, L. Mo, and R. Taylor, Phys. Rev. Letters 24, 748 (1970).

43. M. Bazin, A. Goshaw, R. Zacher, H. Blumenfeld, T. Kitagaki, and C. Sun, Phys. Rev. Letters 19, 1157 (1967); 20, 895 (1968).

44. M. Gormley, E. Hyman, W. Lee, T. Nash, J. Peoples, C. Schutz, and S. Stein, Phys. Rev. Letters 22, 108 (1969); 21, 402 (1968).

45. J. Layter, J. Appel, A. Kotlewski, W. Lee, S. Stein, and J. Thaler, Phys. Rev. Letters (to be published); J. Thaler, private communication.

46. M. Gormley et al., ibid, 21, 399 (1968).

47. J. Thaler, J. Appel, A. Kotlewski, J. Layter, W. Lee, and S. Stein, Phys. Rev. Letters (to be published); J. Thaler, private communication.

48. S. Barshay, Phys. Rev. Letters 17, 49 (1966).

49. C. Friedberg, ibid, pp. 9-11.

50. C. Friedberg, ibid., p. 103.

51. P. Shepard, thesis, Princeton University, 1969 (unpublished); with T. Devlin, R. Mishke, J. Solomon, PPA report PPAR 10, 1969 (unpublished).

52. T. Droege, J. McFadden, D. Rehberger, R. VonColln, S. Wash, PPA technical notes PPAD ED-93, PPAD 605 E, PPAD 671 E (unpublished).

53. D. Bartlett, C. Friedberg, K. Goulianos, I. Hammerman, and D. P. Hutchinson, Phys. Rev. D 1, 1987 (1970).

54. J. Butcher and H. Messel, Nucl. Phys. 20, 15 (1960).

55. O. Benary, L. Price, and G. Alexander, UCRL-20000 NN (August 1970).

56. S. Wilson, thesis, University of Michigan, 1971, p. 40 (unpublished).

TABLES

Table II.1. Contributions to Neutron Spectrum Width

	ΔT_n in MeV due to:					
$\langle T_n \rangle$	Momentum inside deuteron	.7 × dE/dx in ½ Be tgt	Spill width	Timing error	$(\Sigma\sigma_i^2)^{\frac{1}{2}}$	Measured σ
475	29.6	8.5	3.0	6.8	31.6	31.0
560	33.2	8.1	8.7	9.6	36.5	35.2
625	35.1	8.0	7.8	11.4	38.5	38.5
750	40.3	7.8	7.0	21.6	46.9	48.5

Table II.2. Description of Counters

Counter	Scintillant dimensions (inches)			Scintillant type	Tube mounted	Voltage	Efficiency for min. ioniz. part.
	Horizontal	Vertical	Thickness				
D1, D2, D3, D4	48	36	.50	NE 110	Horiz.	2250	> .995
GA1, GA2, G1, G3	24	16	.25	NE 110	Horiz.	2000	> .999
G2, G4	"	"	"	"	"	2150	> .999
N, AB	10	8	.050	Pilot B	Vert.	2150	.995
PM1	14	14	.25	NE 102	Vert.	2000	> .997
PM2	18	18	.25	Pilot A	Vert. (2)	2000	> .997
NMA	2	2	.063	Pilot B	Horiz.	1900	> .99
NM1	1	1	.063	Pilot B	Horiz.	1700	> .99
NM2	"	"	"	"	"	1800	> .99
SIM	2-in. diam. x 4-in. long lucite Č radiator				Slant	~ 1750	——

Table III.1. Number of dγ Events in Each θ_d^* Bin

Mean θ_d^* of bin (degrees)	Number of dγ events in θ_d^* bin and percent error for $\langle T_n \rangle$ of:			
	475 MeV	560 MeV	625 MeV	750 MeV
8	642 ± 4.7	1547 ± 4.2	724 ± 7.4	978 ± 5.8
24	712 4.2	1736 3.6	727 7.6	913 6.6
43	643 4.1	1614 3.3	826 6.2	768 7.1
61	443 5.0	997 3.8	835 4.5	688 7.0
79	460 4.8	986 3.7	873 3.9	840 4.5
96	447 4.9	1380 3.2	924 3.8	735 4.5
115	402 5.5	966 3.7	717 4.4	883 3.9
135	376 5.3	1180 3.4	938 4.0	863 4.2
156	348 5.8	1332 3.7	767 5.4	845 7.0
Total	4464	11738	7331	7513

31046

Table III.2. Calculated Efficiencies for $T_n \cong 475$ MeV

Mean θ_d^* and extent of bin (degrees)	Mean γ-ray energy (MeV)	Calculated efficiencies			
		γ-Ray conversion probability	Monte Carlo acceptance	Fraction of deuterons not lost	Over-all (= product)
9 ± 6	135	.460	.00749	.975	.00336
25 ± 8	140	.463	.00682	.975	.00308
46 ± 8	160	.470	.00589	.974	.00270
64 ± 8	185	.477	.00520	.973	.00241
81 ± 8	215	.483	.00498	.970	.00233
99 ± 8	250	.490	.00503	.966	.00238
118 ± 8	285	.493	.00531	.961	.00252
137 ± 8	315	.497	.00555	.953	.00263
158 ± 8	330	.498	.00566	.947	.00267

Table III.3. Calculated Efficiencies for $T_n \cong 560$ MeV

Mean θ_d^* and extent of bin (degrees)	Mean γ-ray energy (Mev)	Calculated efficiencies			
		γ-Ray conversion probability	Monte Carlo acceptance	Fraction of deuterons not lost	Over-all (= product)
9 ± 6	147	.465	.00692	.975	.00314
24 ± 8	155	.468	.00635	.975	.00290
44 ± 8	180	.475	.00565	.975	.00262
62 ± 8	215	.483	.00518	.975	.00244
79 ± 8	260	.491	.00508	.973	.00243
97 ± 8	295	.495	.00506	.971	.00243
116 ± 8	340	.499	.00550	.965	.00265
136 ± 8	375	.500	.00588	.960	.00282
157 ± 8	405	.502	.00603	.954	.00289

Table III.4. Calculated Efficiencies for $T_n \cong 625$ MeV

Mean θ_d^* and extent of bin (degrees)	Mean γ-ray energy (MeV)	Calculated efficiencies			
		γ-Ray conversion probability	Monte Carlo acceptance	Fraction of deuterons not lost	Over-all (= product)
8 ± 6	155	.468	.00656	.977	.00300
24 ± 8	165	.471	.00606	.977	.00279
43 ± 8	195	.478	.00542	.977	.00253
61 ± 8	235	.487	.00499	.977	.00237
78 ± 8	280	.493	.00492	.975	.00236
95 ± 8	325	.498	.00513	.973	.00249
114 ± 8	370	.500	.00578	.970	.00280
135 ± 8	420	.502	.00599	.960	.00289
156 ± 8	450	.503	.00651	.955	.00313

Table III.5. Calculated Efficiencies for $T_n \cong 750$ MeV

Mean θ_d^* and extent of bin (degrees)	Mean γ-ray energy (MeV)	Calculated efficiencies			
		γ-Ray conversion probability	Monte Carlo acceptance	Fraction of deuterons not lost	Over-all (= product)
8 ± 6	175	.474	.00612	.978	.00284
23 ± 8	185	.477	.00542	.978	.00253
41 ± 8	220	.484	.00519	.978	.00246
58 ± 8	265	.492	.00483	.978	.00232
75 ± 8	320	.497	.00477	.978	.00232
93 ± 8	380	.500	.00527	.974	.00257
112 ± 8	440	.503	.00593	.973	.00290
133 ± 8	510	.506	.00654	.970	.00321
155 ± 8	555	.507	.00725	.962	.00354

Table III.6. Measured Efficiencies and Monitoring for $T_n \cong 475$ MeV

Mean θ_d^* of bin (degrees)	Measured efficiencies				Elastic proton monitor counts
	Intensity independent	Intensity dependent	Total	Percent error in 1/total	
9	.906	.871	.789	2.8	70998
25	.918	.900	.826	2.5	70403
46	.910	.945	.856	3.8	57106
64	.909	.910	.827	5.7	44911
82	.880	.866	.762	4.2	50862
99	.839	.899	.755	6.9	52969
118	.873	.963	.841	6.0	49697
138	.890	.849	.756	3.2	53310
158	.886	.944	.836	2.5	54323

Table III.7. Measured Efficiencies and Monitoring for $T_n \cong 560$ MeV

Mean θ_d^* of bin (degrees)	Measured efficiencies				Elastic proton monitor counts
	Intensity independent	Intensity dependent	Total	Percent error in 1/total	
9	.910	.780	.710	1.4	121619
24	.918	.856	.785	1.5	123711
44	.918	.916	.841	1.7	121338
62	.928	.855	.794	2.9	77280
80	.909	.914	.831	3.3	77120
97	.908	.865	.786	2.9	107122
116	.910	.806	.733	3.0	76531
136	.928	.818	.759	2.0	104758
157	.925	.796	.736	1.4	130082

Table III.8. Measured Efficiencies and Monitoring for $T_n \cong 625$ MeV

Mean θ_d^* of bin (degrees)	Measured efficiencies				Elastic proton monitor counts
	Intensity independent	Intensity dependent	Total	Percent error in 1/total	
8	.895	.710	.635	1.8	66353
24	.940	.776	.729	2.2	55097
43	.922	.802	.739	2.3	66826
61	.928	.869	.806	2.4	61000
78	.914	.926	.846	3.6	59903
96	.922	.842	.776	3.2	66934
115	.950	.787	.748	3.0	57522
135	.926	.883	.818	1.6	69795
156	.819	.886	.725	1.8	68770

Table III.9. Measured Efficiencies and Monitoring for $T_n \cong 750$ MeV

Mean θ_d^* of bin (degrees)	Measured efficiencies				Elastic proton monitor counts
	Intensity independent	Intensity dependent	Total	Percent error in 1/total	
8	.906	.626	.567	1.4	117340
23	.920	.641	.589	1.7	108650
42	.917	.721	.661	2.1	84905
59	.917	.756	.693	2.6	81992
76	.903	.776	.701	2.5	88868
93	.924	.759	.701	2.9	77024
112	.911	.794	.724	2.1	84837
133	.903	.790	.714	1.6	93897
155	.867	.699	.606	1.5	106354

Table IV.1. Angular Distribution of $n + p \rightarrow d + \gamma$ at $T_n = 475$ MeV

θ_d^* (degrees)	Angular distribution			
	Unnormalized	Percent error	Normalized†	Absolute error
9	3.41	± 5.7	0.783	± .045
25	4.16	5.1	0.956	.049
46	4.87	5.7	1.119	.063
64	4.95	8.0	1.136	.090
81	5.09	6.6	1.170	.077
99	4.70	8.0	1.078	.095
118	3.82	8.3	0.877	.073
137	3.55	6.4	0.815	.052
158	2.87	6.4	0.659	.042

† The angular distribution was normalized by fitting with $A_0 + A_1P_1(\cos\theta) + A_2P_2(\cos\theta)$ and setting $A_0 = 1$.

Table IV.2. Angular Distribution of $n + p \rightarrow d + \gamma$ at $T_n = 560$ MeV

θ_d^* (degrees)	Angular distribution			
	Unnormalized	Percent error	Normalized†	Absolute error
9	5.71	± 4.7	0.932	± .044
24	6.16	4.2	1.007	.042
44	6.04	4.0	0.986	.039
62	6.66	4.9	1.087	.054
79	6.33	5.2	1.034	.053
97	6.75	4.6	1.102	.050
116	6.50	4.9	1.061	.052
136	5.26	4.1	0.860	.035
157	4.81	4.1	0.786	.033

† The angular distribution was normalized by fitting with $A_0 + A_1P_1(\cos\theta) + A_2P_2(\cos\theta)$ and setting $A_0 = 1$.

Table IV.3. Angular Distribution of $n + p \rightarrow d + \gamma$ at T_n = 625 MeV

θ_d^* (degrees)	Angular distribution			
	Unnormalized	Percent error	Normalized†	Absolute error
8	5.73	± 7.8	0.887	± .069
24	6.49	8.1	1.005	.081
43	6.61	6.8	1.024	.070
61	7.17	5.3	1.110	.059
78	7.30	5.6	1.130	.063
96	7.14	5.2	1.106	.058
115	5.95	5.6	0.922	.052
135	5.69	4.6	0.880	.040
156	4.92	5.8	0.761	.044

† The angular distribution was normalized by fitting with $A_0 + A_1P_1(\cos\theta) + A_2P_2(\cos\theta)$ and setting $A_0 = 1$.

Table IV.4. Angular Distribution of $n + p \rightarrow d + \gamma$ at T_n = 750 MeV

θ_d^* (degrees)	Angular distribution			
	Unnormalized	Percent error	Normalized†	Absolute error
8	5.18	± 6.3	1.032	± .065
23	5.64	6.7	1.124	.075
41	5.56	7.9	1.109	.087
58	5.22	7.6	1.040	.079
75	5.81	5.4	1.158	.062
93	5.30	5.6	1.056	.059
112	4.96	4.7	0.988	.046
133	4.01	4.7	0.799	.038
155	3.70	7.3	0.738	.054

† The angular distribution was normalized by fitting with $A_0 + A_1P_1(\cos\theta) + A_2P_2(\cos\theta)$ and setting $A_0 = 1$.

Table IV.5. Parameters of Second Order Legendre Polynomial Fits[†] to the Measured Angular Distributions of $n + p \rightarrow d + \gamma$

T_n (MeV)	A_1	A_2	χ^2/degree of freedom
475	.14 ± .025	-.30 ± .04	7.9/6
560	.10 ± .02	-.17 ± .03	6.0/6
625	.12 ± .03	-.19 ± .04	3.5/6
750	.21 ± .03	-.15 ± .04	3.6/6

[†] The fits are of the form $A_0 + A_1P_1(\cos\theta) + A_2P_2(\cos\theta)$, where $A_0 = 1$.

Table IV.6. Summary of Fits to All $\gamma + d \rightarrow n + p$ Angular Distributions Listed in Each Energy Region

T_n (MeV)	E_γ in MeV used in measurements by:			χ^2/degree of freedom		Coefficients using 1.75 × quoted errors	
	Anderson et al.	Buon et al.	Sober et al.	Using quoted errors	Using 1.75 × quoted errors	A_1	A_2
475	222,254	220	240	115/33	38/33	.167 ± .005	-.185 ± .007
560	254,302	280	280	90/34	29/34	.153 ± .005	-.170 ± .007
625	302	320	320	15/22	5/22	.145 ± .009	-.163 ± .011
750	342	360	—	33/15	11/15	.122 ± .011	-.153 ± .013

Table IV.7. Fit of $n + p \rightarrow d + \gamma$ Data to Over-All $\gamma + d \rightarrow n + p$ Fits

T_n	χ^2/degree of freedom	Relative normalization
475	8.3/8	0.962
560	10.1/8	0.999
625	5.8/8	0.998
750	6.2/8	0.996

FIGURES

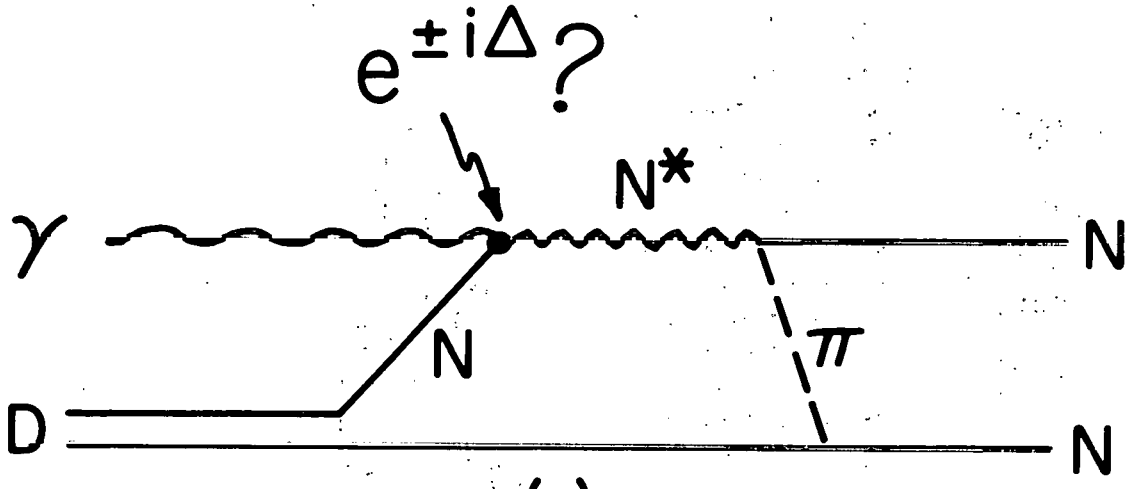

(a)

Resonant

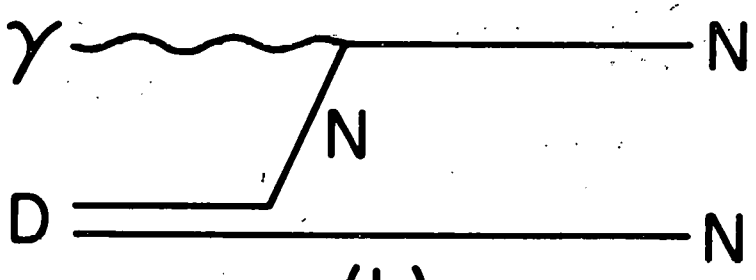

(b)

Background

FIGURE I.1

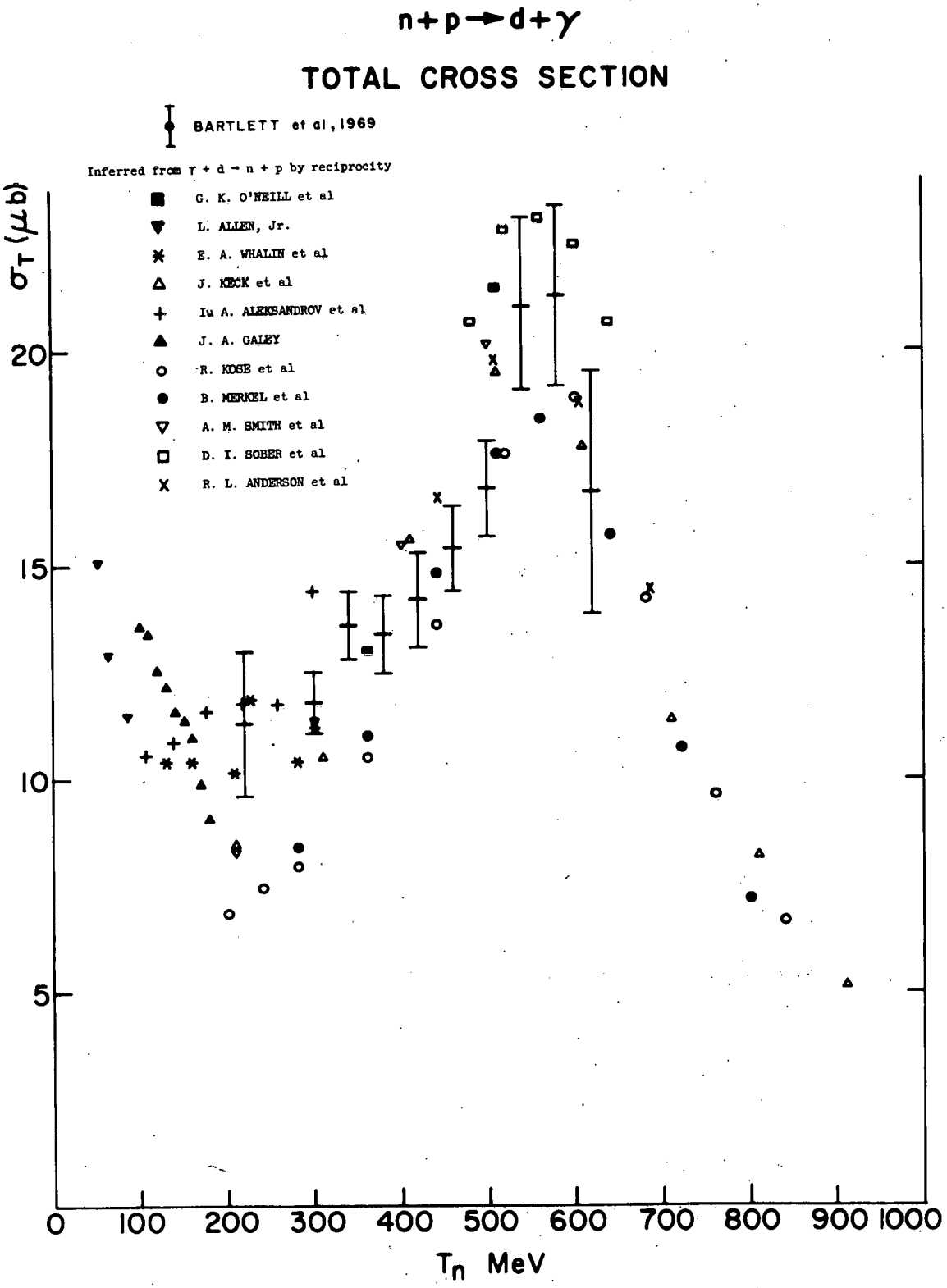
n+p→d+γ
TOTAL CROSS SECTION
BARTLETT et al, 1969
Inferred from γ + d → n + p by reciprocity
G. K. O'NEILL et al
L. ALLEN, Jr.
E. A. WHALIN et al
J. KECK et al
Iu A. ALEKSANDROV et al
J. A. GALEY
R. KOSE et al
B. MERKEL et al
A. M. SMITH et al
D. I. SOBER et al
R. L. ANDERSON et al
σT (μb)
20
15
10
5
0
100
200
300
400
500
600
700
800
900
1000
Tn MeV

FIGURE I.2

KINEMATIC ELLIPSE

$n+p \rightarrow d+\gamma^{\circ}$

$n+p \rightarrow d+\pi$

$T_n = 600$ MeV

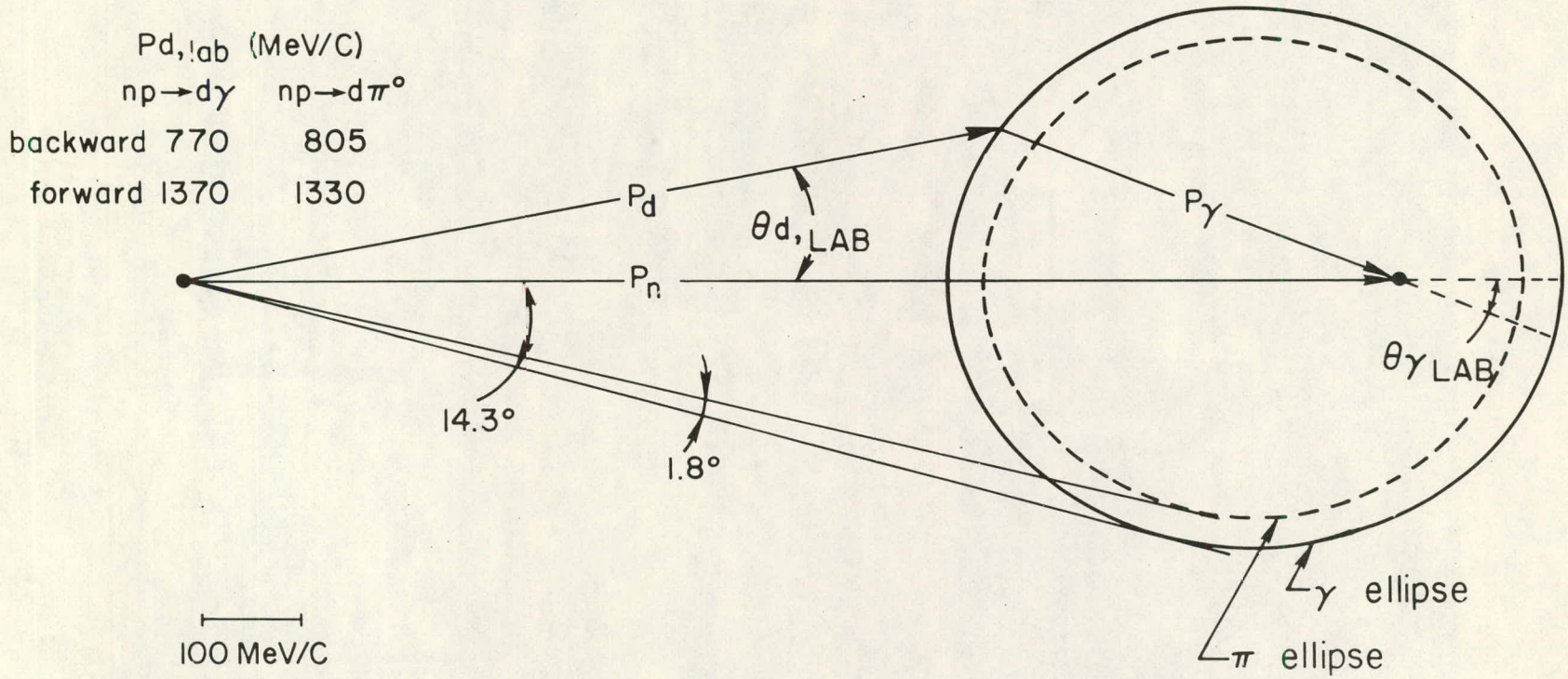

FIGURE II.4

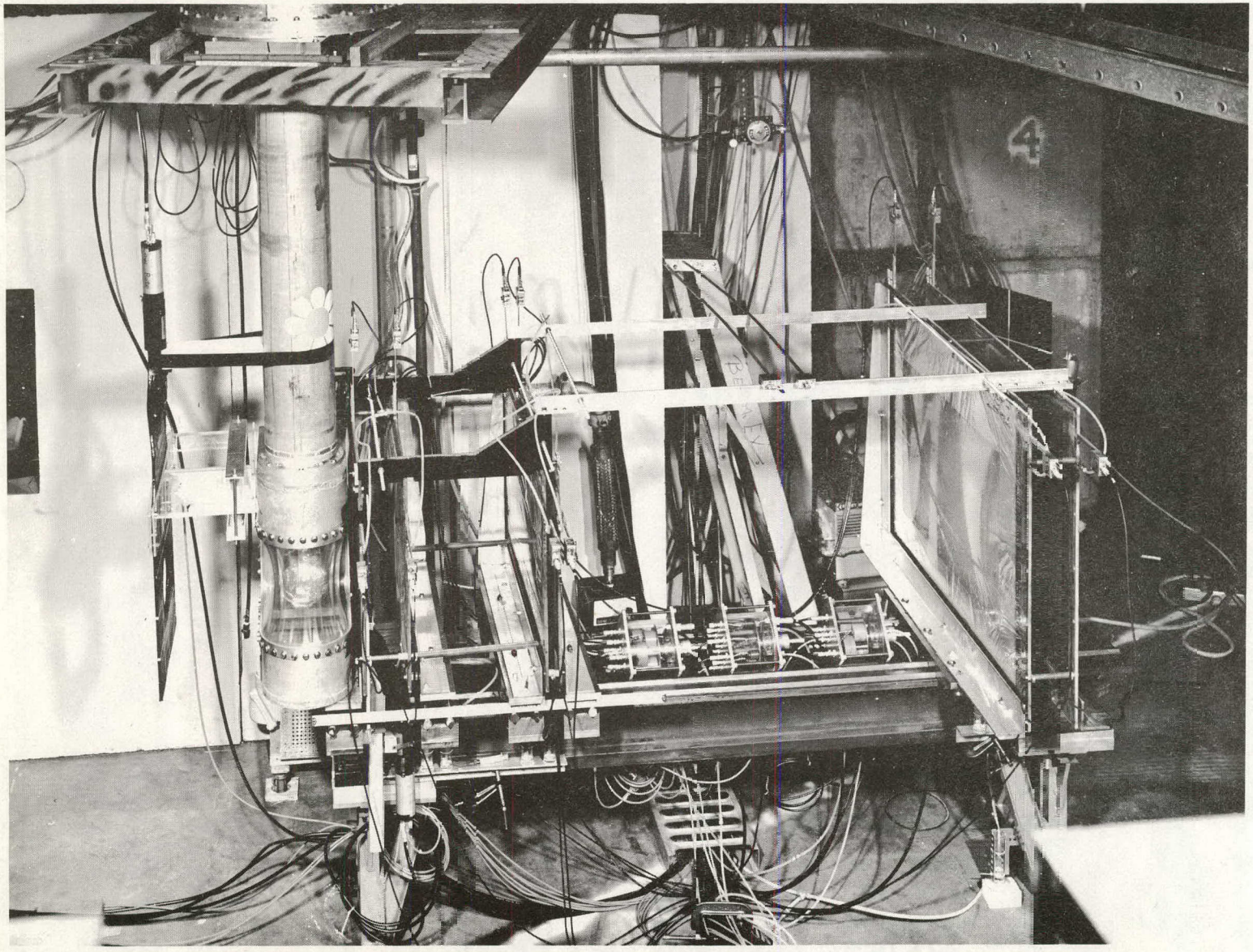

FIGURE II.3

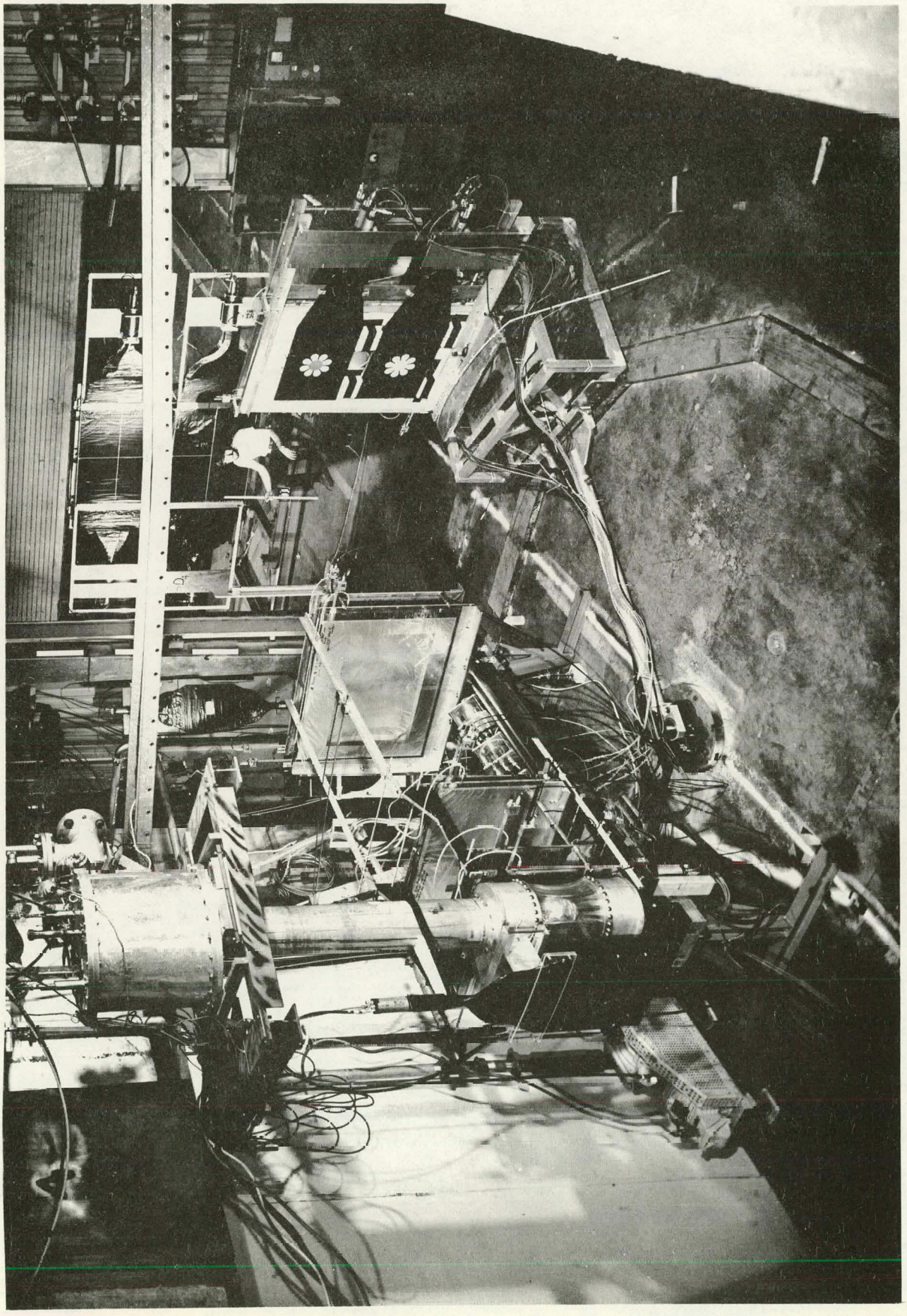

FIGURE II.2

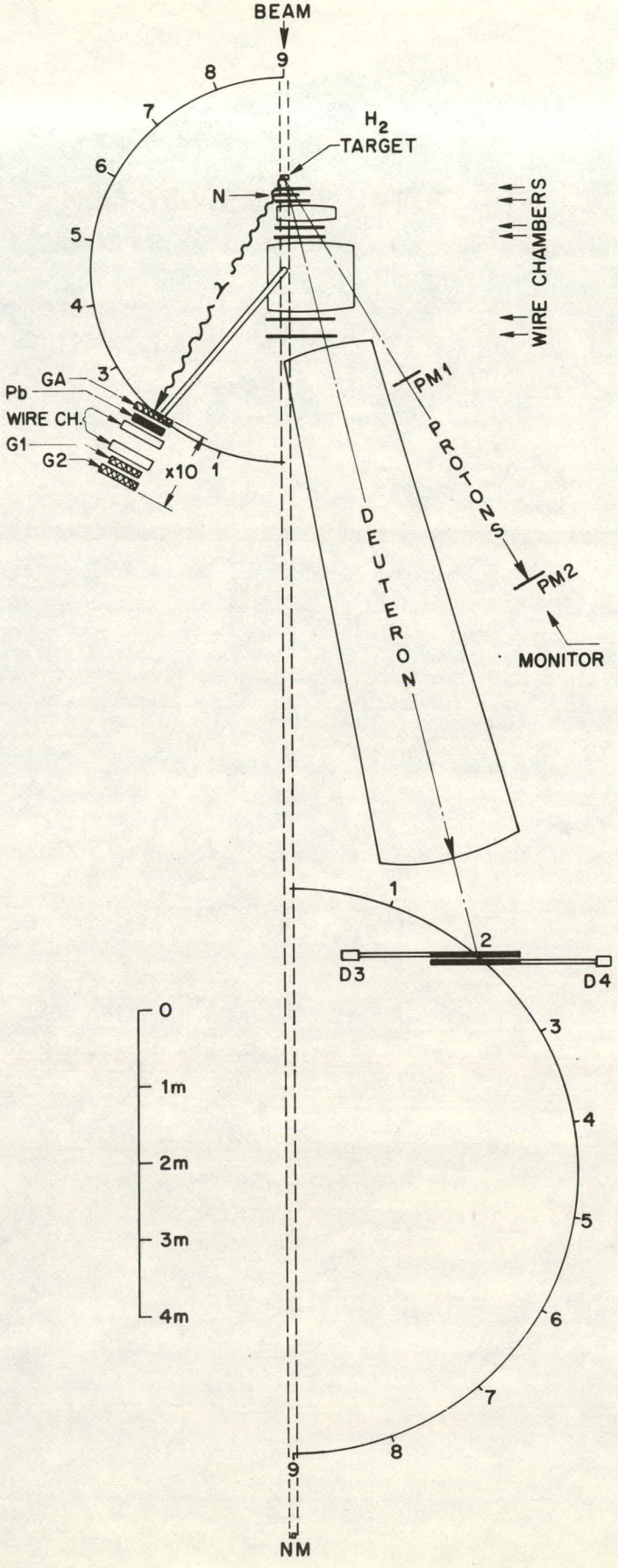
BEAM
9
8
7
6
5
4
3
H_2
TARGET
N
γ
WIRE CHAMBERS
GA
Pb
WIRE CH.
G1
G2
x10
1
PM1
PROTONS
DEUTERON
PM2
MONITOR
1
2
D3
D4
0
1m
2m
3m
4m
3
4
5
6
7
8
9
NM

FIGURE II.1

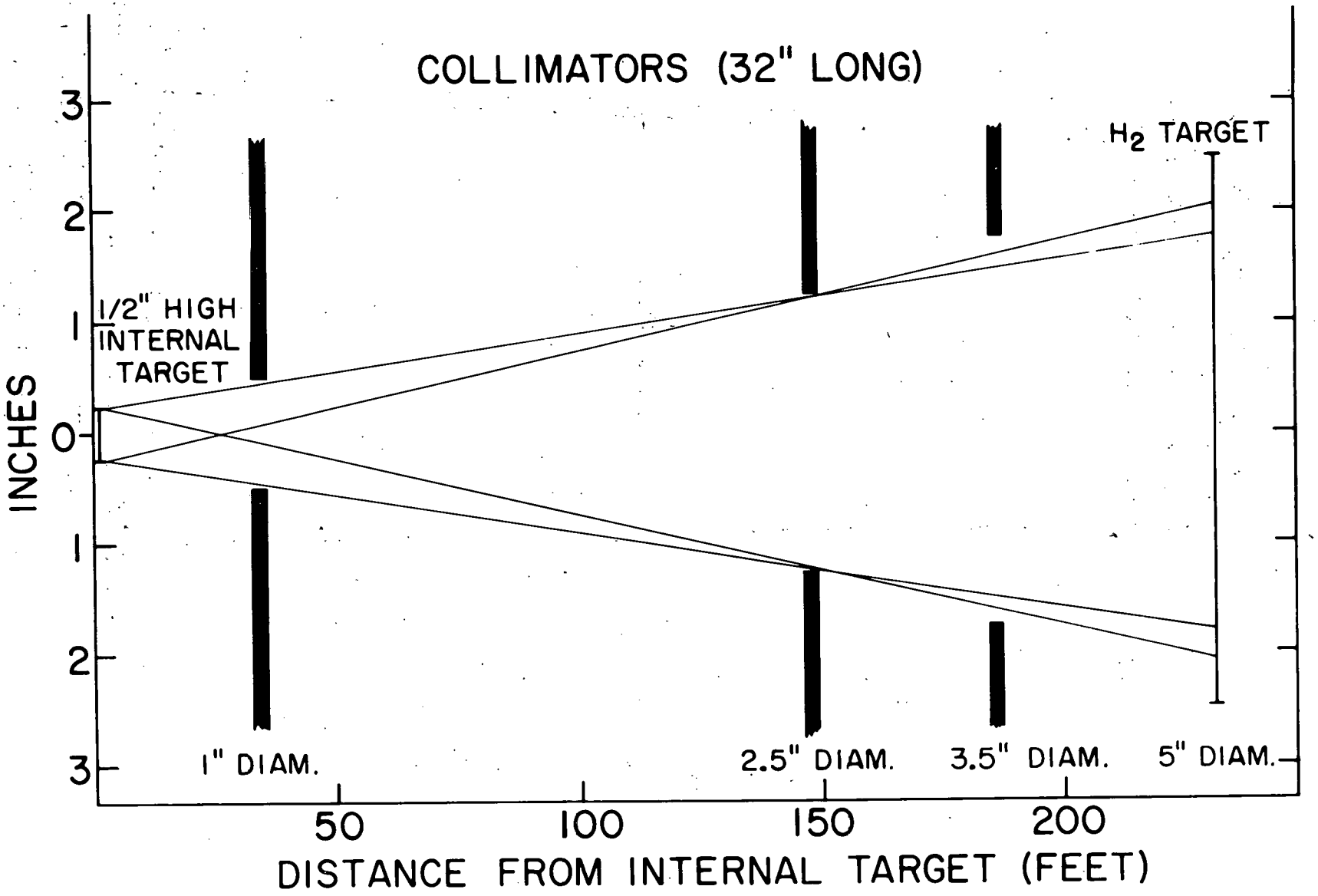
COLLIMATORS (32" LONG)
H_2 TARGET
1/2" HIGH INTERNAL TARGET
INCHES
3
2
1
0
1
2
3
1" DIAM.
2.5" DIAM.
3.5" DIAM.
5" DIAM.
50
100
150
200
DISTANCE FROM INTERNAL TARGET (FEET)

FIGURE II.5

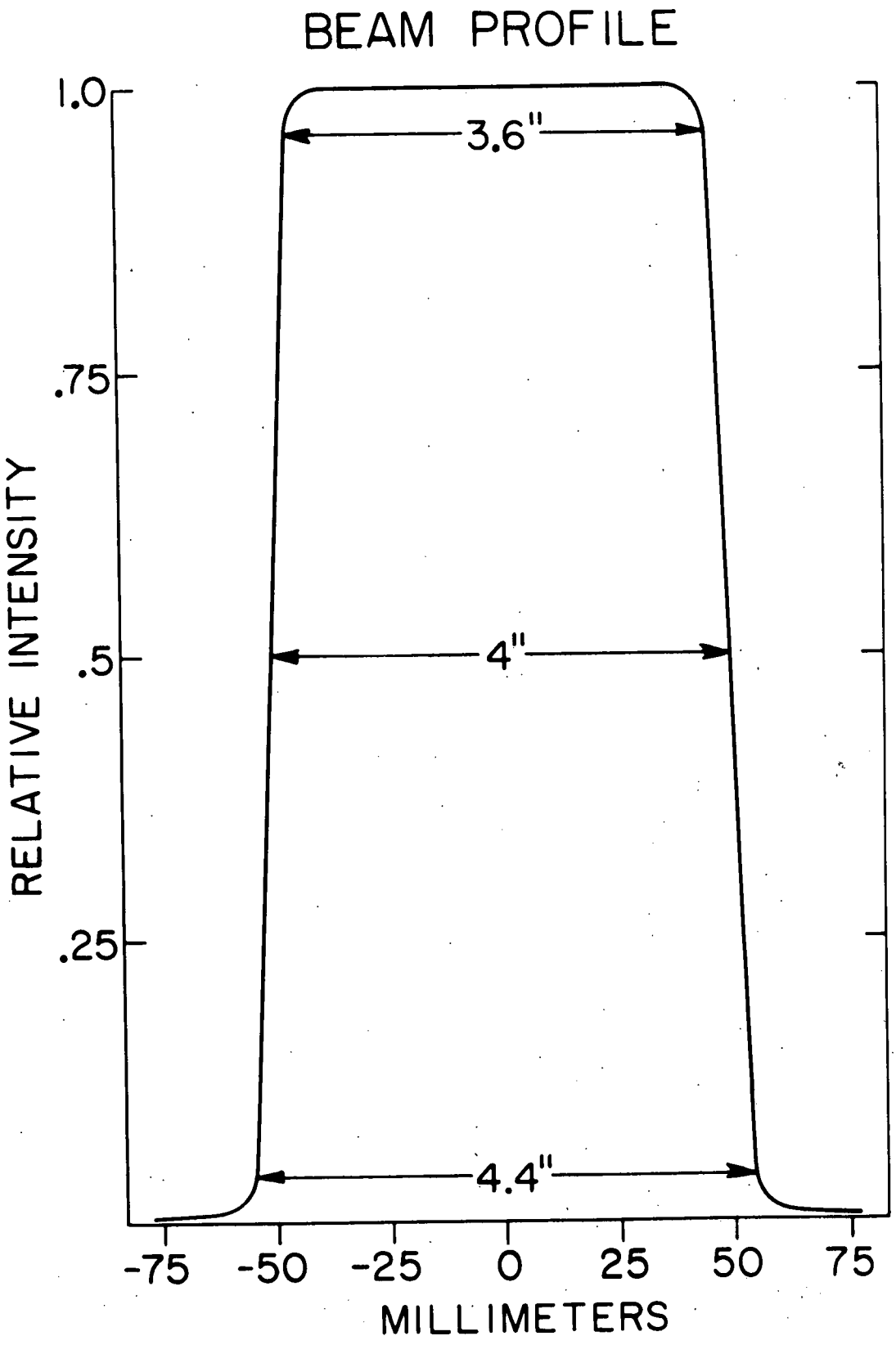
BEAM PROFILE
1.0
.75
.5
.25
RELATIVE INTENSITY
3.6"
4"
4.4"
-75
-50
-25
0
25
50
75
MILLIMETERS

FIGURE II.6

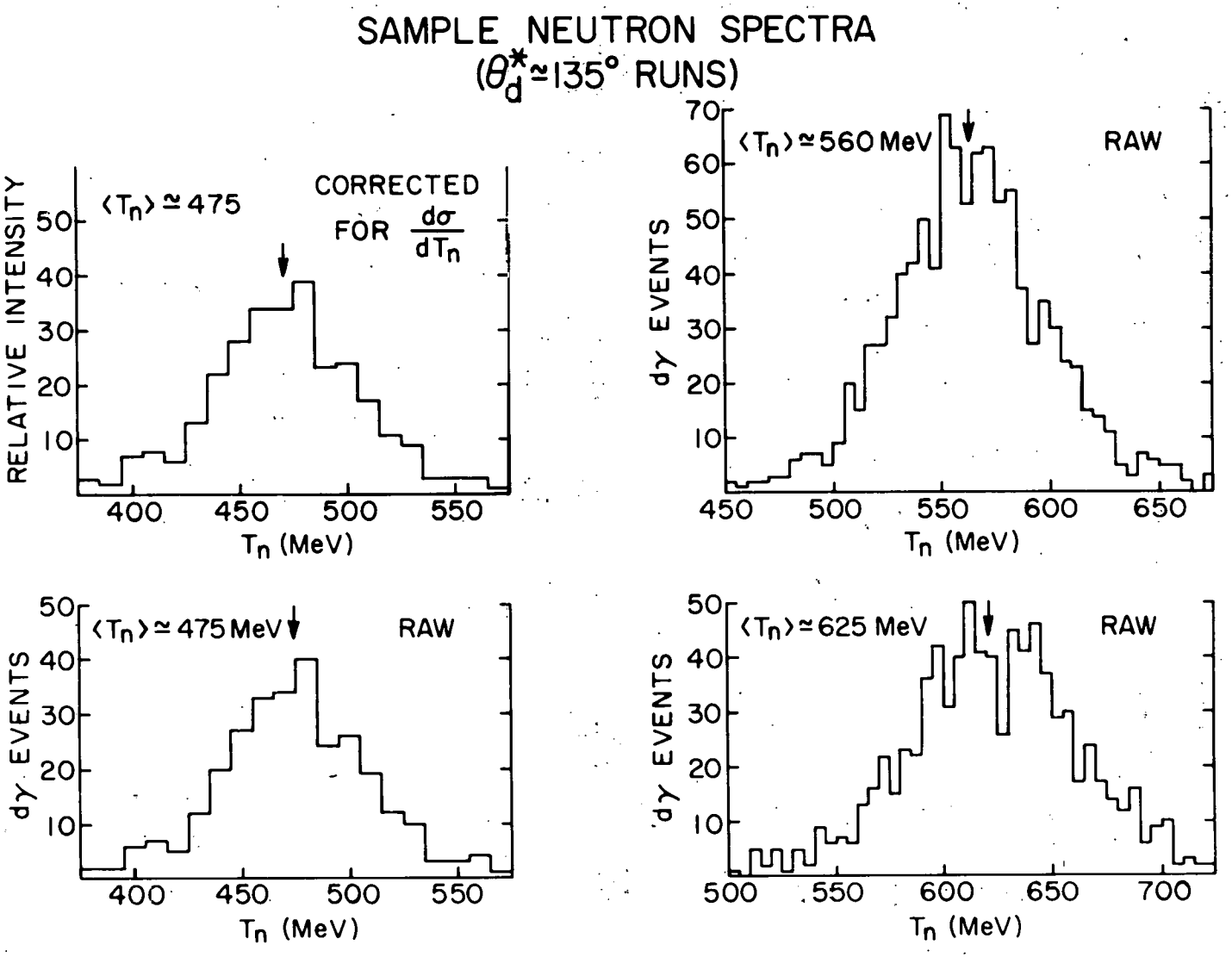
SAMPLE NEUTRON SPECTRA
($\theta_d^* \simeq 135°$ RUNS)
$\langle T_n \rangle \simeq 475$
CORRECTED FOR $\frac{d\sigma}{dT_n}$
RELATIVE INTENSITY
T_n (MeV)
$\langle T_n \rangle \simeq 560$ MeV
RAW
dγ EVENTS
T_n (MeV)
$\langle T_n \rangle \simeq 475$ MeV
RAW
dγ EVENTS
T_n (MeV)
$\langle T_n \rangle \simeq 625$ MeV
RAW
dγ EVENTS
T_n (MeV)

FIGURE II.7

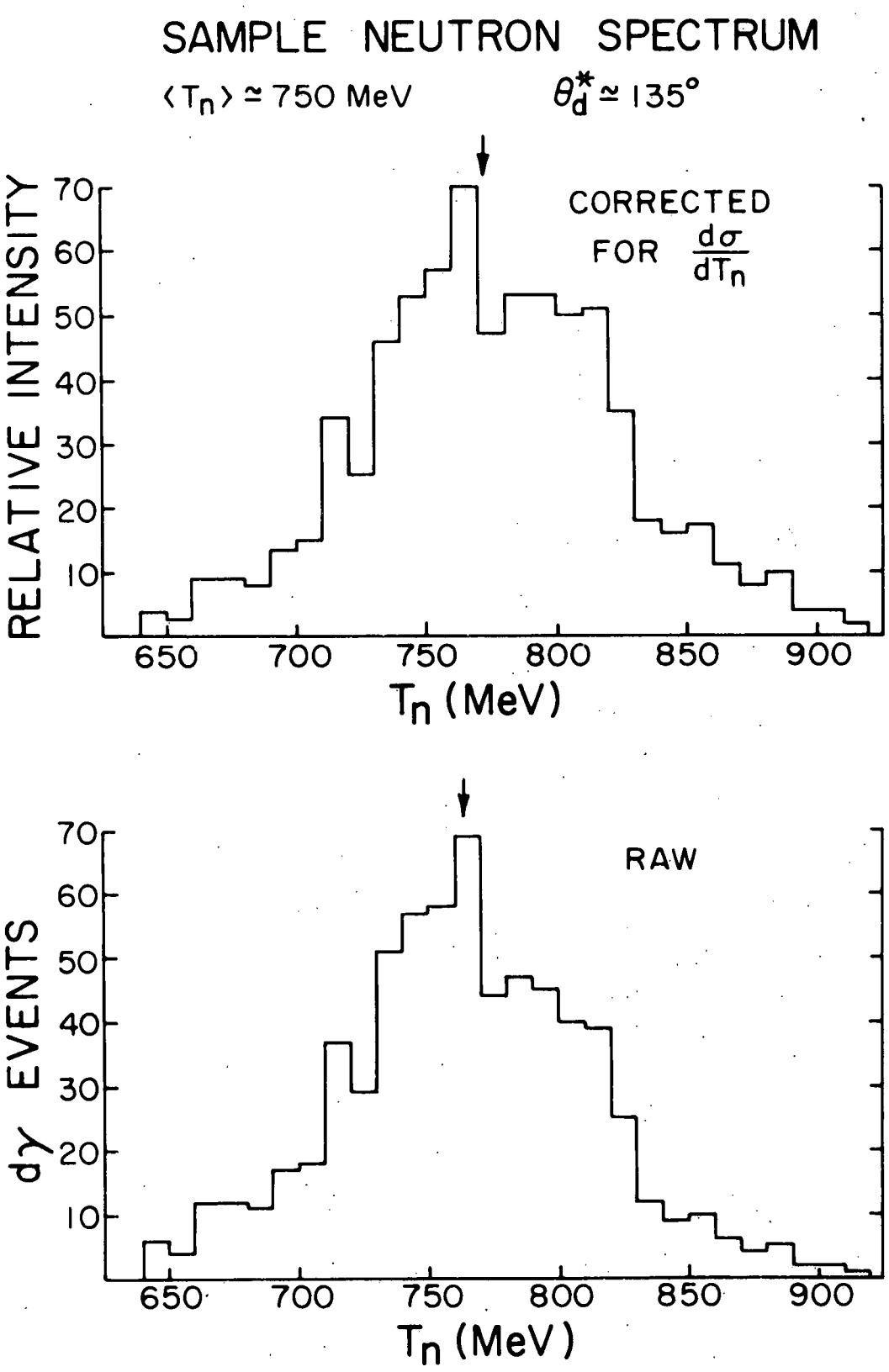
SAMPLE NEUTRON SPECTRUM
⟨Tn⟩ ≃ 750 MeV
θ*d ≃ 135°
CORRECTED FOR dσ/dTn
RELATIVE INTENSITY
70
60
50
40
30
20
10
650
700
750
800
850
900
Tn (MeV)
RAW
dγ EVENTS
70
60
50
40
30
20
10
650
700
750
800
850
900
Tn (MeV)

FIGURE II.8

3

LIQUID HYDROGEN TARGET

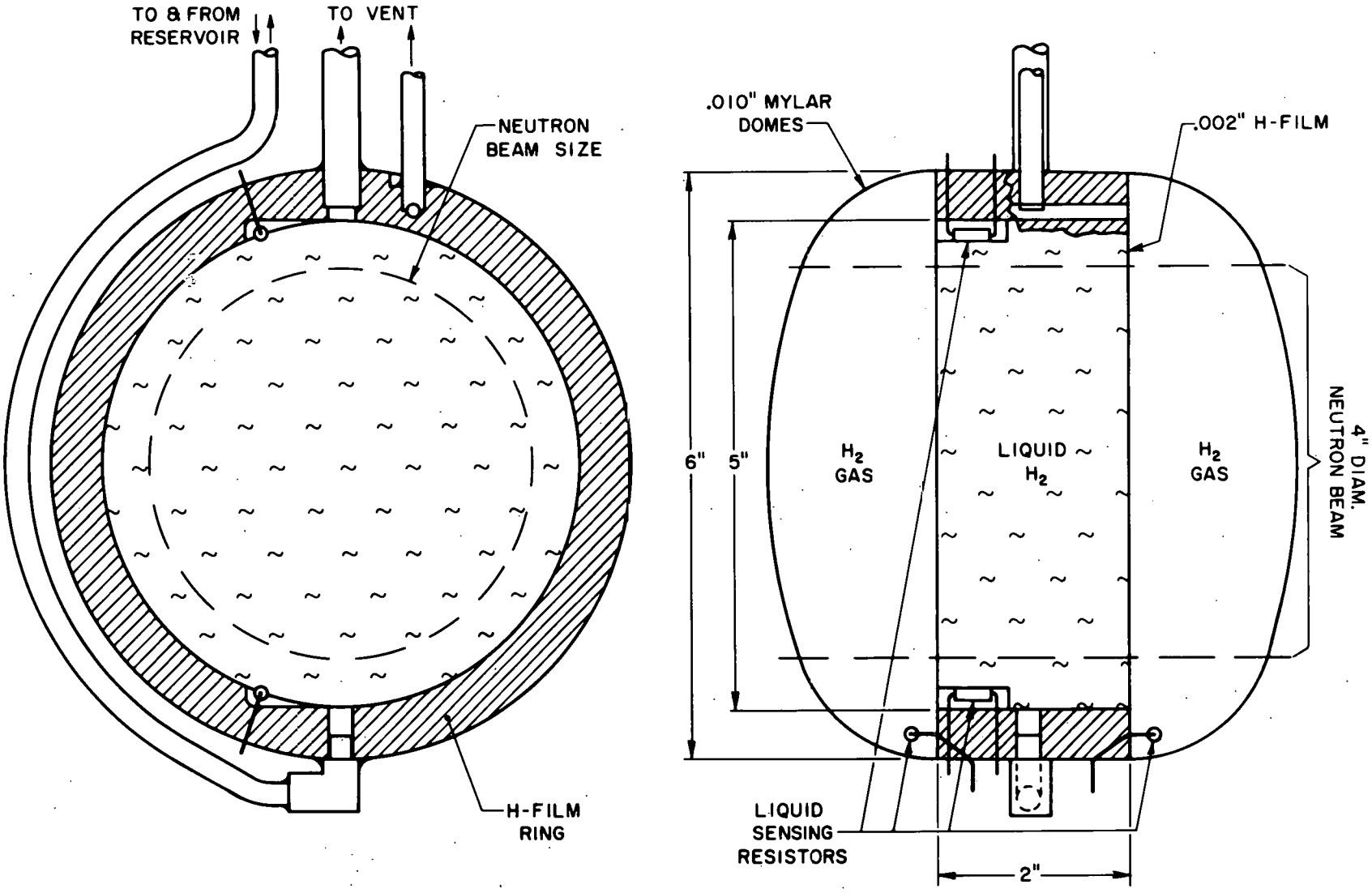

FIG. II.9

VARIATION OF TIME WITH POSITION

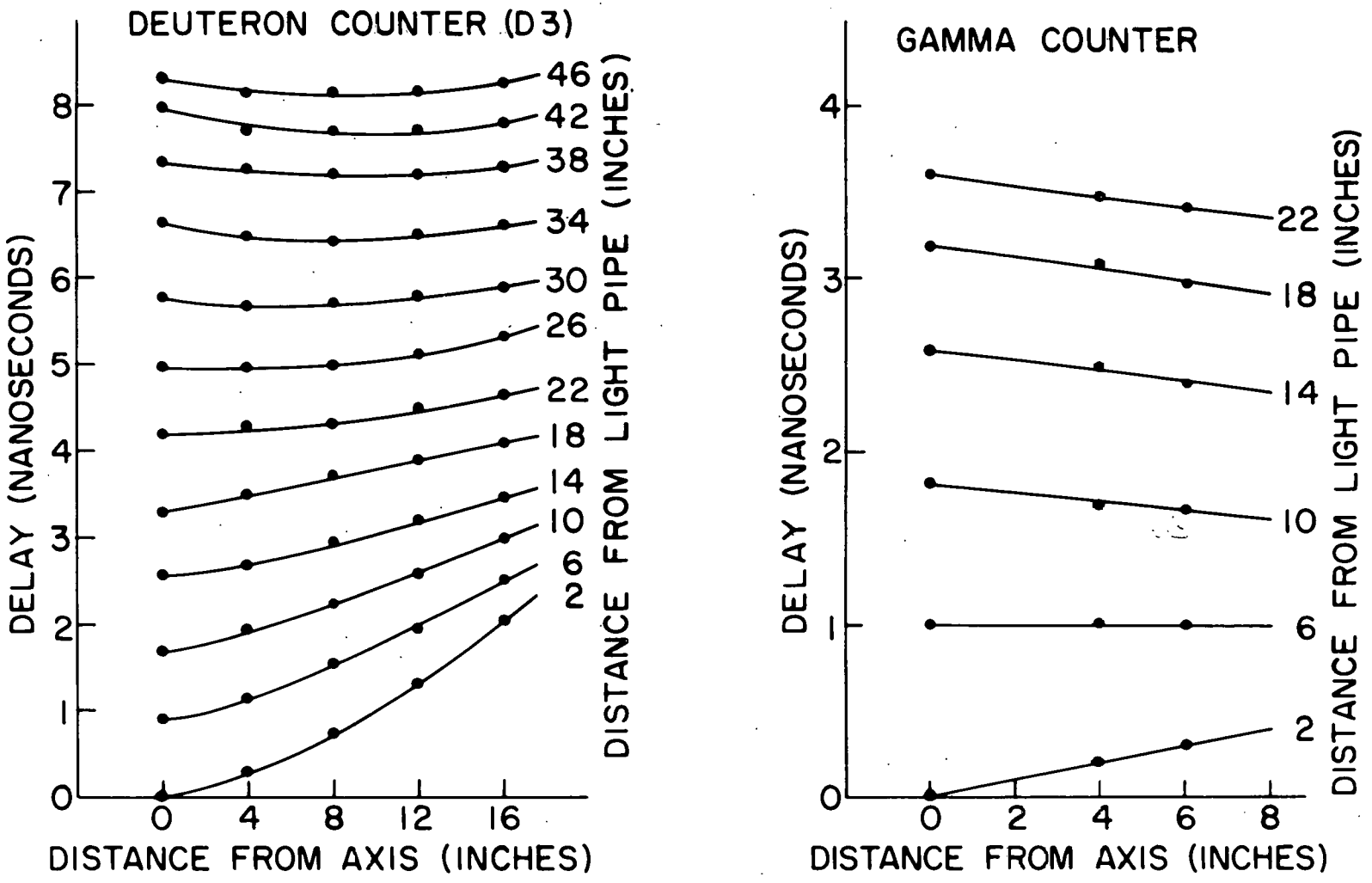

FIGURE II.10

SPARK CHAMBER CONSTRUCTION

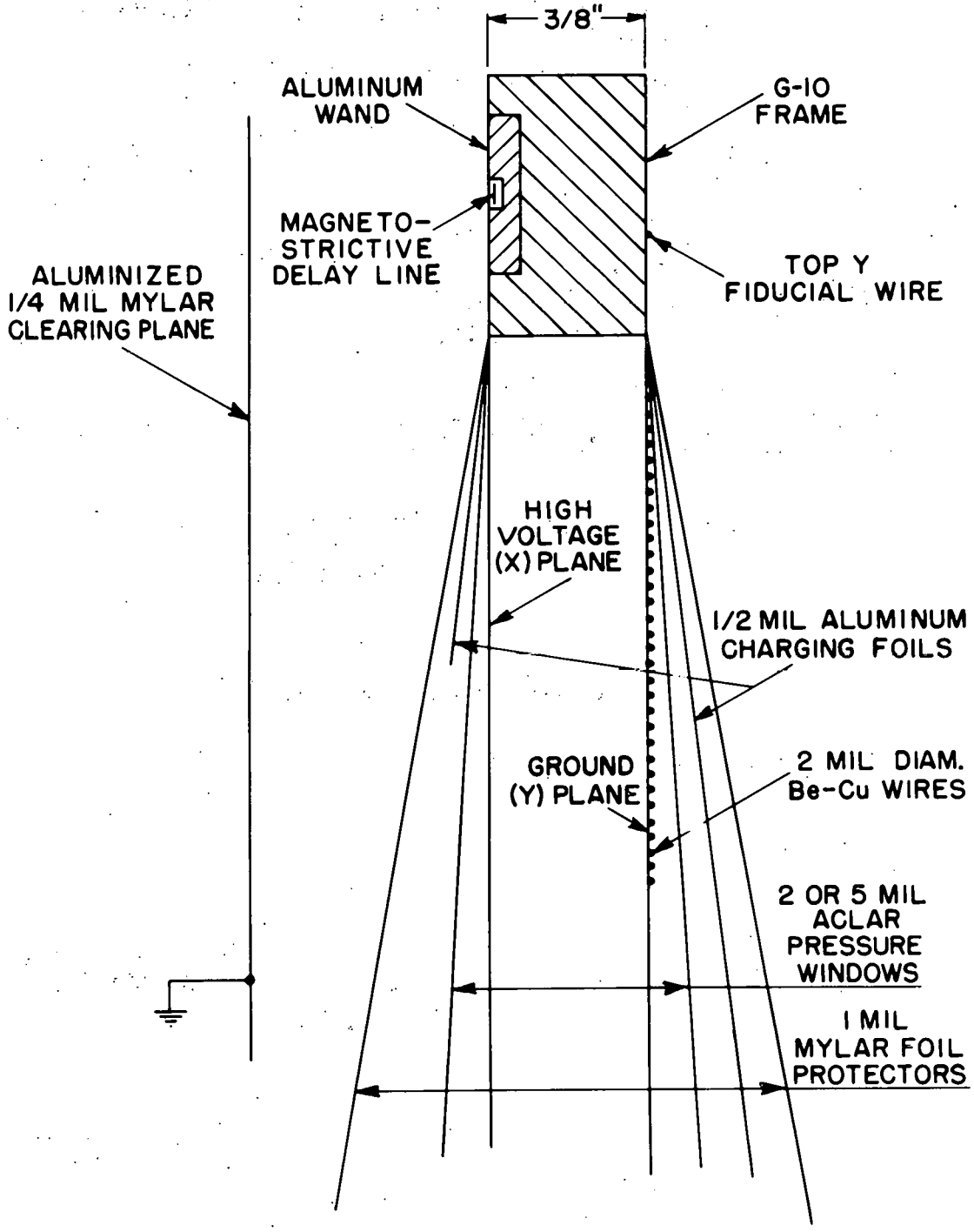

FIGURE II.11

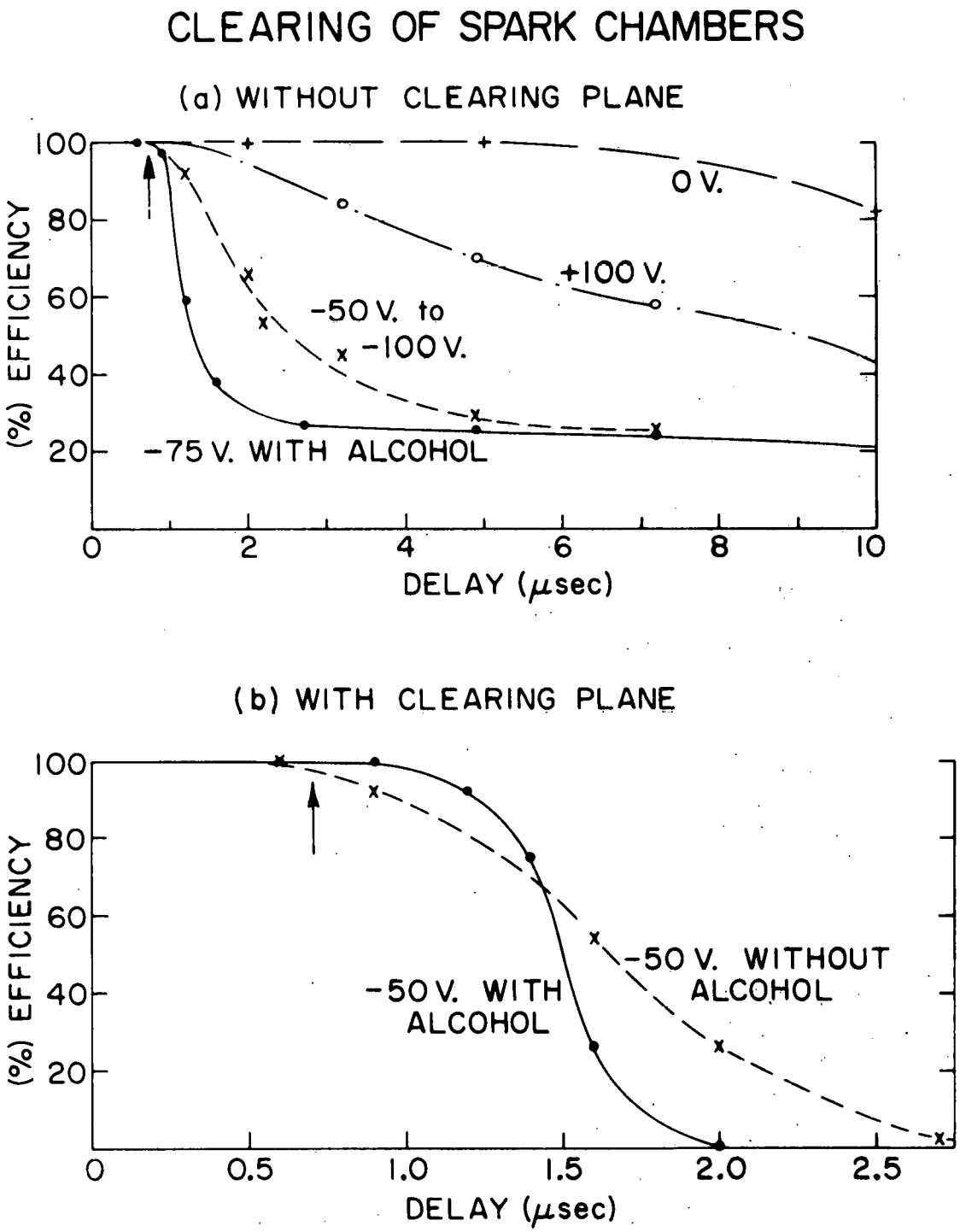
CLEARING OF SPARK CHAMBERS
(a) WITHOUT CLEARING PLANE
(%) EFFICIENCY
100
80
60
40
20
0
2
4
6
8
10
DELAY (μsec)
0 V.
+100 V.
-50 V. to
-100 V.
-75 V. WITH ALCOHOL
(b) WITH CLEARING PLANE
(%) EFFICIENCY
100
80
60
40
20
0
0.5
1.0
1.5
2.0
2.5
DELAY (μsec)
-50 V. WITHOUT
ALCOHOL
-50 V. WITH
ALCOHOL

FIGURE II.12

SPARK CHAMBER HIGH VOLTAGE PULSING SYSTEM

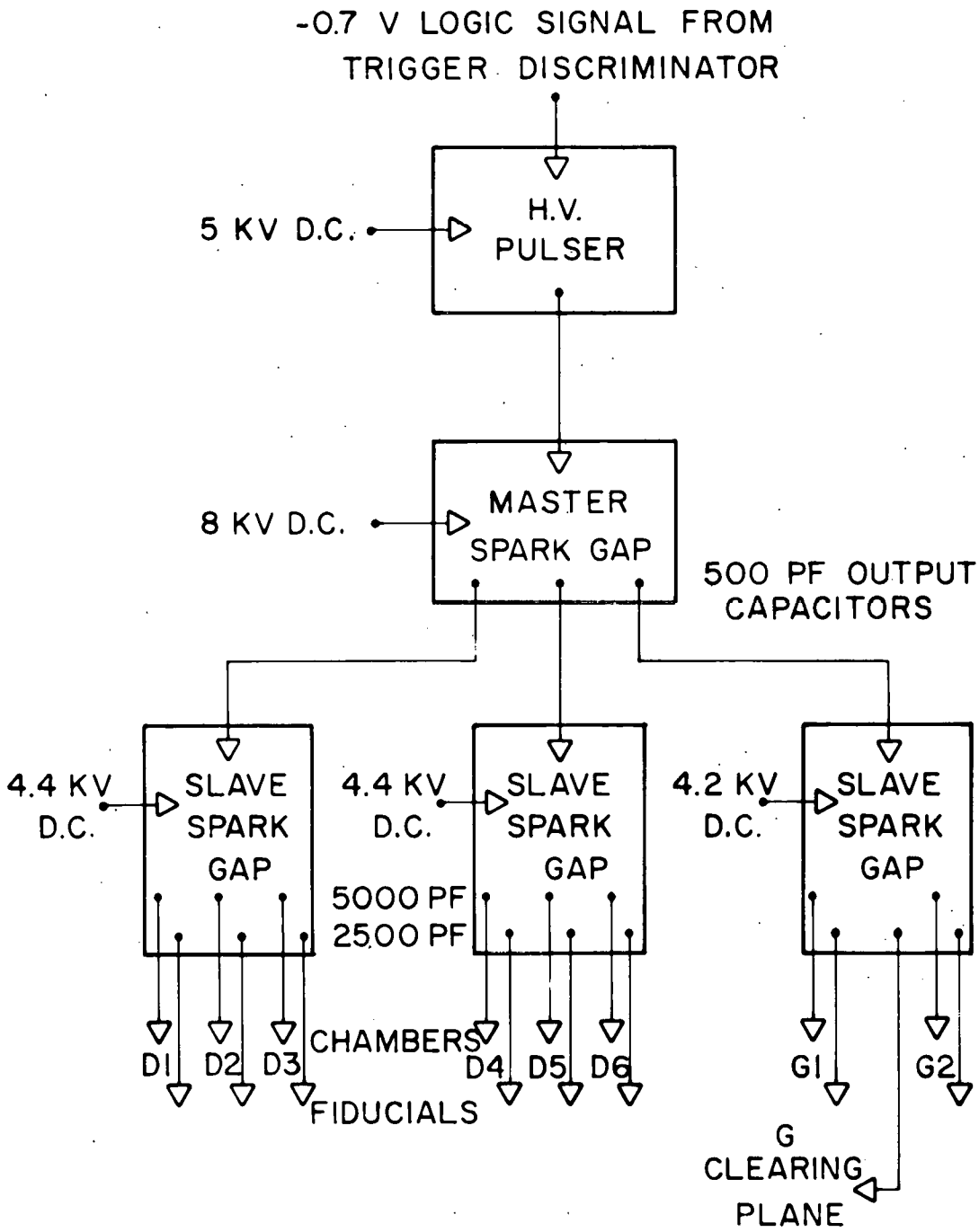

FIGURE II.13

EVENT TRIGGER LOGIC

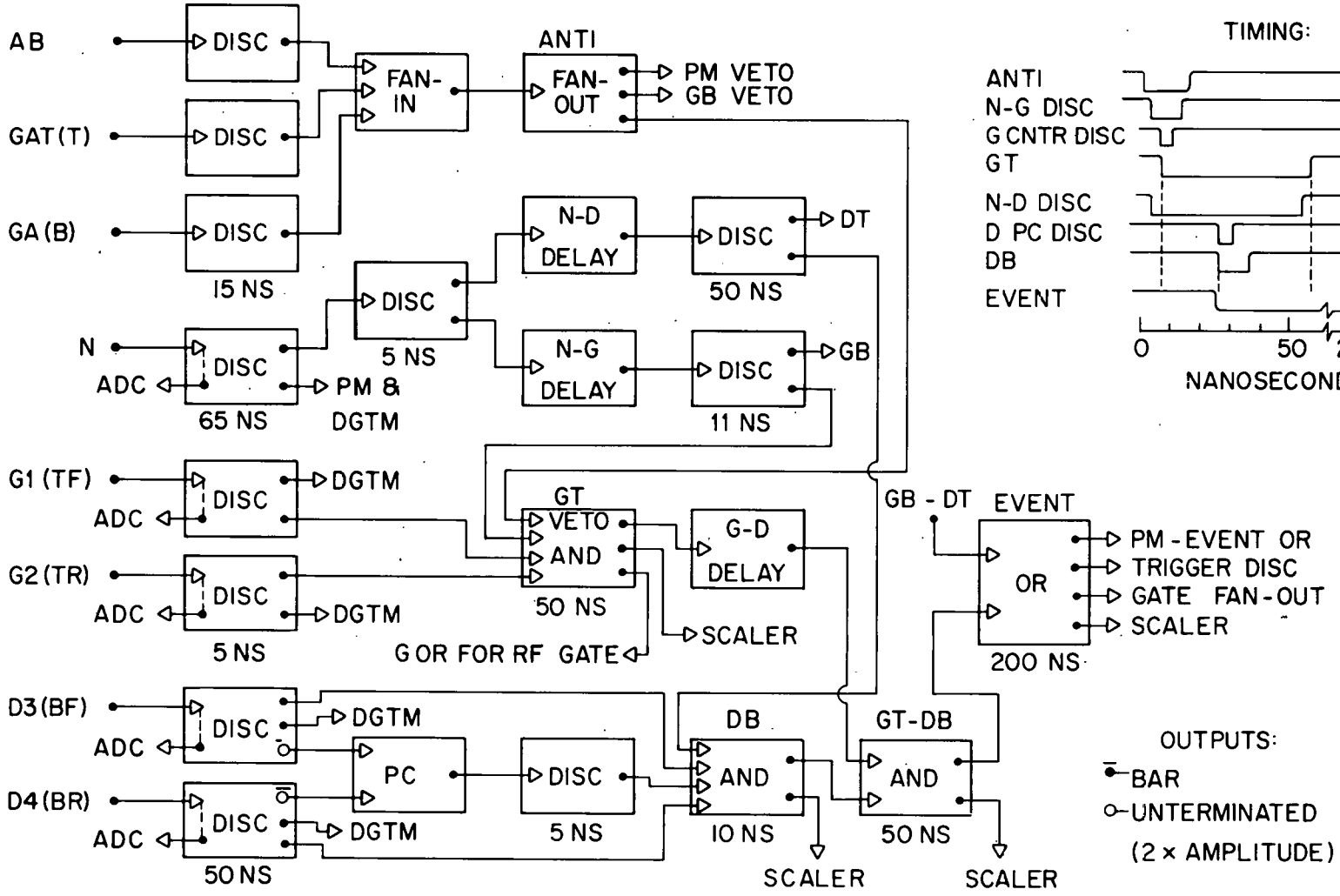

FIGURE II.14

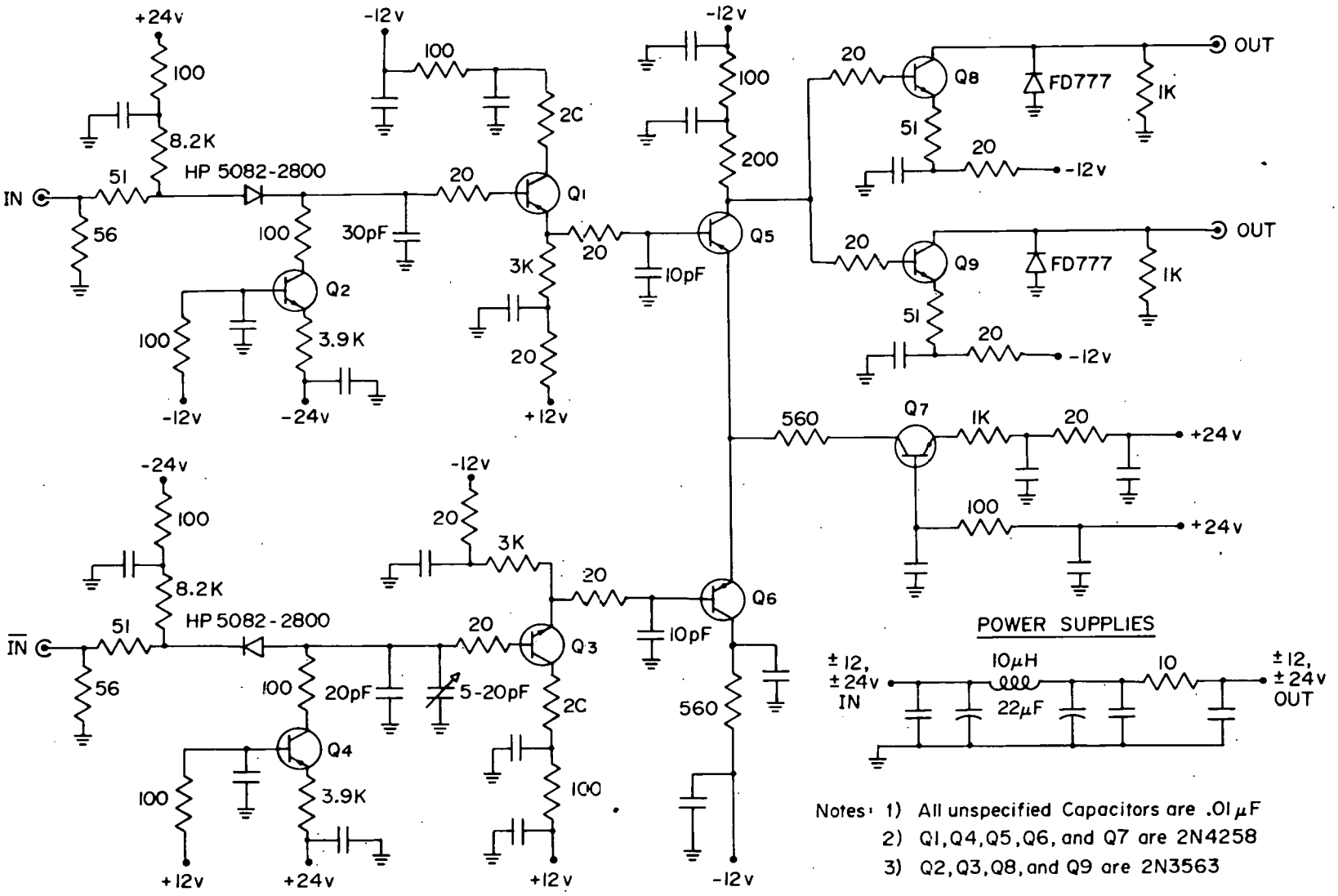
POSITION COMPENSATOR
+24v
-12v
-12v
100
8.2K
HP 5082-2800
51
IN
56
100
30pF
2C
20
Q1
3K
20
10pF
Q5
200
100
Q2
3.9K
100
-12v
-24v
+12v
20
Q8
FD777
1K
51
20
-12v
OUT
Q9
560
Q7
1K
20
+24v
100
-24v
-12v
20
3K
8.2K
HP 5082-2800
IN
51
56
100
20pF
5-20pF
20
Q3
2C
Q6
560
Q4
3.9K
100
+12v
+24v
+12v
-12v
POWER SUPPLIES
±12, ±24v IN
10μH
22μF
10
±12, ±24v OUT
Notes: 1) All unspecified Capacitors are .01μF
2) Q1, Q4, Q5, Q6, and Q7 are 2N4258
3) Q2, Q3, Q8, and Q9 are 2N3563

FIGURE II.15

PROTON MONITOR LOGIC

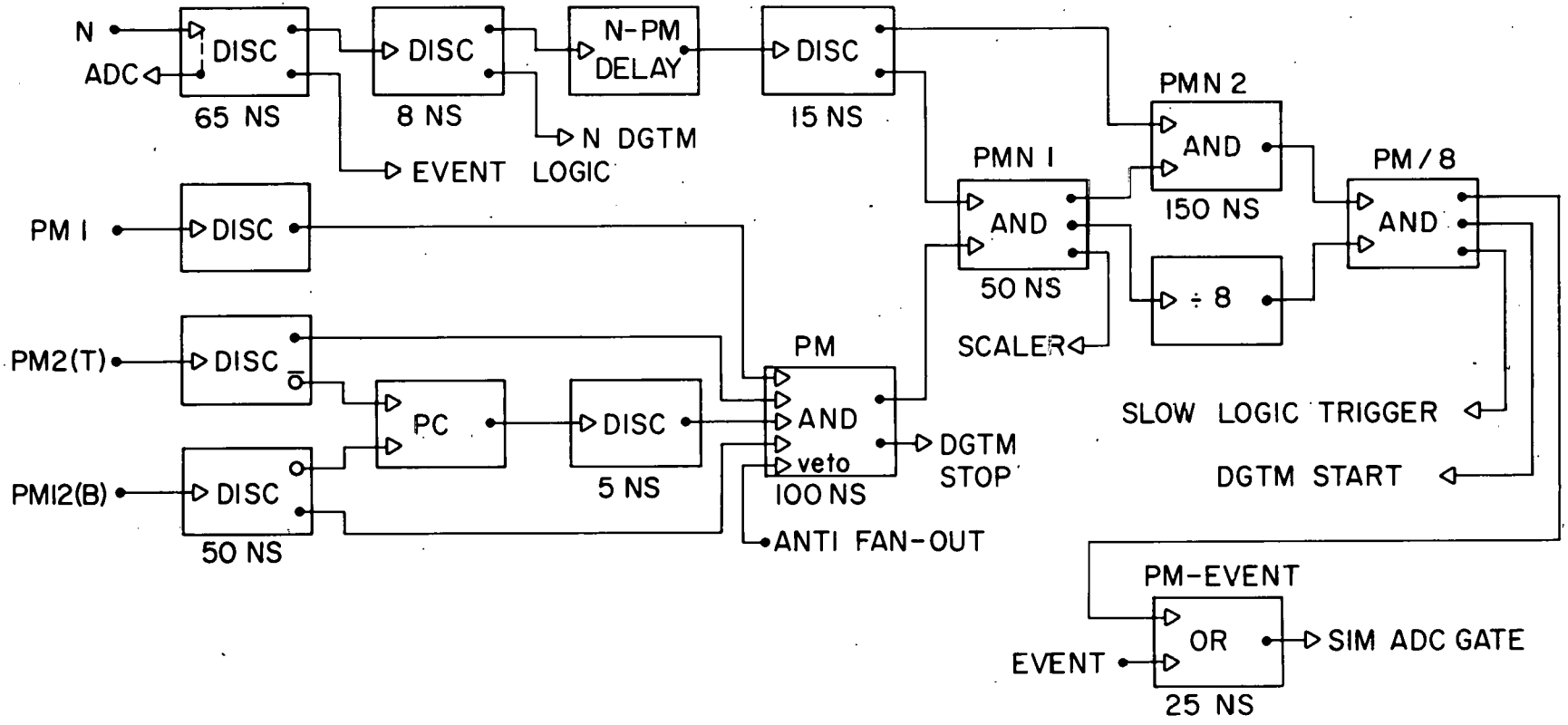

FIGURE II.16

RF BUCKET SELECTION AND TIMING LOGIC

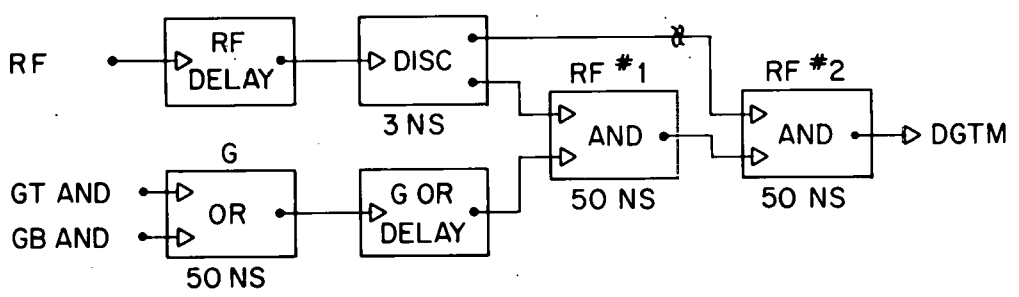

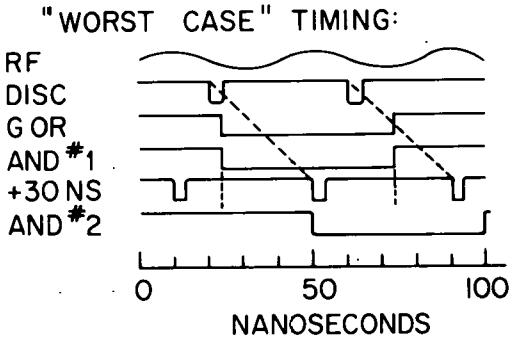

DIGITIME LOGIC

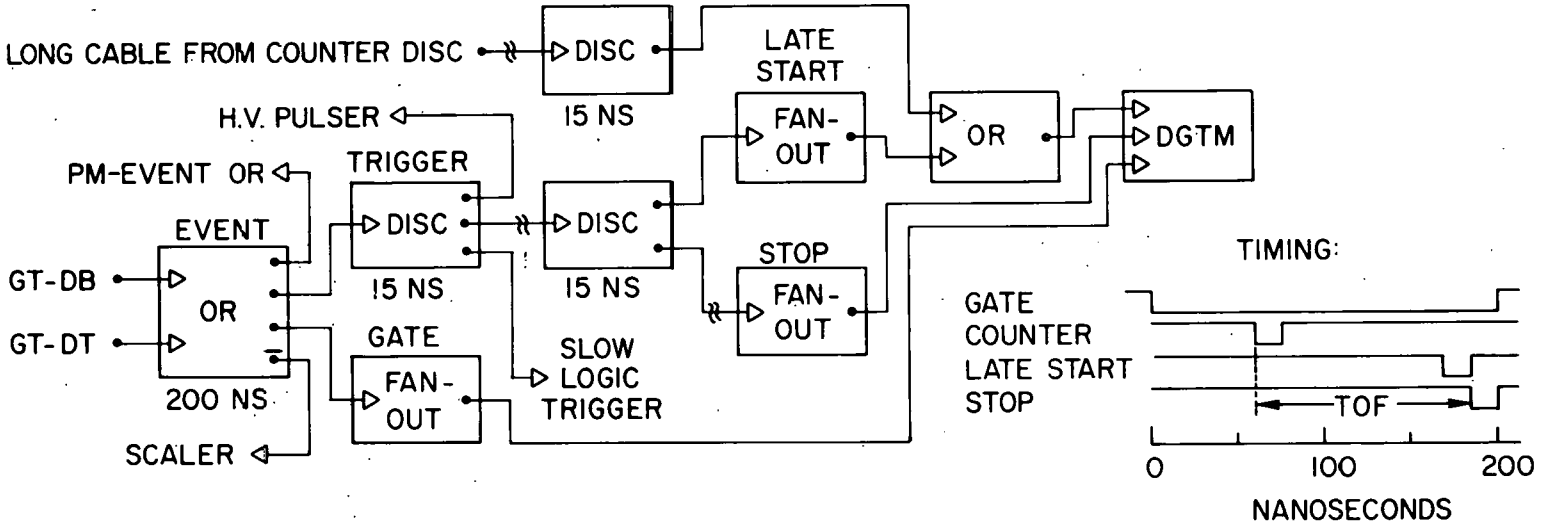

FIGURE II.17

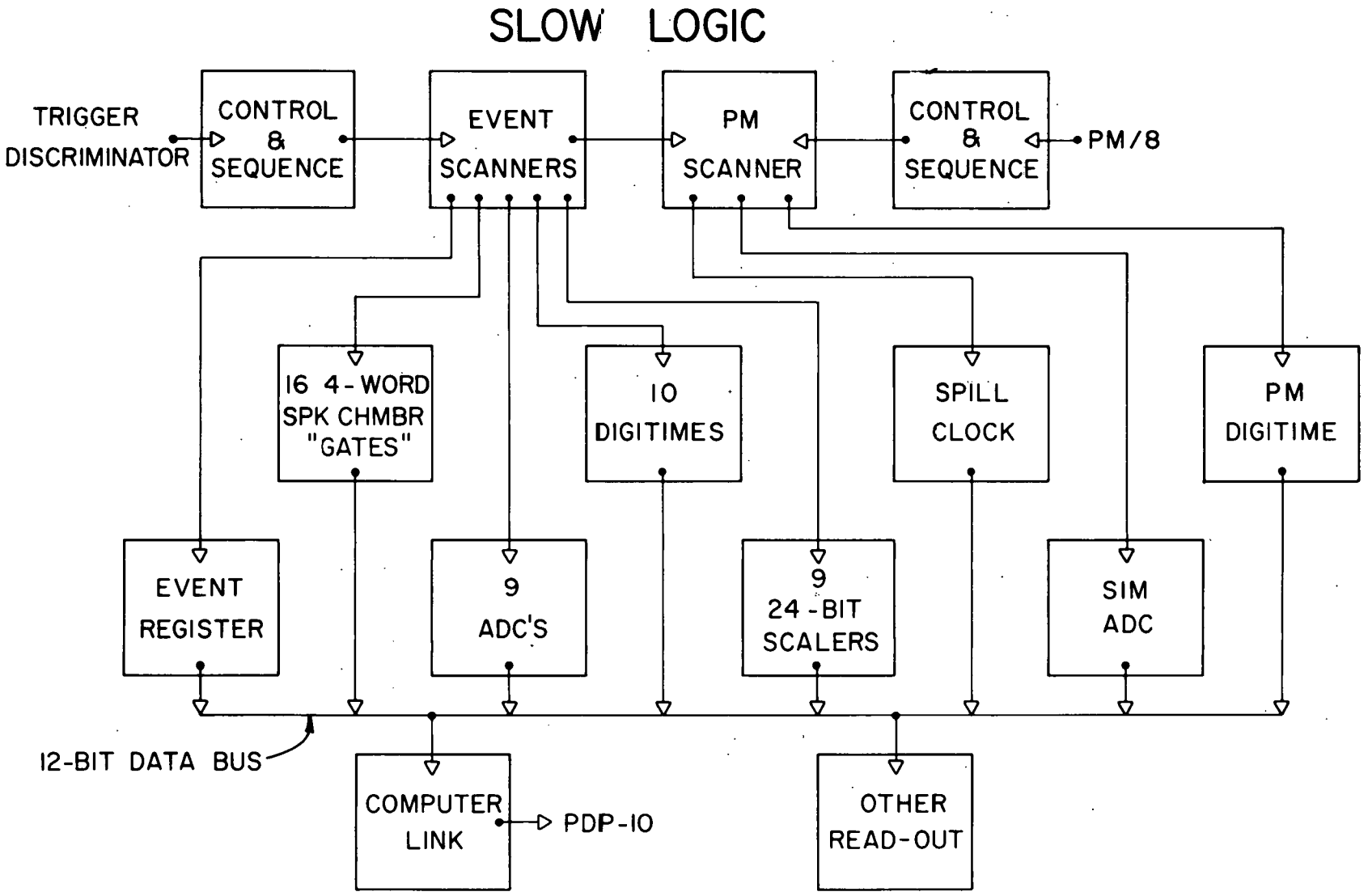
SLOW LOGIC
TRIGGER DISCRIMINATOR
CONTROL & SEQUENCE
EVENT SCANNERS
PM SCANNER
CONTROL & SEQUENCE
PM/8
16 4-WORD SPK CHMBR "GATES"
10 DIGITIMES
SPILL CLOCK
PM DIGITIME
EVENT REGISTER
9 ADC'S
9 24-BIT SCALERS
SIM ADC
12-BIT DATA BUS
COMPUTER LINK
PDP-10
OTHER READ-OUT

FIGURE II.18

CROSS SECTION OF HELIUM BAG SEAM

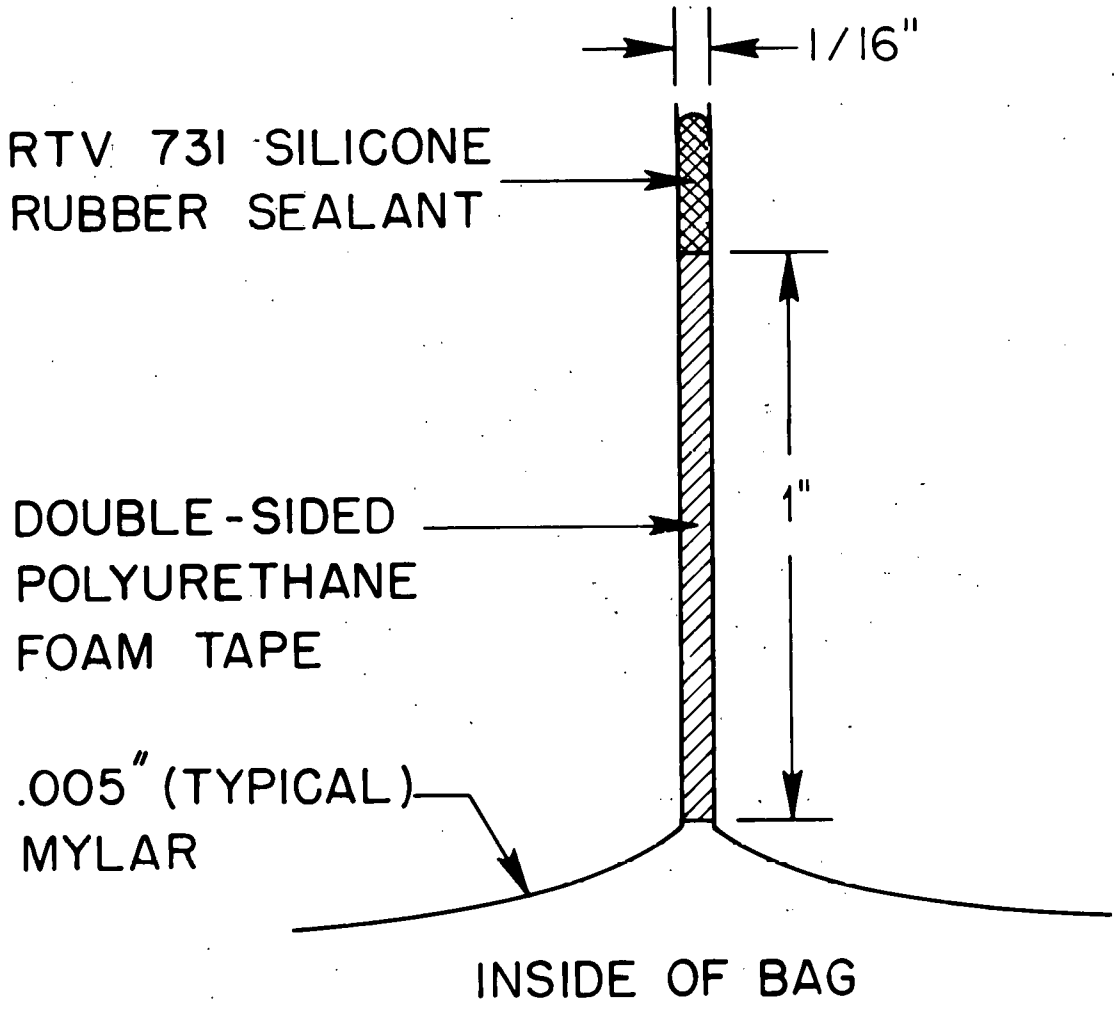

FIGURE II.19

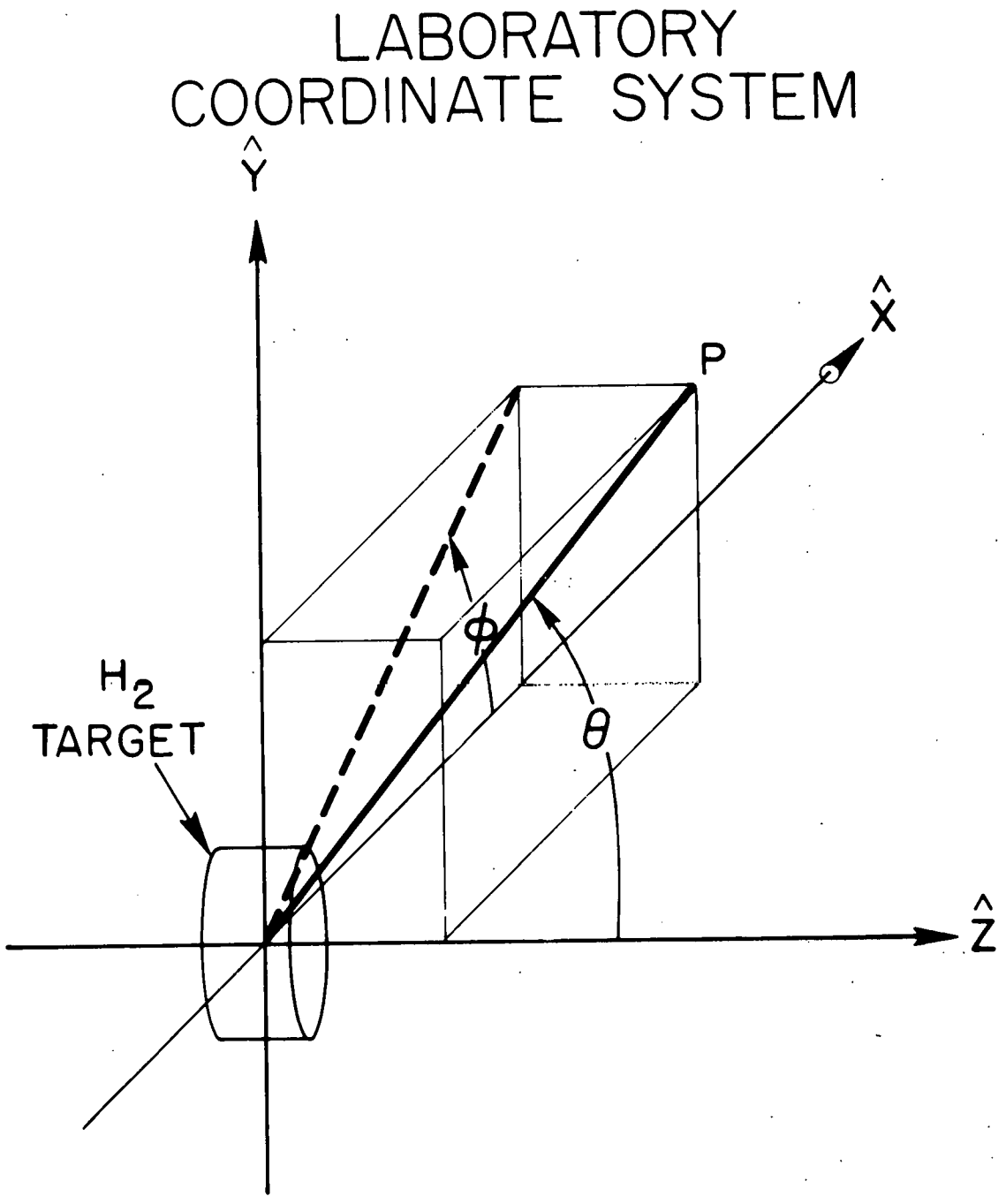

FIGURE III.1

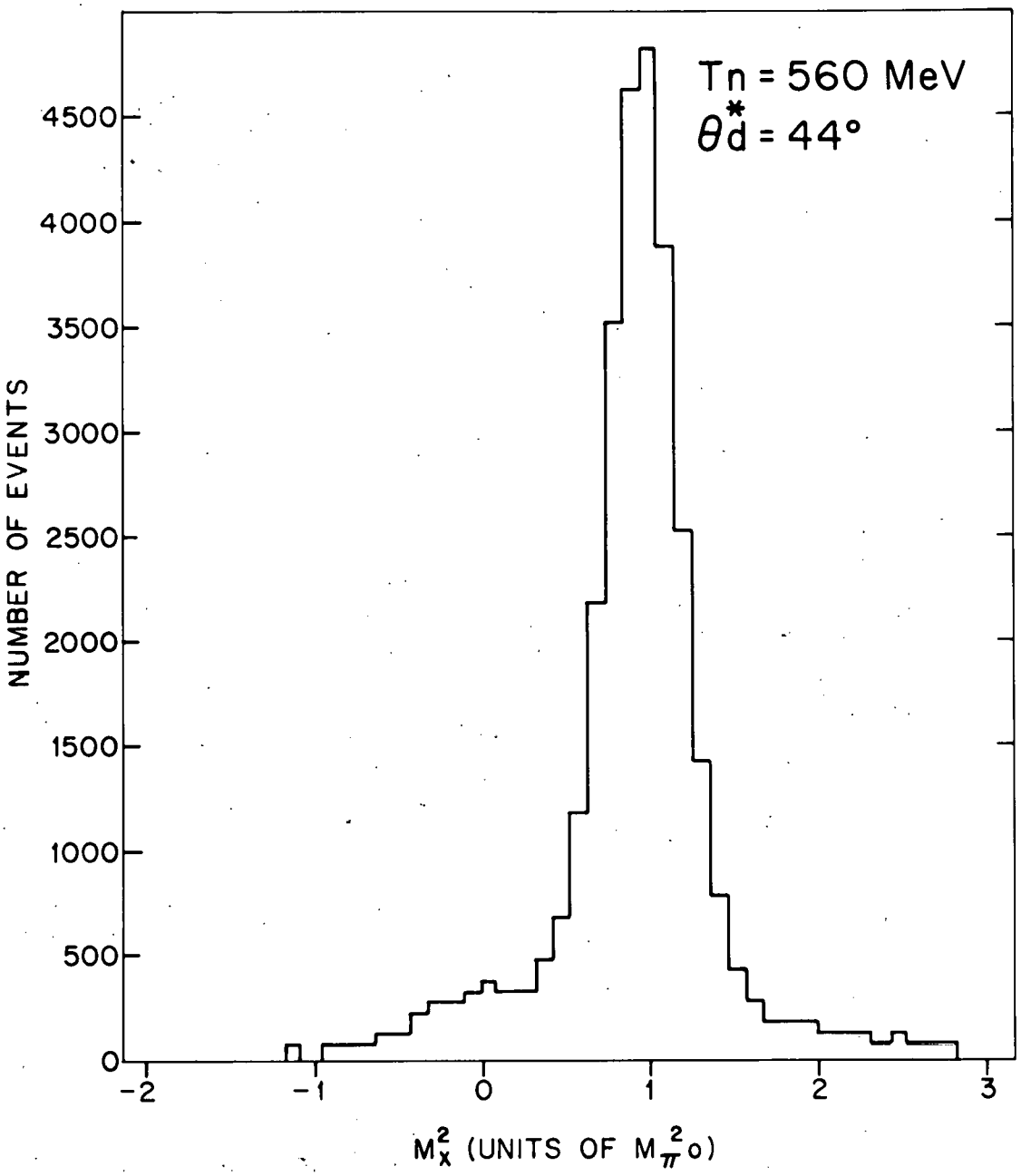
Tn = 560 MeV
θ*d = 44°
NUMBER OF EVENTS
4500
4000
3500
3000
2500
2000
1500
1000
500
0
-2
-1
0
1
2
3
M²x (UNITS OF Mπ²o)

FIGURE III.2

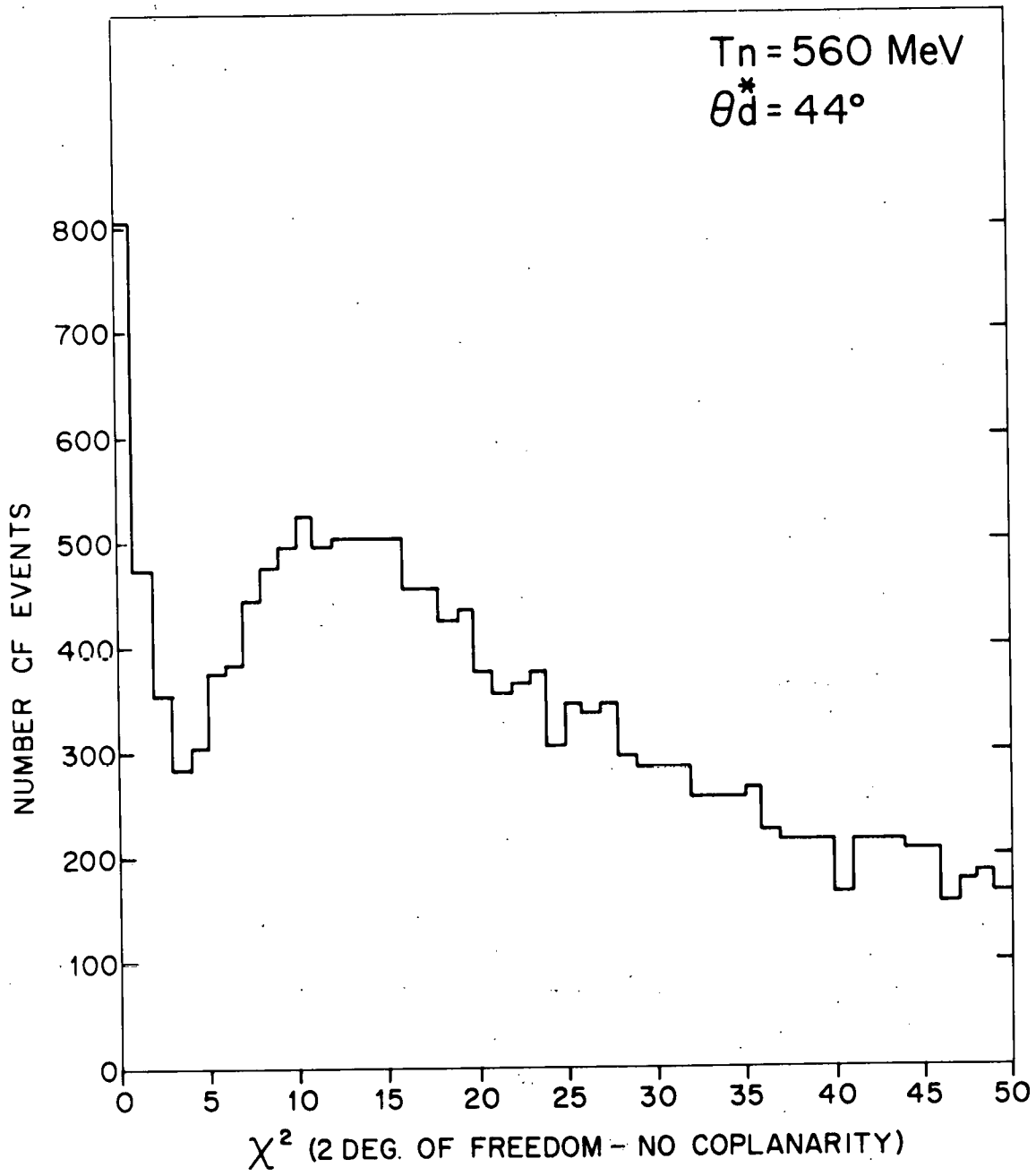
Tn = 560 MeV
θ*d = 44°
NUMBER CF EVENTS
800
700
600
500
400
300
200
100
0
0
5
10
15
20
25
30
35
40
45
50
χ² (2 DEG. OF FREEDOM – NO COPLANARITY)

FIGURE III.3

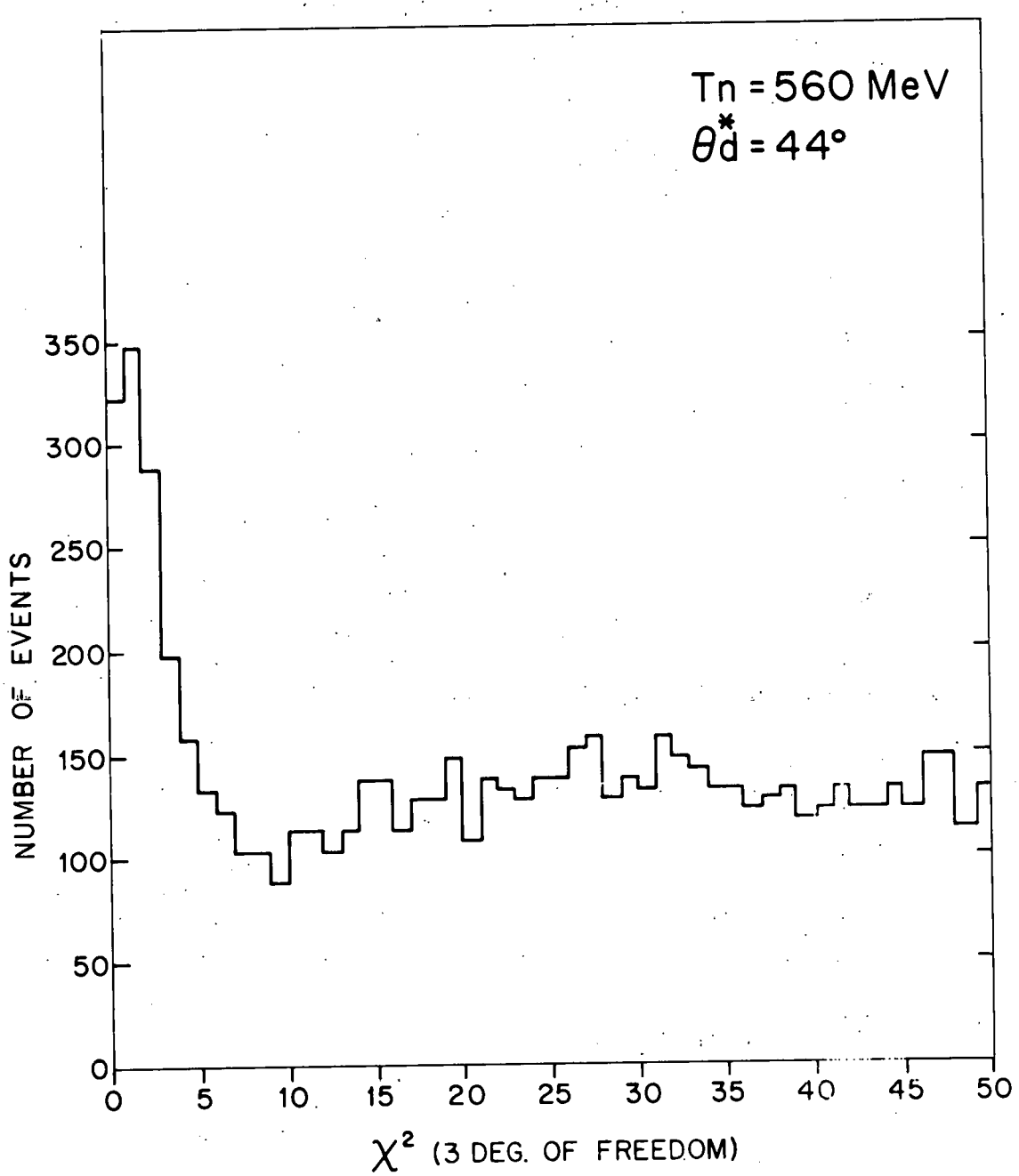
Tn = 560 MeV
θ*d = 44°
NUMBER OF EVENTS
350
300
250
200
150
100
50
0
0
5
10
15
20
25
30
35
40
45
50
χ² (3 DEG. OF FREEDOM)

FIGURE III.4

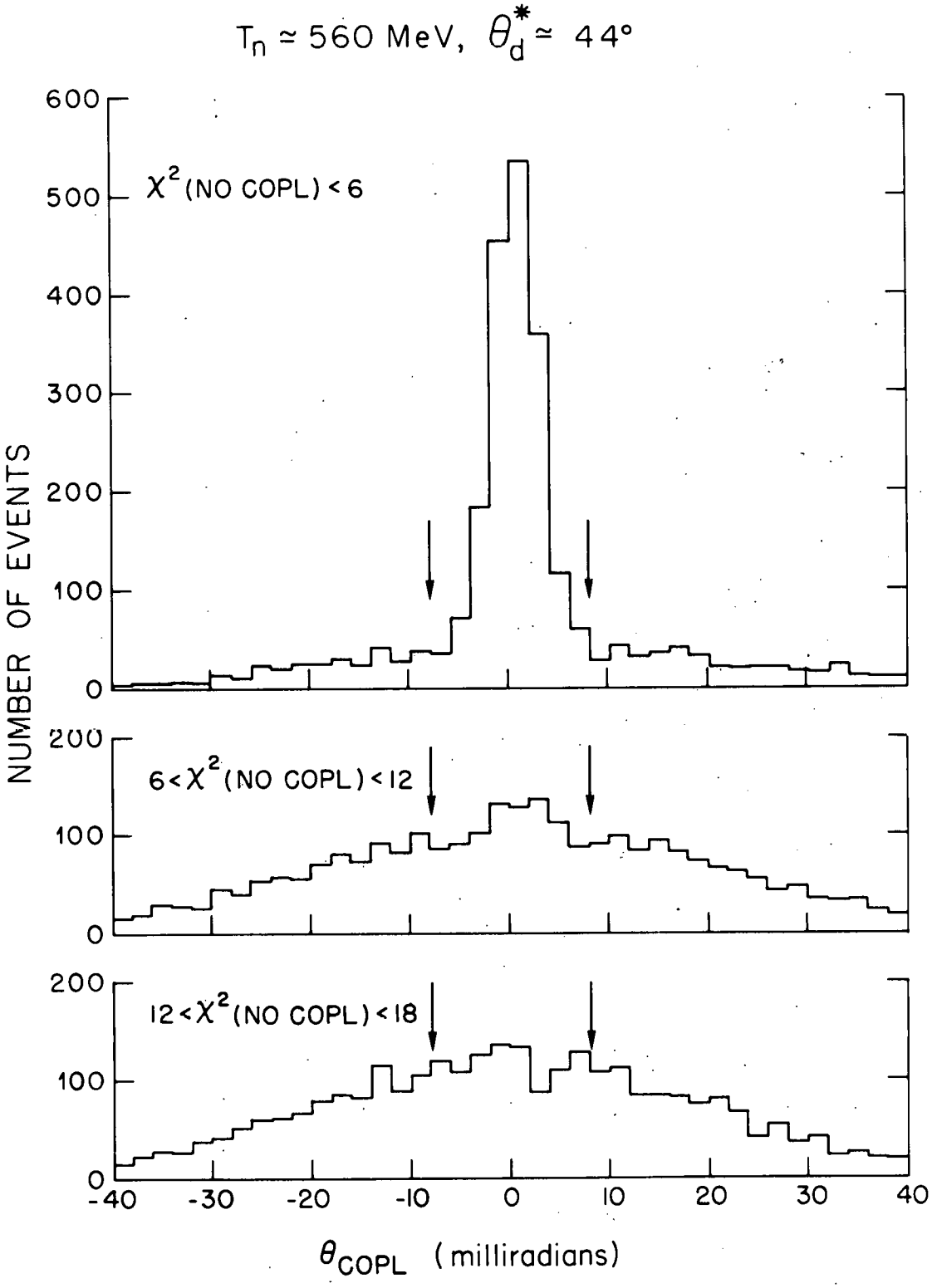
$T_n \simeq 560$ MeV, $\theta_d^* \simeq 44°$
χ^2(NO COPL) < 6
6 < χ^2(NO COPL) < 12
12 < χ^2(NO COPL) < 18
NUMBER OF EVENTS
600
500
400
300
200
100
0
200
100
0
200
100
0
-40
-30
-20
-10
0
10
20
30
40
θ_{COPL} (milliradians)

FIGURE III.5

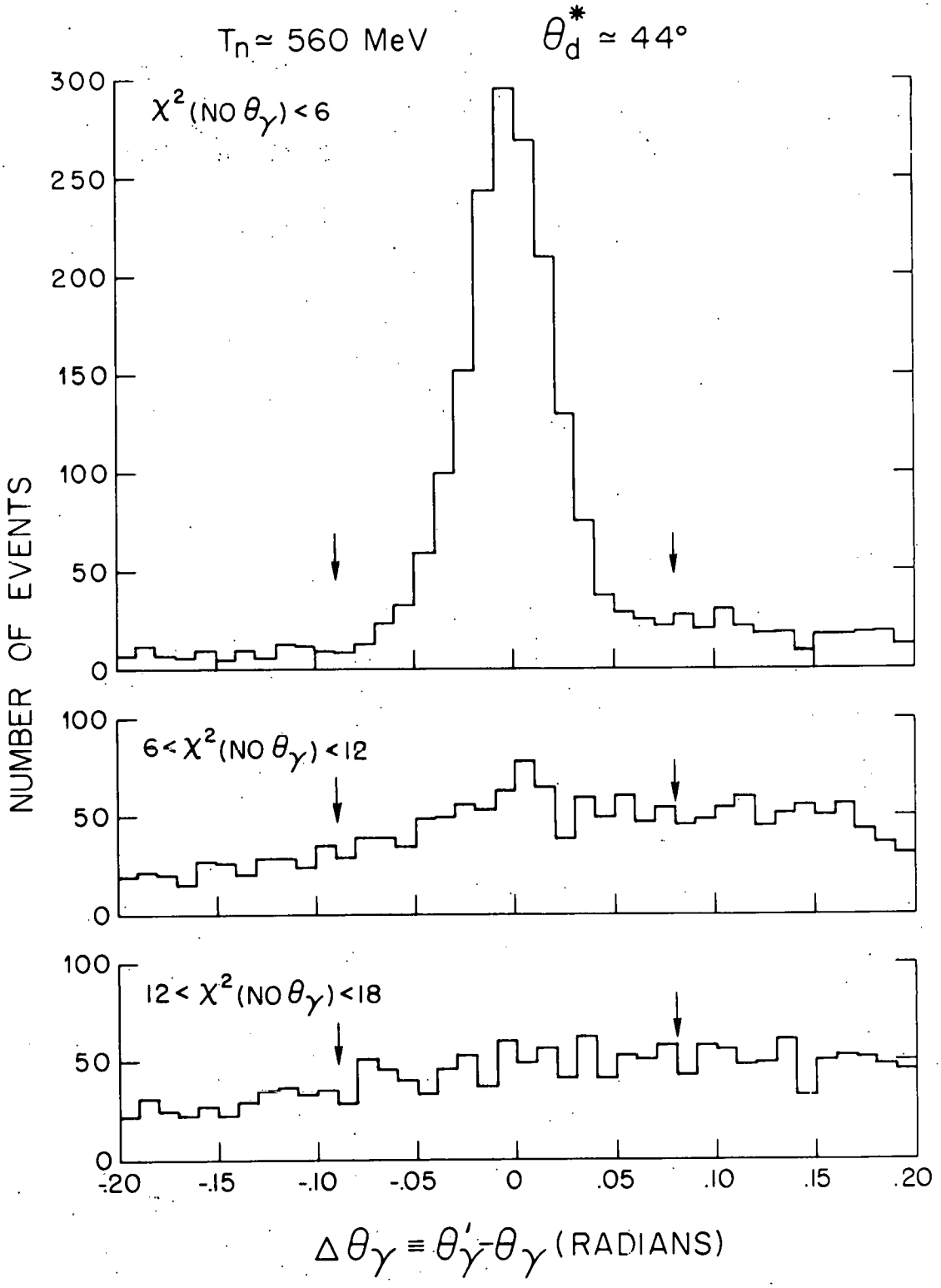
$T_n \simeq 560$ MeV
$\theta_d^* \simeq 44°$
$\chi^2(\text{NO}\,\theta_\gamma) < 6$
$6 < \chi^2(\text{NO}\,\theta_\gamma) < 12$
$12 < \chi^2(\text{NO}\,\theta_\gamma) < 18$
NUMBER OF EVENTS
300
250
200
150
100
50
0
-.20
-.15
-.10
-.05
0
.05
.10
.15
.20
$\Delta\theta_\gamma \equiv \theta'_\gamma - \theta_\gamma$ (RADIANS)

FIGURE III.6

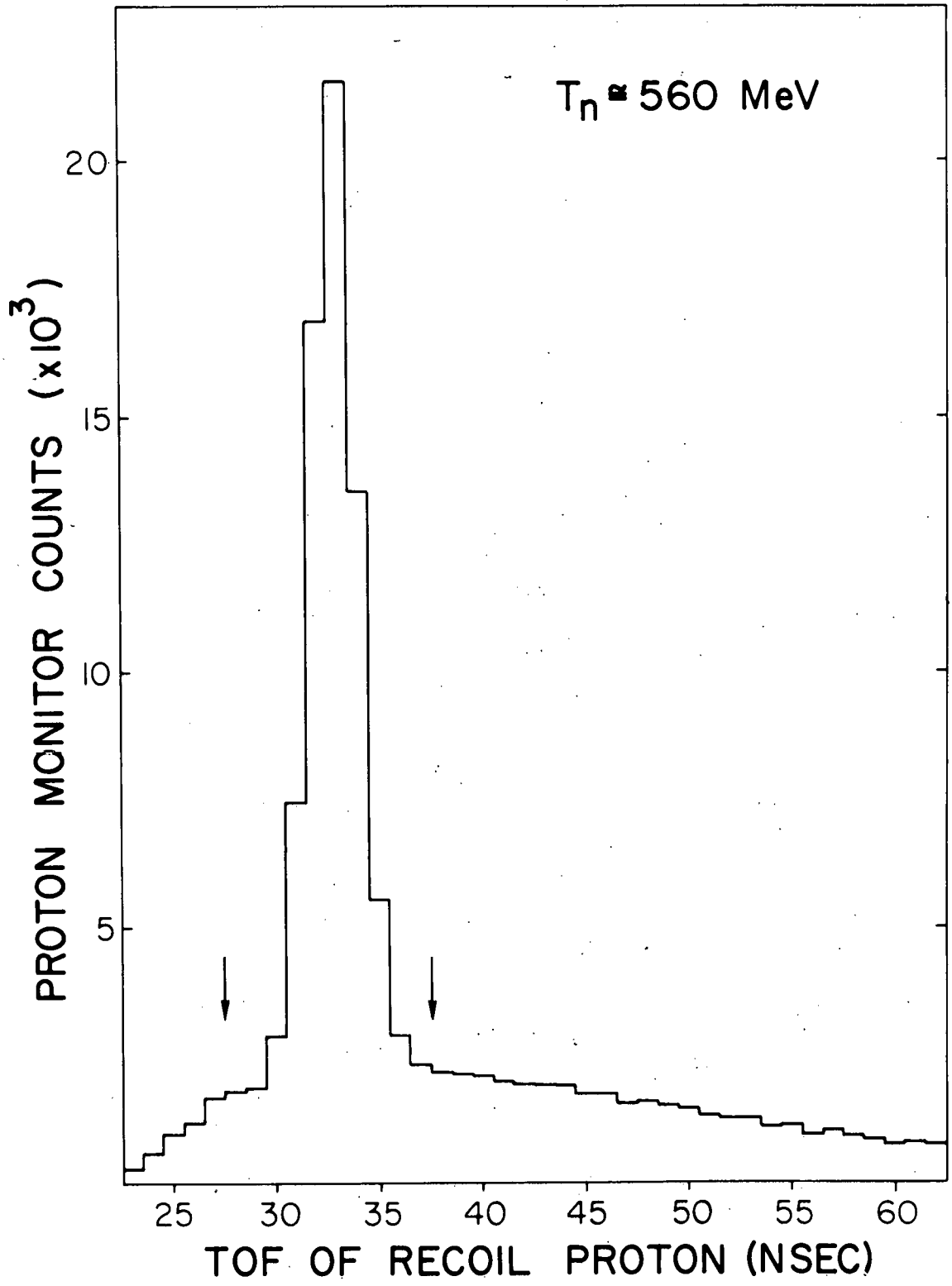
$T_n \cong 560$ MeV
PROTON MONITOR COUNTS ($\times 10^3$)
20
15
10
5
25
30
35
40
45
50
55
60
TOF OF RECOIL PROTON (NSEC)

FIGURE III.7

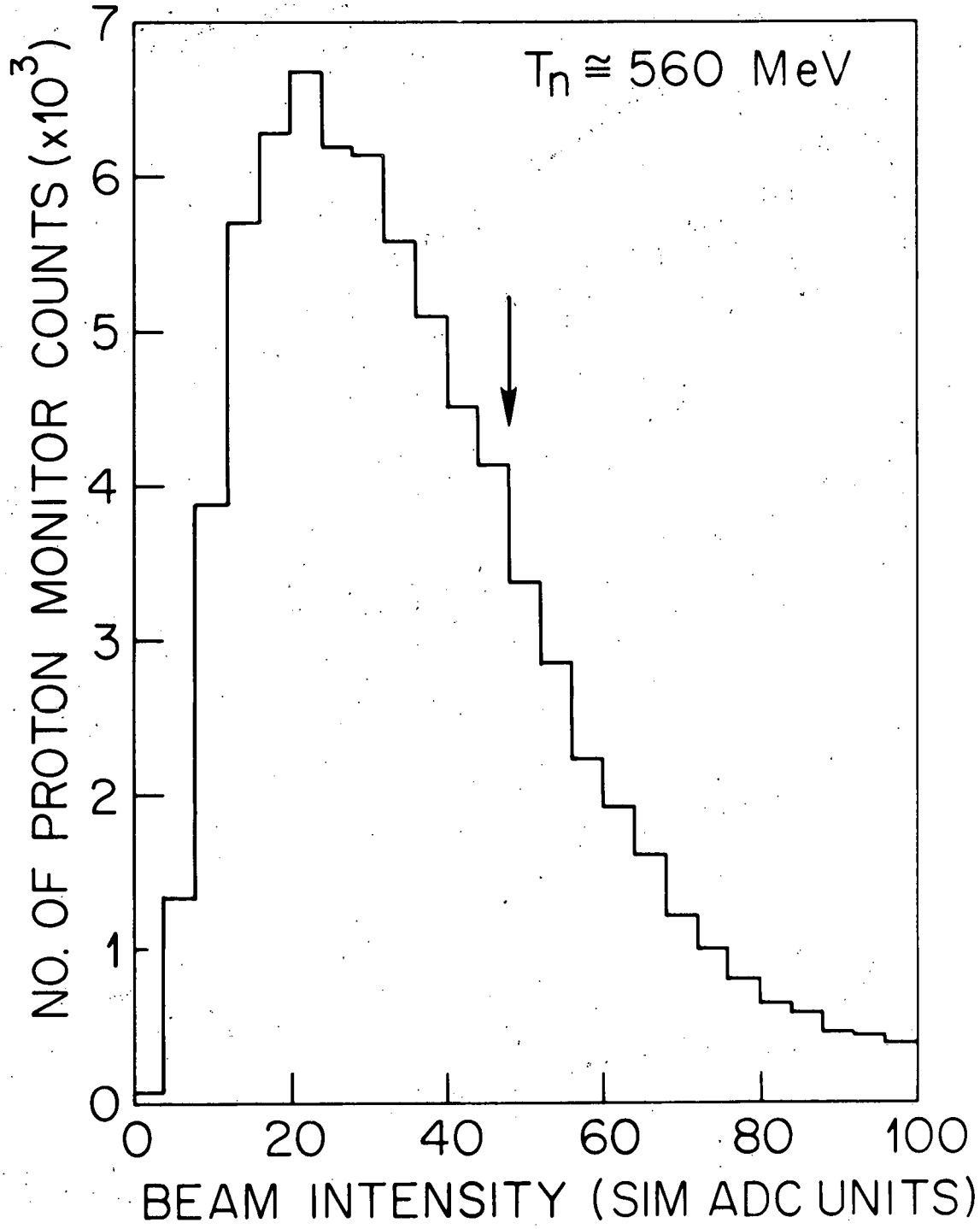
$T_n \cong 560$ MeV
NO. OF PROTON MONITOR COUNTS ($\times 10^3$)
0
1
2
3
4
5
6
7
0
20
40
60
80
100
BEAM INTENSITY (SIM ADC UNITS)

FIGURE III.8

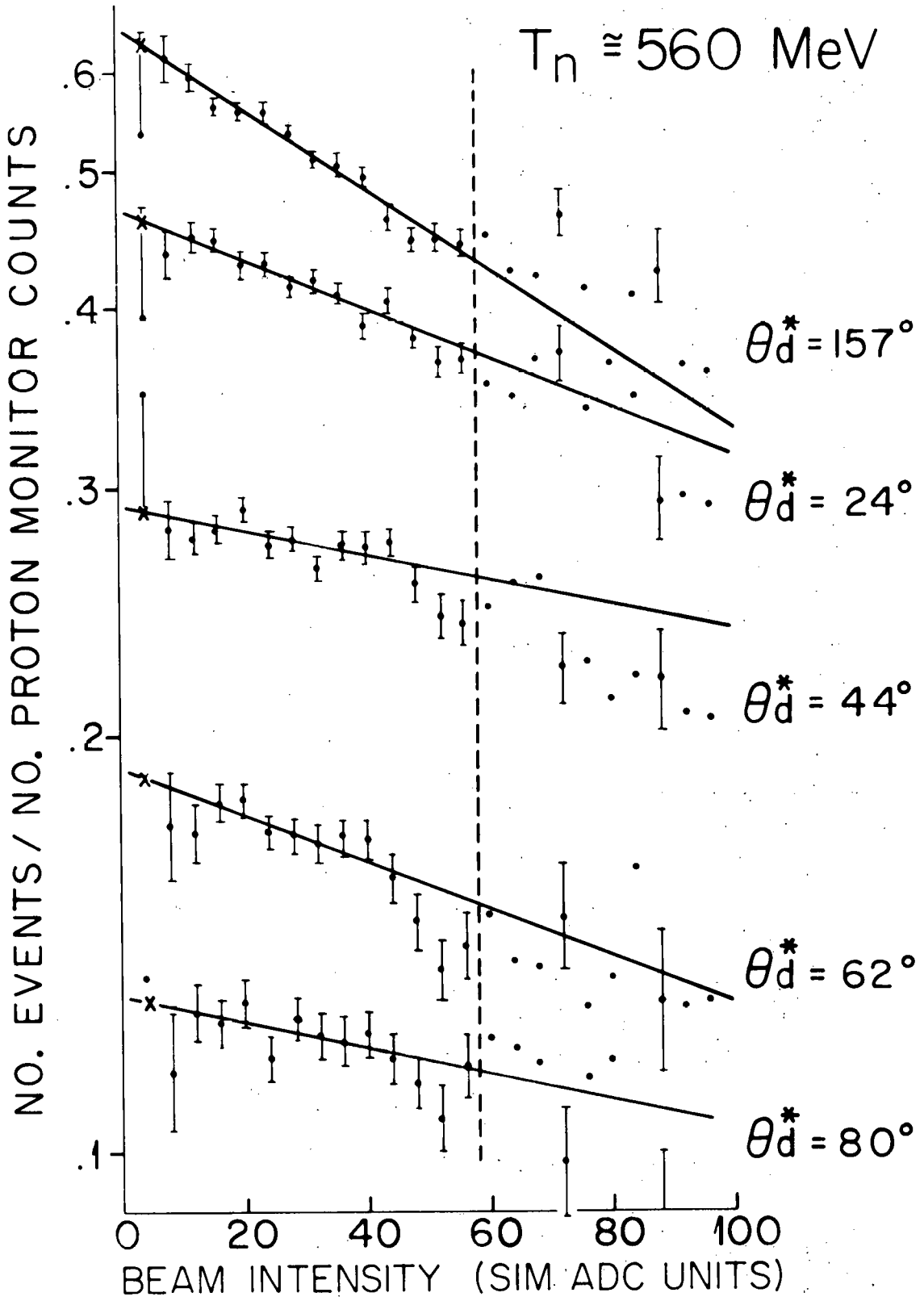
$T_n \cong 560$ MeV
$\theta_d^* = 157°$
$\theta_d^* = 24°$
$\theta_d^* = 44°$
$\theta_d^* = 62°$
$\theta_d^* = 80°$
NO. EVENTS / NO. PROTON MONITOR COUNTS
.6
.5
.4
.3
.2
.1
0
20
40
60
80
100
BEAM INTENSITY (SIM ADC UNITS)

FIGURE III.9

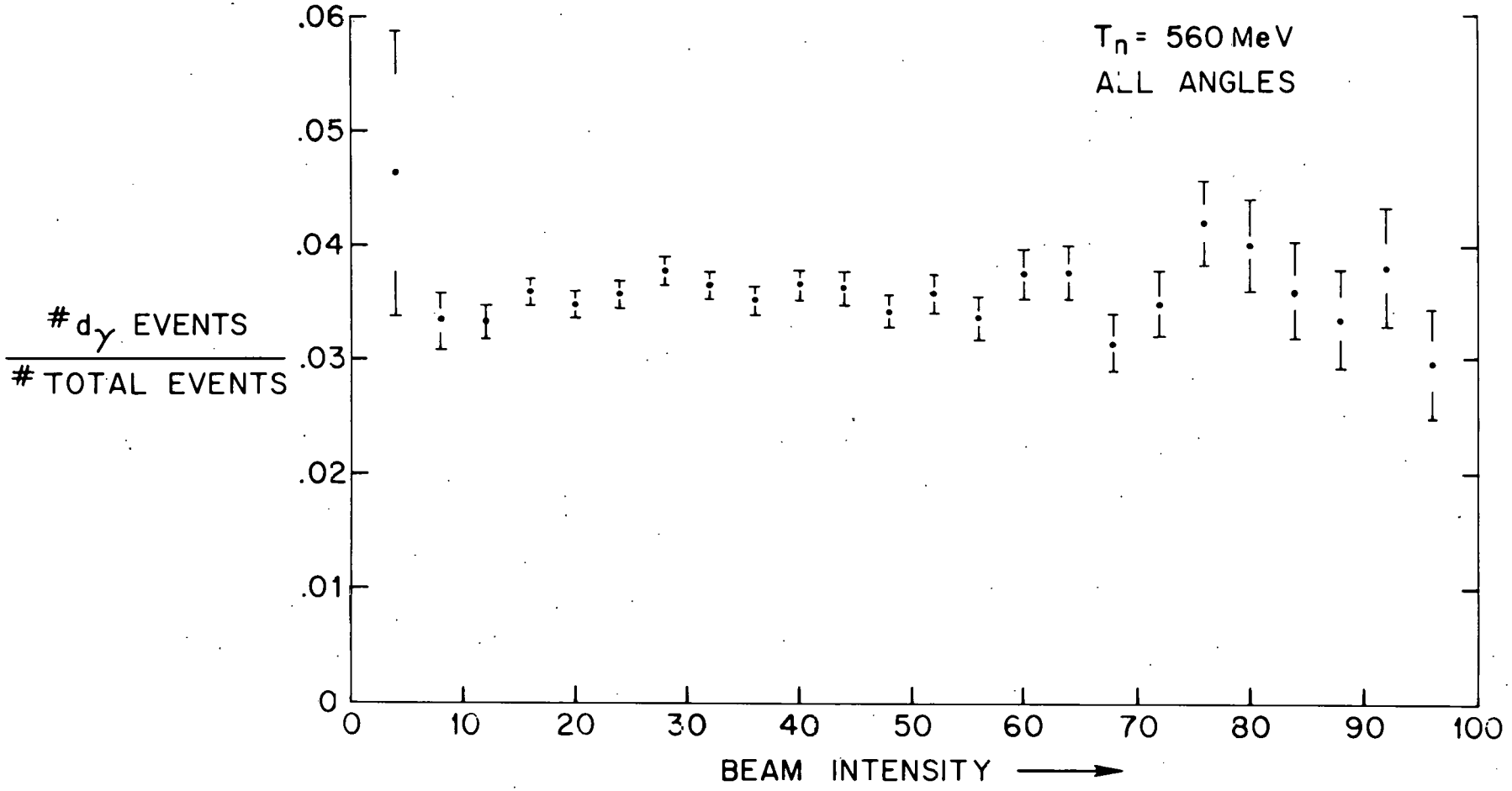

FIGURE III.10

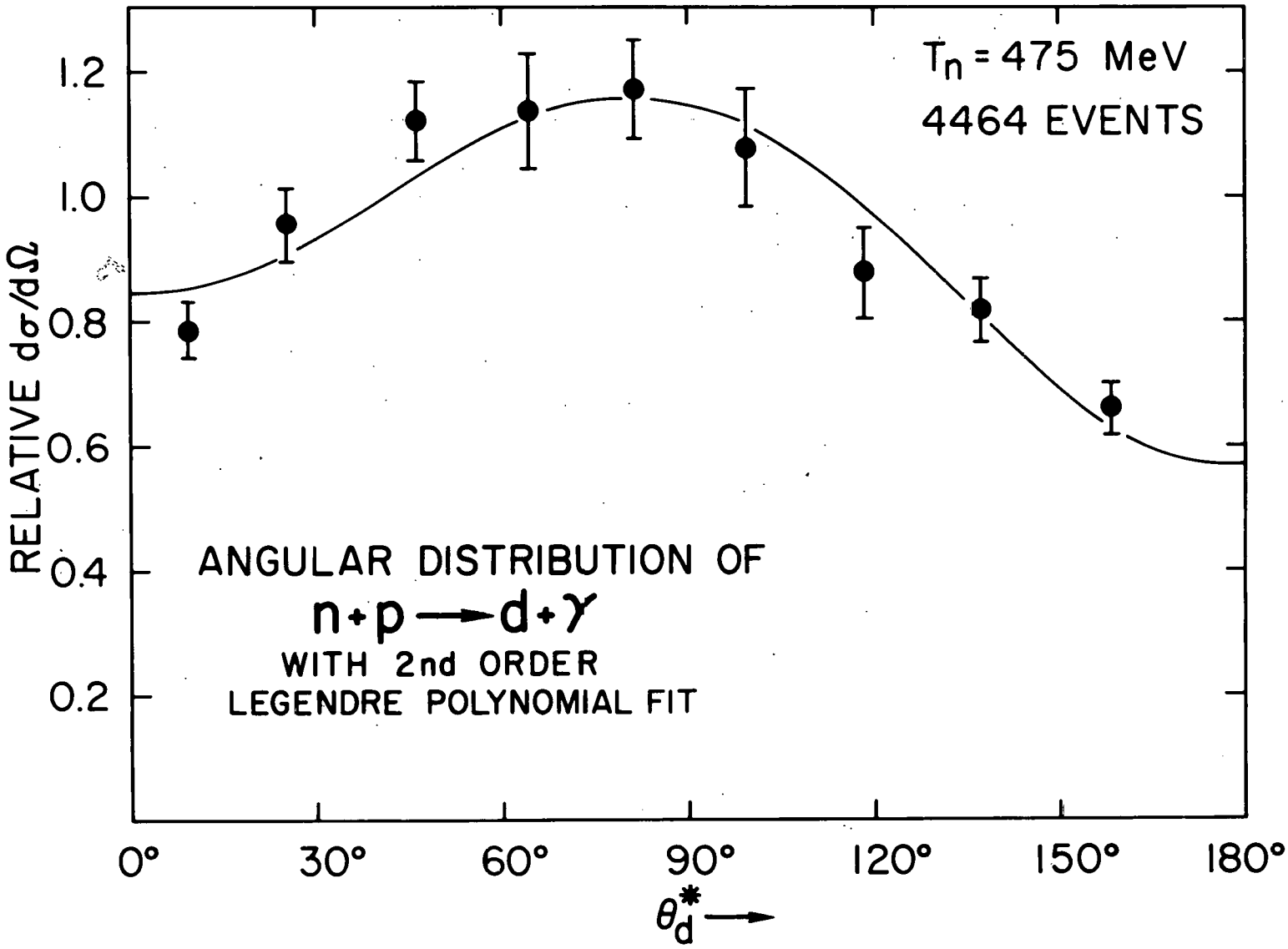
T_n = 475 MeV
4464 EVENTS
ANGULAR DISTRIBUTION OF
n+p → d+γ
WITH 2nd ORDER
LEGENDRE POLYNOMIAL FIT
RELATIVE dσ/dΩ
1.2
1.0
0.8
0.6
0.4
0.2
0°
30°
60°
90°
120°
150°
180°
θ_d^* →

FIGURE IV.1

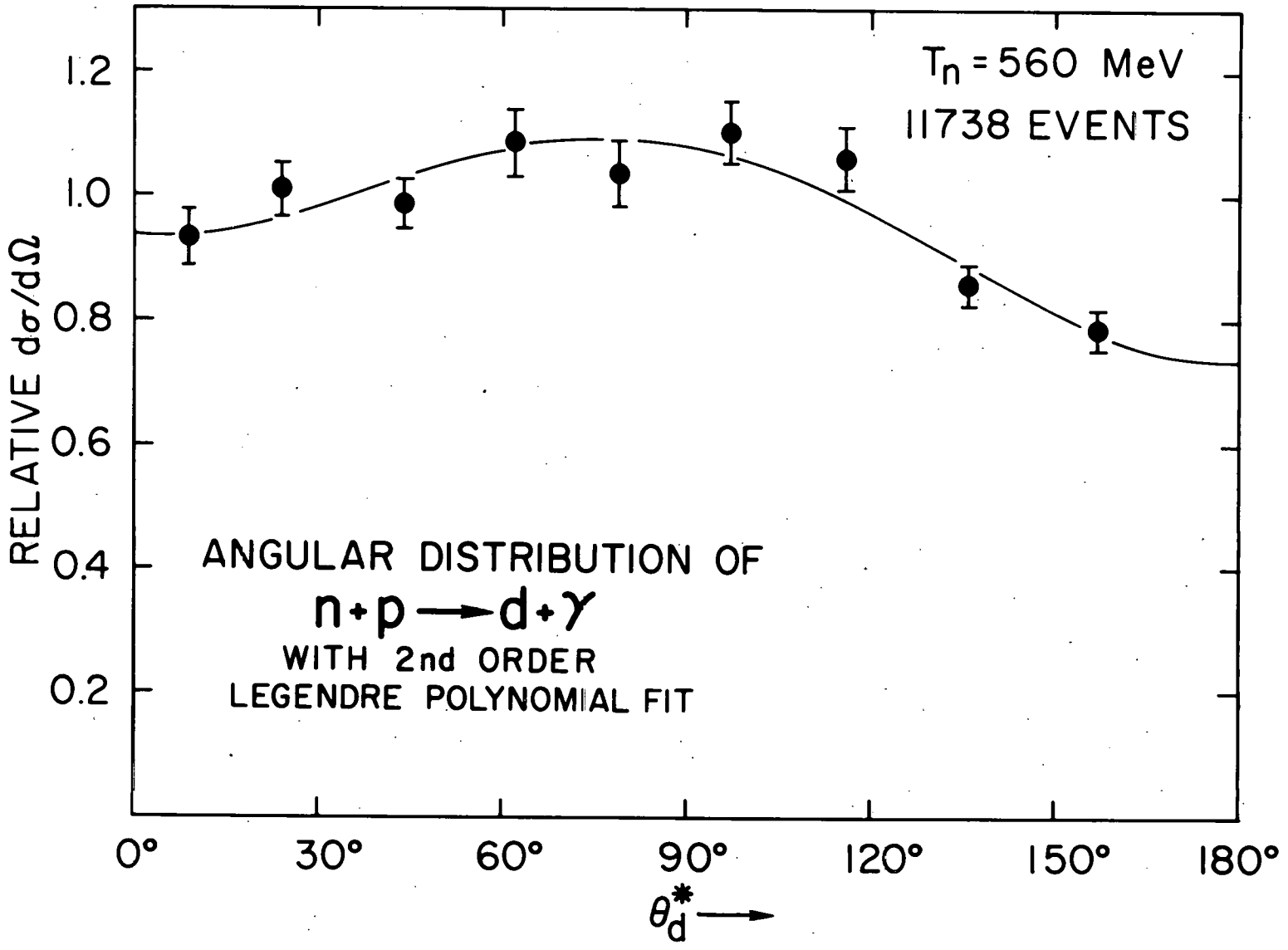
T_n = 560 MeV
11738 EVENTS
ANGULAR DISTRIBUTION OF
n+p → d+γ
WITH 2nd ORDER
LEGENDRE POLYNOMIAL FIT
RELATIVE dσ/dΩ
1.2
1.0
0.8
0.6
0.4
0.2
0°
30°
60°
90°
120°
150°
180°
θ_d^* →

FIGURE IV.2

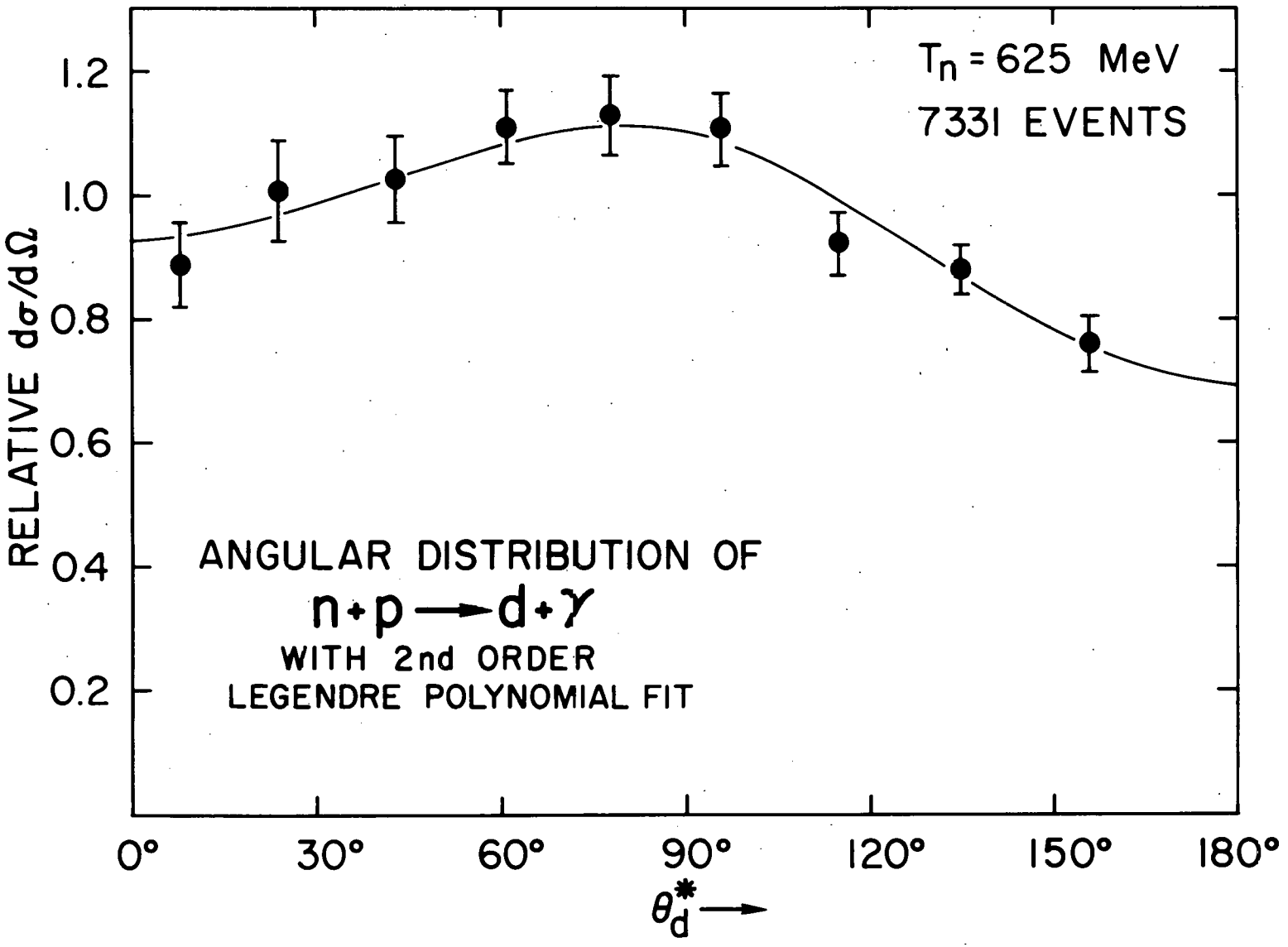
T_n = 625 MeV
7331 EVENTS
ANGULAR DISTRIBUTION OF
$n+p \rightarrow d+\gamma$
WITH 2nd ORDER
LEGENDRE POLYNOMIAL FIT
RELATIVE $d\sigma/d\Omega$
1.2
1.0
0.8
0.6
0.4
0.2
0°
30°
60°
90°
120°
150°
180°
$\theta_d^* \rightarrow$

FIGURE IV.3

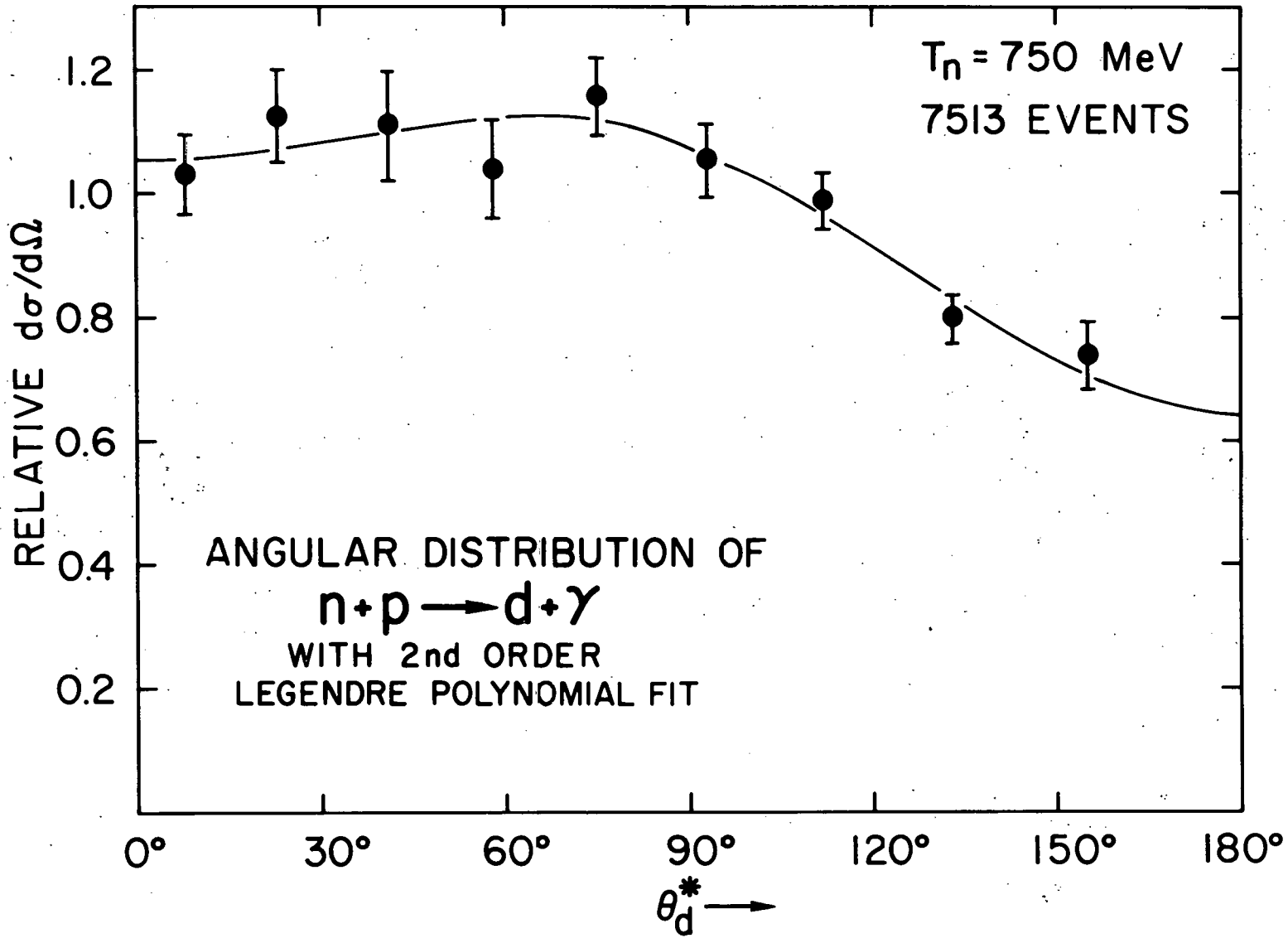
T_n = 750 MeV
7513 EVENTS
ANGULAR DISTRIBUTION OF
n+p → d+γ
WITH 2nd ORDER
LEGENDRE POLYNOMIAL FIT
RELATIVE dσ/dΩ
1.2
1.0
0.8
0.6
0.4
0.2
0°
30°
60°
90°
120°
150°
180°
θ_d^* →

FIGURE IV.4

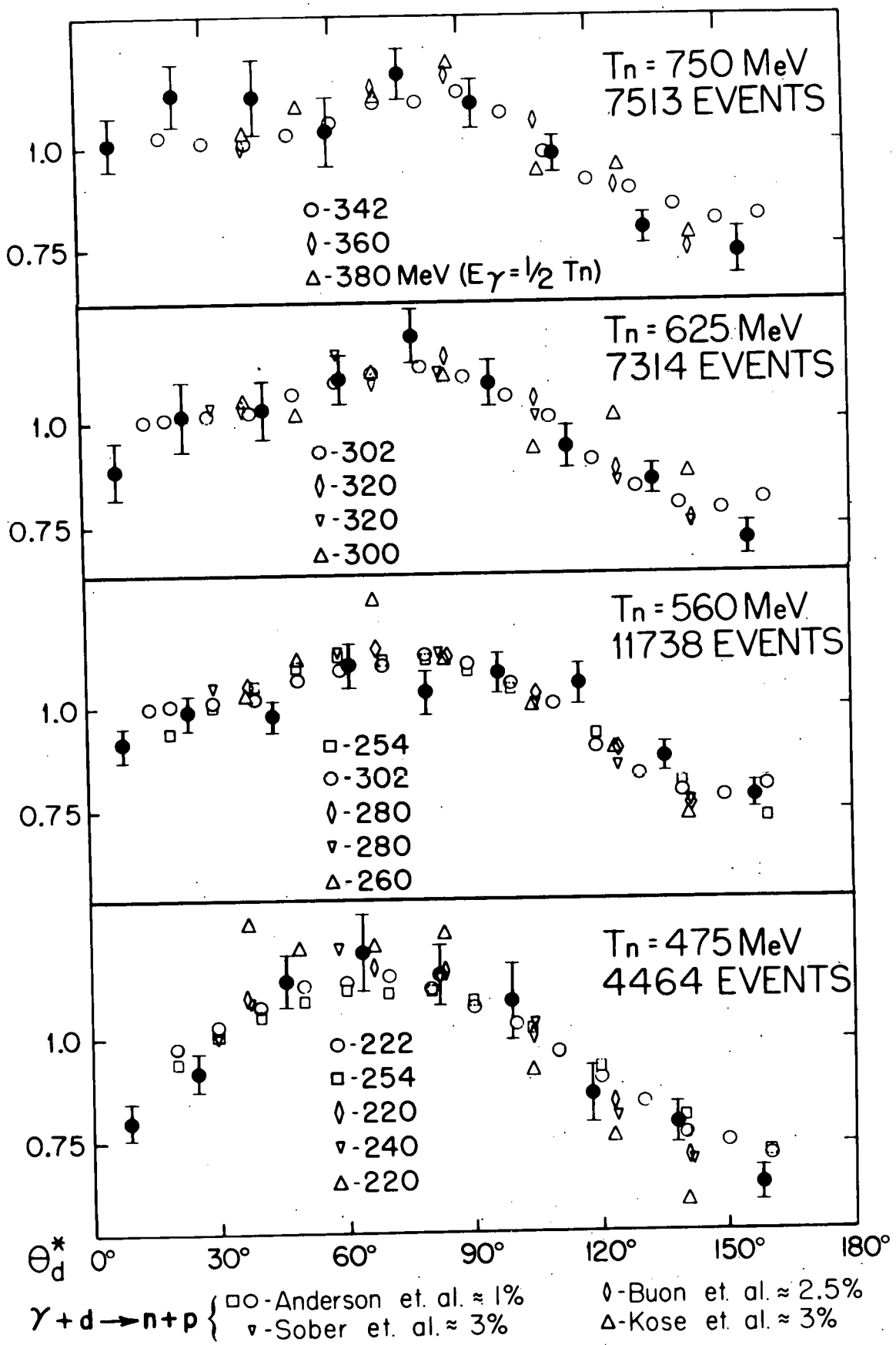
Tn = 750 MeV
7513 EVENTS
o-342
◊-360
△-380 MeV (Eγ = ½ Tn)
Tn = 625 MeV
7314 EVENTS
o-302
◊-320
▽-320
△-300
Tn = 560 MeV
11738 EVENTS
□-254
o-302
◊-280
▽-280
△-260
Tn = 475 MeV
4464 EVENTS
o-222
□-254
◊-220
▽-240
△-220
1.0
0.75
θ*d
0°
30°
60°
90°
120°
150°
180°
γ + d → n + p
□o-Anderson et. al. ≈ 1%
▽-Sober et. al. ≈ 3%
◊-Buon et. al. ≈ 2.5%
△-Kose et. al. ≈ 3%

FIGURE IV.5

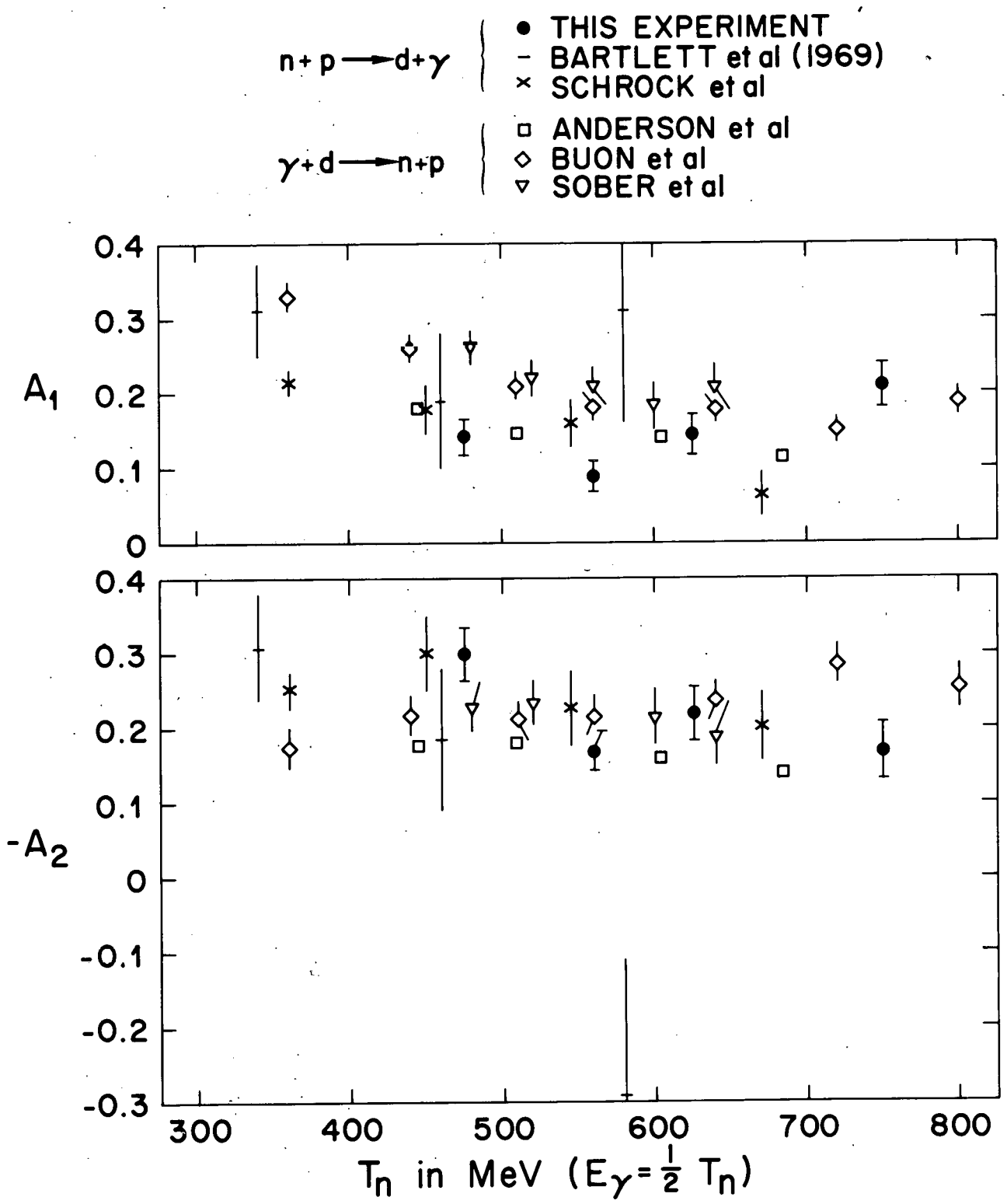
COEFFICIENTS OF
LEGENDRE POLYNOMIAL FITS
n+p → d+γ
THIS EXPERIMENT
BARTLETT et al (1969)
SCHROCK et al
γ+d → n+p
ANDERSON et al
BUON et al
SOBER et al
A1
-A2
0.4
0.3
0.2
0.1
0
-0.1
-0.2
-0.3
300
400
500
600
700
800
Tn in MeV (Eγ = 1/2 Tn)

FIGURE IV.6